Fermilab Library
0 1160 0004001 8

TEST OF BJORKEN SCALING IN DEEP INELASTIC MUON SCATTERING AT 150 AND 56.3 GEV.

A Thesis

Presented to the Faculty of the Graduate School

of Cornell University for the Degree of

Doctor of Philosophy

by

Yasushi Watanabe

August 1975

LIBOFFCE
FERMILAB
THESIS

AAB1902

Biographical Sketch

Yasushi Watanabe (former name Yasushi Ojima) was born on June 29, 1944, in Nagano City, Nagano, Japan. After graduating Toyama Chubu high school in Toyama City, Toyama, he entered Tokyo Institute of Technology in April 1963 and recieved Bachelor of Science degree in Physics in March 1967. He was adopted to Mr. and Mrs. Tokinosuke Watanabe. He enrolled in graduate school at Tokyo University in April 1967, and received Master of Science degree in physics in 1969. He enrolled in graduate school at Cornell in September 1969, and since then has been a research assistant in the Laboratory of Nuclear Studies. In October 1974 he and Miss Jyunko Hirai of Toyama, Japan, were married.

LIBOFFCE
FERMILAB
THESIS
Watanabe, Yasushi.
Test of Bjorken scaling in
deep inelastic mion scattering
at 150 and 56.3 GeV

FERMILAB
LIBRARY

DEMCO

Acknowledgments

The experiment in the thesis was proposed by my advisor Professor Louis N.Hand of Cornell and Professor K.Wendell Chen of Michigan State University.

Without their never ending enthusiasm, faith and dedication, this experiment would not have existed. I am indebted to Professor Hand for giving me the opportunity to join the experiment and for his generous help, encouragement and constructive criticisms throughout.

The success of the experiment has been the result of the combined effort of many people, including the physicists of the collaboration, consisting of, C.Chang, K.W.Chen, D.J.Fox, A.Kotlewski and P.Kunz from Michigan State, L.N.Hand, S.Herb and A.Rusell from Cornell, S.C.Loken and M.Strovink from Univ. of California, Berkeley, and W.Vernon from Univ. of California, San Diego.

I deeply regret that Donald J.Fox is not here to see the completion of this work. His devotion to the experiment was outstanding and the success of the spark chamber system owed much to his efforts.

Chuen Chang worked especially on an independent analysis, Adam Kotlewski wrote an excellent Monte Carlo program, Paul F.Kunz worked on electronics including time digitizer system, PDP11 software and developed an independent track

hunting technique for the MSU analysis.

Stephen Herb is the expert on the magnets and the magnetic measurements and has been an inspiring fellow student. Many discussions, cooperations and constructive criticisms in developing and understanding the analysis were much appreciated. I also thank him for reading this manuscript. Alison Russell worked on target counters and on the Cornell Monte Carlo. Stewart C.Loken is the expert of the PDP11 software system. The construction of a working apparatus owed much to his ingenuity. I am indebted to him for his constant encouragement and guidence. Mark Strovink designed the electronics for the proportional chamber system.

His contribution to the understanding of the data analysis, in close collaboration with Stewart C.Loken and Thomas Markiewicz has been outstanding. Wayne Vernon, with the help of Bruce Thelar provided us with the spark chambers, and his expertise on both instruments and physics has been very inspiring.

This experiment would not have been possible without the successful construction and operation of the 400 GeV proton accelerator at the Fermilab. The credit for the successful operation of the muon beam line goes to the combined effort of Drs. R.Huson, Peter Limon, R.Orr, Tim Toohig and Taiji Yamanouchi.

At early construction stage, Professor Donald Hartill

kindly taught me about making proportional chambers. Mr. Thomas Reitz helped constructing the proportional chambers and setting up the apparatus. Bruce Meyer and David Chapman developed the reliable PDP11 on-line system. K.Rajendra constructed spark chambers and designed the support system for magnets and spark chambers. G.Graham built the small magnet with S.C.Loken, which was a great help for the spectrometer calibration. Dr. Larry Litt joined at the last stage of the experiment and helped analysis.

The machine shop and the electronics shop are commended for the technical support.

Thomas Allen, Euginia Moracco and James Moravec of Purchasing are thanked for their swiftness of response.

In analyzing data, the use of the PDP10 computer at the Wilson Laboratory was crucial. Professor Boyce D.McDaniel is to be thanked for this and for his continuous encouragement.

The advice and help of the system programmers, Erick Knobil, Selden Ball and Ray Helmke are appreciated.

Mrs. Kathleen Balonek of the drafting room did the fine work of figure drawing, and the thesis was expertly typed by Mrs. Velma Ray.

Finally I thank my parents and my wife for their total understanding, patience and support both spiritual and material. Some of the typing and the drawing were done by my wife Jyunko.

Table of Contents

		Page
I.	INTRODUCTION	1
II.	INELASTIC LEPTONIC PROCESSES	4
	A. Kinematics of Inelastic Lepton Scattering	4
	1. Structure Functions and Scaling	4
	2. Longitudinal and Transverse Photons	6
	3. Cross Sections in Scaling Variables	9
	B. Related Processes	11
	1. $\nu+N\rightarrow\mu+$hadrons	11
	2. $e^+e^-\rightarrow N+$hadrons	15
	3. Hadron + hadron$\rightarrow l^+l^-$ + hadrons	17
III.	EXPERIMENTAL METHOD	19
	A. Scaling The Apparatus	23
	B. Acceptance of the Apparatus	27
	C. Muon Beam	34
	D. Targets	37
	E. Iron Core Magnets	40
	F. Proportional and Spark Chamber System	46
	G. Counters and Trigger Logic	50
	1. Trigger Logic	50
	2. Beam Counters	50
	3. Spectrometer Counters	54
	4. Beam Veto Counters	56
	5. Beam Hodoscope Counters	57
	H. Scalers	60
	I. On-Line Computer	64
IV.	DATA TAKING AND THE ANALYSIS	66
	A. Data Taking	66

Table of Contents (continued)

	Page
B. Secondary Analysis	68
C. Tertiary Analysis	74
D. Monte Carlo Simulation	81
V. RESULTS AND FITS	82
A. Histograms	82
B. Ratio of 150 and 56.3 GeV data	90
C. Propagator fit	98
D. Systematic Uncertainties	106
VI. DISCUSSIONS AND CONCLUSIONS	108
A. The Parameter Λ	108
B. Theoretical Ideas on Scaling Breakdown	110
C. Summary of the Results	113
D. Concluding Remarks	114
Appendix	
A. Detail of Apparatus	119
1. Muon Beam	119
2. Proportional Chambers	124
3. Wire Spark Chambers	131
B. Detail of Analysis Program	143
1. Track Reconstruction in the Spectrometer	143
2. Beam Track Finding	153
3. Momentum Fit	158
C. Study of Track Reconstruction and the Bias	162
1. Back Line Finding Efficiency	164
2. Point Finding Efficiency	165
3. Results	167

Table of Contents (continued)

	Page
D. Calibration of the Spectrometer	172
1. Method	172
2. Beam Energies into the Spectrometer	172
3. Results	174
E. Event Simulation: Monte Carlo Program	178
1. The Generation Part	178
2. The Spectrometer Part	180
3. Ingredients	180
F. Systematic Uncertainties	189
References	201

List of Tables

		Page
Table 3.1	Characteristics of the Experiment	22
Table 3.2	Characteristics of the Muon Beam	36
Table 3.3	Parameters of Iron Magnets	45
Table 3.4	Parameters of Proportional and Spark Chamber System	49
Table 3.5	Counter System	59
Table 3.6	Scalers and Ratios	62
Table 3.7	Word Structure of Primary Tape	65
Table 4.1	Summary of Run Conditions	67
Table 4.2	Two Other Analyses	69
Table 4.3	Secondary Tape Format	73
Table 4.4	Standard Cuts	75
Table 4.5	Tertiary Tape Format	80
Table 5.1	Summary of Fits	101
Table 5.2	ω Dependence of the Fits	101
Table 5.3	Systematic Errors and the Constrained fit	107
Table 6.1	Interpretaions of Λ in $(1 + Q^2/\Lambda^2)^{-2}$	109
Table A.1	Front End Parameters	121
Table A.2	Parameters of Muon Beam Line	123
Table A.3	Construction and Operation of Proportional Chambers	130
Table A.4	Construction and Operation of Spark Chambers	142
Table B.1	Terminology for Track Reconstruction	144

List of Tables (continued)

		Page
Table B.2	Beam Track Reconstruction	157
Table C.1	Track Finding Efficiency	171
Table D.1	The Conditions of Calibration Runs	173
Table D.2	The Results of Calibration	177
Table E.1	Format of Generated Events	181
Table E.2	Effects Included in the Monte Carlo Program	182
Table F.1	Normalization Factors	191
Table F.2	Amount of Absorber Upstream of BV and BV Latching	197

List of Figures

		Page
Figure 2.1	One Photon Exchange Diagram for $\mu+N\rightarrow\mu+$hadrons and kinematical Values	7
Figure 2.2	Kinematical Region of $\mu+N\rightarrow\mu+$hadrons in Q^2-ν Plane and Lines of Constant Kinematical Values	7
Figure 2.3	Scaling Behavior of $\nu W_2(Q^2,\omega)$ vs. ω'	8
Figure 2.4a	Mean Square Charge of Interacting Constituents	14
Figure 2.4b	$\sigma_T(\nu+N\rightarrow\mu+$hadrons$)$ vs. E_ν	14
Figure 2.5	Kinematical Region of $e^+e^-\rightarrow N+$hadrons	16
Figure 3.1a	Schematic of the Apparatus for 150 and 56.3 GeV	21
Figure 3.1b	Scaling of the Apparatus	26
Figure 3.2a	Generated Events in Q^2-ν Plane	29
Figure 3.2b	Acceptance in Q^2-ν Plane	30
Figure 3.2c	Generated Events in P-P_T Plane	31
Figure 3.2d	Acceptance in P-P_T Plane	31
Figure 3.2e	Lines of Constant Kinematical Values in P-P_T Plane	32
Figure 3.3	Schematic of Muon Beam Line	35
Figure 3.4	Target Cart Geometry	39
Figure 3.5	Magnet and Magnet Cart.	41
Figure 3.6	B(r) of Iron Core Magnets	42
Figure 3.7	Calibration of the Spectrometer	44
Figure 3.8a	Schematic of Trigger Logic	51
Figure 3.8b	Detail of Electronics and Trigger Logic	52
Figure 3.9	Halo and Spectrometer Counters	55

List of Figures (continued)

		Page
Figure 3.10	HA Hodoscope	58
Figure 4.1	Flow Diagram of Secondary Analysis	71
Figure 4.2	Typical z_{int} distribution after all the cuts	77
Figure 4.3a	The Stability of Event Rate (150GeV)	78
Figure 4.3b	The Stabiltiy of Evnet Rate (56.3Gev)	79
Figure 5.1	Histograms of 150 and 56.3 GeV data	84
Figure 5.2	Ratio of 150/56.3 GeV data (Corrected by Monte Carlo)	92 92
Figure 5.3	The Effect of the Different Beam Size (150/56.3 GeV Monte Carlo)	94
Figure 5.4	r_B^2 Distribution of 150 and 56.3 GeV Beam	96
Figure 5.5	Scaling of Apparatus (Monte Carlo/Monte Carlo)	97
Figure 5.6	$N-1/\Lambda^2$ Contour of the Propagator Fit	102
Figure 5.7	Q^2 Behavior at Different ω Region	103
Figure 5.8a	Generated Events in Q^2-ω Plane	104
Figure 5.8b	Acceptance in Q^2-ω Plane	105
Figure A.1	Fermilab Switchyard	120
Figure A.2	Cross Sectional View of a Proportional Chamber	125
Figure A.3	Charpak Discriminator	128
Figure A.4	Latch Circuit for the Proportional Chamber System	129
Figure A.5	Spark Chamber Plates	132
Figure A.6	Finished Spark Chamber Plate	133

List of Figures (continued)

		Page
Figure A.7a	Operation of Spark Chamber	135
Figure A.7b	The Detail of Spark Chamber Operation	135
Figure A.8	Pre-amplifier	137
Figure A.9	Zero Crossing Discriminator	138
Figure A.10	Schematic of Time digitizer Operation	141
Figure B.1	Line Finding Windows and Histograms	147
Figure B.2	Hour Glass Window	148
Figure B.3	One Dimensional χ^2 vs. 1/p	150
Figure B.4	The Distance from p=∞ point vs. 1/p	152
Figure B.5a	Matching of UVW Chamber Module	156
Figure B.5b	χ^2/dof of Beam Tracks	156
Figure C.1	Binning and Numbering of a Spark Chamber Plane(for Efficiency Study)	163
Figure C.2	Track Finding Efficiency Over the Plane	169
Figure C.3	Track Finding Efficiency vs. r_{13}	170
Figure D.1	A Typical E'(Reconstructed) Distribution	175
Figure E.1	νW_2^{IRON} vs ω	184
Figure E.2	Typical Cross Section, Radiative Corrections and Wide Angle Bremsstrahlung	186
Figure E.3	Radiative Corrections	187
Figure E.4	Integrand of Exact Formula of Radiative Corrections	188 188
Figure F.1	The Movement of Events in Q^2-ν Plane by Shifting E' by +1%	193
Figure F.2	The Effect of E' Resolution in Q^2-ν Plane	193
Figure F.3	Effects of Underlying Physics	200

I. INTRODUCTION

Understanding of the ultimate structure of matter has been one of the most fundamental interests of human beings. In uncovering the structure down to shorter and shorter distances, the technique of scattering particles has been extensively used.

Using the lepton is especially successful because of the "known and rather weak" interaction.

Recent experiments done at the Stanford Linear Accelator Laboratory (SLAC) using electrons revealed a remarkable regularity in the scattering off nucleons.[1] The regularity called "scaling" was theoretically suggested by Bjorken[2], and the observation of the phenomenon has caused a great excitement among both theorists and experimentalists.

Inelastic scattering observing leptons only measures invariant functions of nucleons, called structure functions, which usually depend on two invariant variables. Scaling is a phenomenon in which the structure functions become only a function of the ratio of the two variables when they are sufficiently large.

An intuitively appealing way of understanding the phenomenon is the parton model proposed by Feynman.[3] In this picture, hadrons are made of pointlike constituents named partons, and we are observing the distributions of thses partons. Identifying them with the long pursued quarks does

not seem to be a wild idea and at least provides experimentally accessible predictions.[4]

This rather naive picture was shown to be equivalent to more formal approaches.[5] The understanding of this mechanism, whereby the partons behave like free and bare particles during the interaction, was further advanced by the discovery of asymptotically free field theories[6] in which the strong interaction could become weaker at shorter distances.

Actually the observation of scaling in deep inelastic scattering was rather puzzling in that it occurred at rather low energy to be asympotic.

This was especially the case, when the scaling was found to be badly violated in the crossed channel, e^+e^- annihilation process.[7]

Subsequently exciting new particles were found[8] in this process, and the violation seems to be a threshold effect; beyond that energy, the scaling seems to set in at a new level.[9]

It is of particular interest to test scaling in the scattering channel over a much larger kinematical range to see if it continues to hold. A breakdown of scaling necessarily implies new physics, giving new informations on the structure of hadrons.

We report on an experiment carried out at Fermilab, using 150 and 56.3 GeV muons as the probe.

At this energy, muons are replacing the role long held by electrons in probing matter, because of the ease both in obtaining such a high energy beam and in detecting them.

Comparing to the electron scattering experiments at SLAC, the muon intensity is down by about seven order of magnitudes, some of which could be made up with the use of heavy target.

Relevant cross section is measured in terms of nano barns. So the experimental method employed is quite different.

Muons were scattered from an iron target. The spectrometer to detect and reconstruct the scattered muons consists of wire spark chambers, plastic scintillation counters and solid iron toroidal magnets. It has a large aperture and azimuthally symmetric acceptance.

The apparatus was designed so that events with scaled kinematical values would go through the same region in the detectors at the two energies. Any two distributions would be identical within the experimental accuracy if the scaling holds at the two energies.

The kinematical region that was explored for the first time was Q^2 up to 40 $(\mathrm{GeV}/c)^2$ and ν up to 100 GeV.

In Section II we define the kinematics of this and the related processes and observe the behavior of the cross sections when Bjorken scaling holds. The essense of the experimental method is given in Section III, while some of the detail is described in Appendix A.

Data analysis is described in Section IV and more in detail in Appendix B. Considering the "propagator" type of violation as a convenient parametrization, we obtain a limit to a scaling breakdown by comparing the two energies in Section V. Systematic errors and their sensitivities are considered in this parametrization. Finally in Section VI, some of theoretical ideas on scaling breakdown are reviewed, followed by concluding remarks.

II. INELASTIC LEPTONIC PROCESSES

A. Kinematics of Inelastic Lepton Scattering

1. Structure functions and scaling

We consider the process where a charged lepton (electron or muon) is scattered from a nucleon. The final state of the hadron system is not observed and hence an automatic summation over the final state is performed. This process is, in good approximation, represented by the one photon exchange diagram shown in Figure 2.1, where definitions of kinematical values are also given.

The lepton vertex is "known", i.e. by observing the incident and scattered lepton, we effectively scatter a virtual photon of known energy and mass off the nucleon.

The cross section can be written as

$$d\sigma = \sum_{\text{final}} \sum_{\text{spin}} \left| \langle p' | j^{\mu}(0) | p \rangle \frac{i}{q^2} \langle \text{final} | J_{\mu}(0) | P \rangle \right|^2 \delta^4(p' + P_f - p - P) \tag{2.1}$$

where j_μ and J_μ are lepton and hadron electromagnetic (EM) currents and i/q^2 is from the photon propagator. The matrix element of j_μ is known, while that of J_μ is our main interest.

The formula becomes

$$d\sigma \propto \frac{1}{(q^2)^2} w^{\mu\nu} W_{\mu\nu} \tag{2.2}$$

where $w_{\mu\nu}$ is the tensor for the lepton and given by

$$w_{\mu\nu} = p_\mu p'_\nu + p_\nu p'_\mu - g_{\mu\nu}(p'p) \tag{2.3}$$

while $W_{\mu\nu}$ is

$$W_{\mu\nu} = (2\pi)^2 \frac{P_o}{M}\int(2\pi)^4\delta^{(4)}(q+P-P_f) \sum_{\text{final}} \sum_{\text{spin}} \langle P|J_\mu(0)|P_f\rangle \langle P_f|J_\nu(0)|P\rangle \tag{2.4}$$

$$= (2\pi)^2 \frac{P_o}{M}\int d^4x\ e^{iqx} \langle P|[J_\mu(x),\ J_\nu(0)]|P\rangle \tag{2.5}$$

(nucleon spin averaged. P_o/M is convention.)

The commutator appears in Eq. (2.5) because the other term does not physically contribute.

Current and parity conservation together with Lorentz invariance allow $W_{\mu\nu}$ to be written in terms of two invariant functions W_1 and W_2, customarily defined as follows.

$$W_{\mu\nu} = -(g_{\mu\nu} - \frac{q_\mu q_\nu}{q^2})W_1(q^2,\nu) + \frac{1}{M^2}(P_\mu - \frac{Pq}{q^2}q_\mu)(P_\nu - \frac{Pq}{q^2}q_\nu)W_2(q^2,\nu)$$

$$\nu = P\cdot q/M \tag{2.6}$$

where q^2 and ν are the only independent invariant variables describing the vertex and W_1 and W_2 are functions of these two variables.

The cross section becomes

$$\frac{d^2\sigma}{dE'd\Omega} = \frac{4\alpha^2}{(q^2)^2} E'^2 (W_2 \cos^2\frac{\theta}{2} + 2W_1 \sin^2\frac{\theta}{2}) \tag{2.7}$$

So these two so-called structure functions can be measured, and contain the information of the hadron structure.

The kinematically allowed region in terms of these two invariants is shown in Figure 2.2. It is obtained from the relations,

$$\begin{aligned} W^2 &\equiv P_f^{\,2} = (P+q)^2 = M^2 + 2M\nu - Q^2 \geq M^2 \\ Q^2 &\equiv -q^2 > 0 \end{aligned} \tag{2.8}$$

Bjorken conjectured that in the limit of both Q^2 and ν large, but the ratio of the two fixed, MW_1 and νW_2 (not W_2 nor $\nu^2 W_2$, etc.) become functions of the ratio only.[2]

This is the scaling hypothesis:

$$\begin{aligned} &MW_1(\omega,Q^2) \to F_1(\omega) \\ &\nu W_2(\omega,Q^2) \to F_2(\omega) \\ &Q^2 \to \infty,\ \omega \equiv 2M\nu/Q^2 = \frac{1}{x} \geq 1 \text{ fixed} \end{aligned} \tag{2.9}$$

This appeared to be confirmed by the experiments done at the Stanford Linear Accelerator Center (SLAC).[1]

To exhibit scaling in a broader kinematical region, another scaling variable ω' was introduced.

$$\omega' \equiv \frac{W^2}{Q^2} = \omega + \frac{M^2}{Q^2} \equiv \frac{1}{x'} \tag{2.10}$$

The universal behavior that was observed is reproduced in Figure 2.3 together with the best fit to the points.

2. Longitudinal and transverse photons

Before going further, we introduce another useful expression, considering the process as the absorption of a virtual photon by the nucleon. The photon acquires longitudinal polarization for $Q^2 \neq 0$, and we can express the

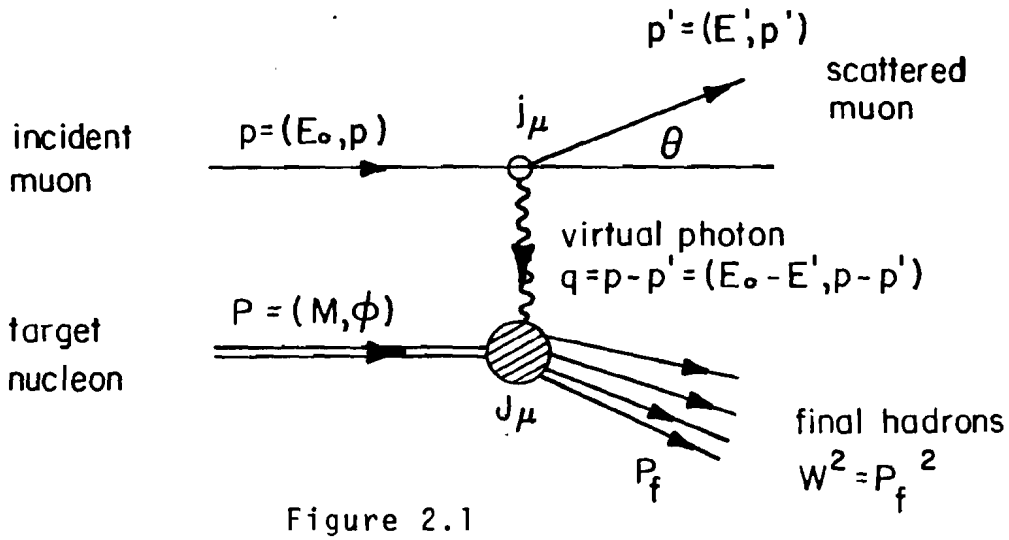

Figure 2.1

One photon exchange diagram for $\mu N \to \mu +$ hadrons and kinematical values

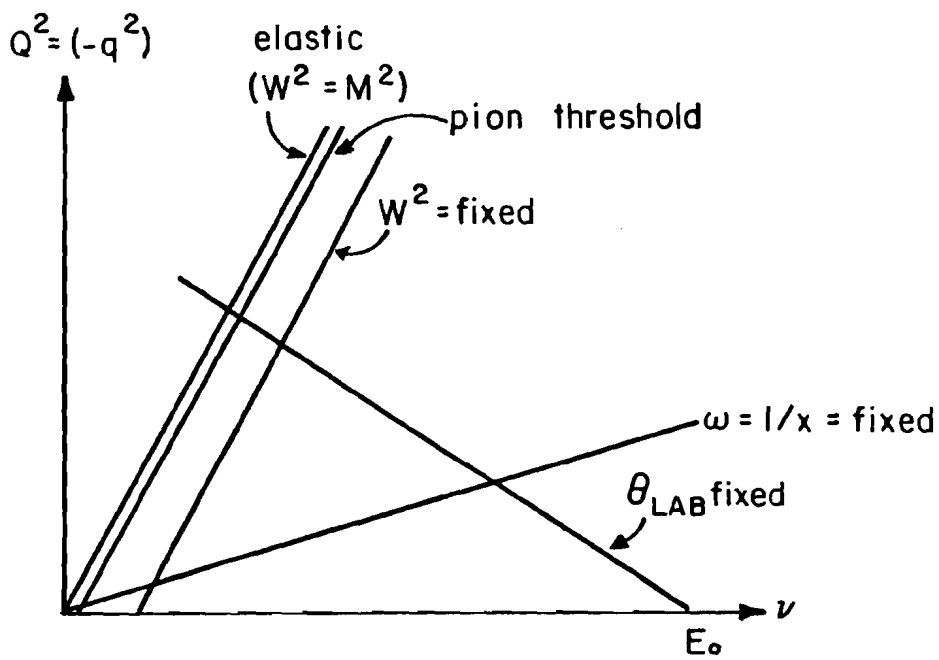

Figure 2.2

Kinematical region of $\mu N \to \mu$ + hadrons and lines of constant kinematical values

Figure 2.3 Scaling of the structure function

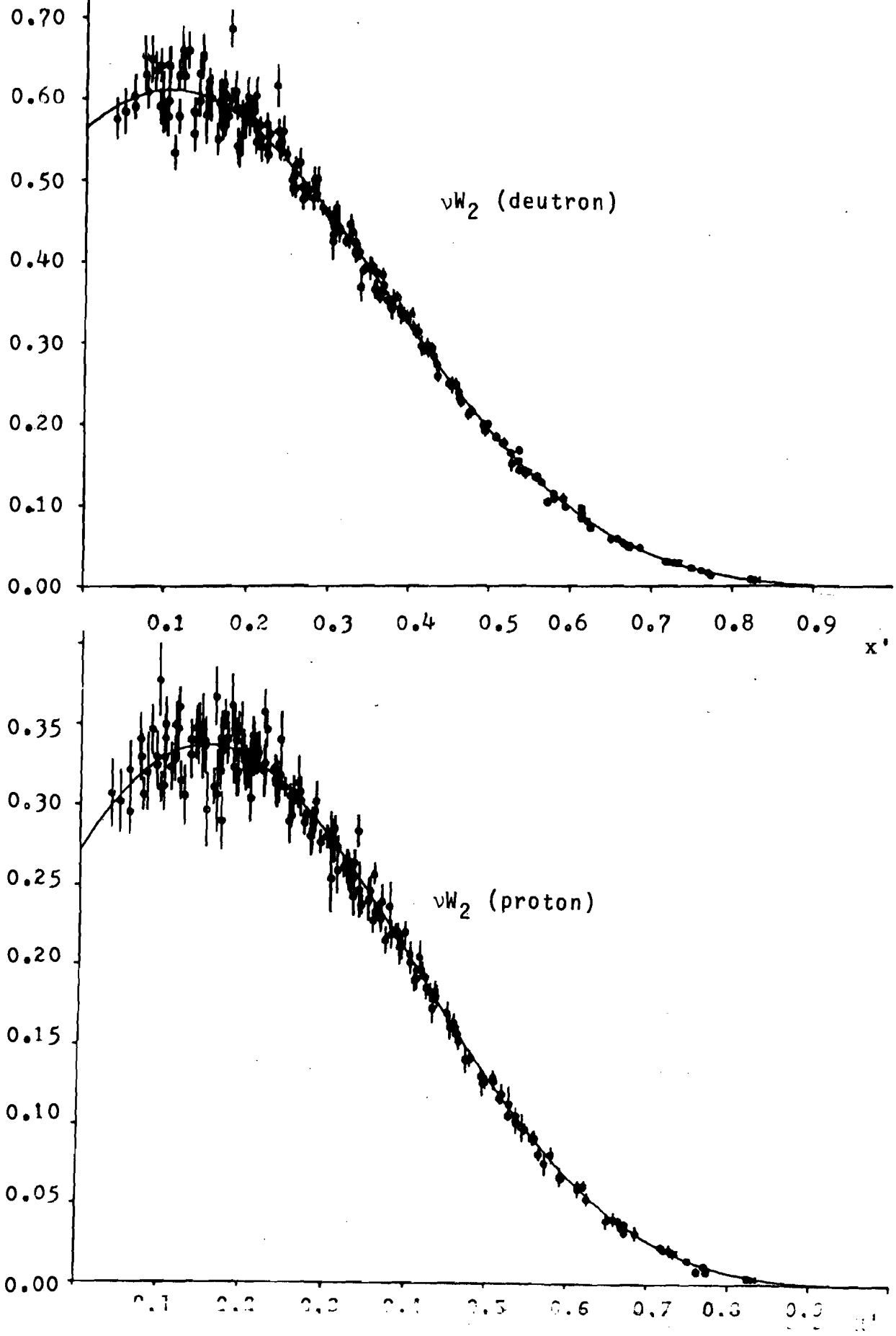

differential cross section in terms of σ_T and σ_L, the total cross section for the transverse and longitudinal photons.[10]

$$\frac{d^2\sigma}{dE'd\Omega} = \Gamma_\gamma \sigma_T (1 + \varepsilon R) \tag{2.11}$$

Γ_γ and ε are interpreted as the flux and the amount of polarization of the virtual photon.

$$\begin{aligned} \Gamma_\gamma &= \frac{\alpha}{4\pi^2} \frac{K}{Q^2} \frac{E'}{E_0} \frac{2}{1-\varepsilon} \\ \varepsilon &= \left(1 + 2(1 + \nu^2/Q^2)\tan^2 \tfrac{\theta}{2}\right)^{-1}, \quad 0 \le \varepsilon \le 1 \\ K &= \nu - Q^2/2M \\ R &= \sigma_L/\sigma_T \end{aligned} \tag{2.12}$$

As expected, $\sigma_L \to 0$, $\sigma_T \to \sigma_{\gamma N}$, $K \to \nu$, as $Q^2 \to 0$, i.e. it approaches to the real photon process. R is closely related with the spin of the constituents.

The structure functions defined above are related to these absorption cross sections:

$$\begin{aligned} W_2 &= \frac{K}{4\pi^2\alpha} \frac{Q^2}{Q^2+\nu^2} (\sigma_T + \sigma_L) \\ W_1 &= \frac{K}{4\pi^2\alpha} \sigma_T \end{aligned} \tag{2.13}$$

3. Cross section in scaling variables

To make the scaling aspect of the process more explicit, we introduce another variable, which depends on the kinematics of the lepton side.

$$y \equiv \frac{2M\nu}{S} \quad , \qquad S \equiv (p + P)^2 \tag{2.14}$$

The cross section is now, in small angle approximation,

$$S \frac{d^2\sigma}{dxdy} = 4\pi\alpha^2 F_2(x,Q^2) \frac{1}{(xy)^2} \left[1 - y + \frac{1}{2(1+R(x,Q^2))} y^2\right] \tag{2.15}$$

It is clear from this that if F_2 and R become functions of x only independent of Q^2, $S \frac{d^2\sigma}{dxdy}$ is a function of x and y, independent of S.

The scaling can be intuitively understood in terms of dimensional analysis. If masses and dimensional couplings are strictly zero, no natural scale is defined and the scale is solely determined by the large kinematical values. This situation may be realized if the kinematical values become much larger than natural scales in the real world. In this sense the question of why MW_1 and νW_2 scale may be understood. The cross section behaves as $\sim 1/Q^2$ at high Q^2, and the relations of (2.13) give the behavior of W_1 and W_2

B. Related Processes

Investigating the structure of hadrons and scaling behavior, it is important to correlate all the related processes. Some are discussed below.

1. $\nu(\bar{\nu}) + N \to \ell^{\mp} + \text{hadrons}$

A similar argument applies in this process in probing the structure of nucleons. To first order, the interaction of the lepton part is known and the tensor $W_{\mu\nu}$ is now

$$W_{\mu\nu}^{\nu,\bar{\nu}} = (2\pi)^2 \frac{P_o}{M} \int dx\, e^{iqx} \langle P|[J_\mu^{\mp}(x), J_\nu^{\pm}(0)]|P\rangle$$

$$= -(g_{\mu\nu} - \frac{q_\mu q_\nu}{q^2})\, W_1^{\nu,\bar{\nu}}(q^2,\nu)$$

$$+ \frac{1}{M^2}(P_\mu - \frac{pq}{q^2} q_\mu)(P_\nu - \frac{pq}{q} q_\nu) W_2^{\nu,\bar{\nu}}(q^2,\nu)$$

$$- i\varepsilon_{\alpha\beta\mu\nu} \frac{P^\alpha q^\beta}{2M^2} W_3^{\nu,\bar{\nu}}(q^2,\nu) \qquad (2.16)$$

The other three terms become proportional to the square of the lepton mass and thus negligible. The third term is due to the parity violation.

If we introduce "scaling" functions

$$\begin{aligned} MW_1(q^2,\nu) &= F_1(x,q^2) \\ \nu W_2(q^2,\nu) &= F_2(x,q^2) \\ \nu W_3(q^2,\nu) &= F_3(x,q^2) \end{aligned} \qquad (2.17)$$

the cross section can be written at high energy,

$$\frac{d^2\sigma^{\nu,\bar{\nu}}}{dxdy} \doteq \frac{G^2S}{2\pi}\left[xy^2F_1^{\nu,\nu} + (1-y)F_2^{\nu,\nu} \mp xy\left(1-\frac{y}{2}\right)F_3^{\nu,\nu}\right] \tag{2.18}$$

where G is the Fermi coupling constant for the weak interaction,

$$G \cong 10^{-5}/M_p^2$$

and the upper sign is for the neutrino.

According to this formula, the total cross section should grow linearly with energy, if scaling holds.

This formula becomes much simpler if we average over the proton and neutron target and assume:

1) Callan-Gross relation for spin 1/2 constituents,[11]

$$F_1 = F_2/2x$$

2) Maximum interference of vector and axial vector current,

$$F_3 = -2F_1 \ .$$

Then

$$\frac{d^2\sigma^{\nu}}{dxdy} = \frac{G^2S}{2\pi}F_2(x,Q^2)$$

$$\frac{d^2\sigma^{\bar{\nu}}}{dxdy} = \frac{G^2S}{2\pi}F_2(x,Q^2)\cdot(1-y)^2 \tag{2.18}$$

The structure function F_2 is related to the one measured in eN scattering, if we take the simple quark parton model.

$$F_2^{eN}(x) \cong \frac{5}{18}F_2^{\nu N}(x) \tag{2.19}$$

The experimental observations[12] up to now seem to confirm this surprising relation (2.19) as shown in Figure

2.4a.

The energy dependence of the total cross section is consistent with the linear rise up to 200 GeV (Figure 2.4b). A more stringent test of scaling is possible by taking the average value of Q^2, which should also rise linearly with energy. This also is consistent with the data, but the simple relations of Eq. (2.18) seem to be violated.

Figure 2.4a

Mean Square Charge of Interacting Constituents (S=0)

$$\langle q^2 \rangle = \frac{\left[\int F_2^{\gamma N}\, dx\right]}{\frac{3\pi}{4G^2M}\,\frac{\sigma^{\nu}+\sigma^{\bar{\nu}}}{E_\nu}} = \frac{0.303 \pm 0.04}{\frac{\sigma^{\nu}+\sigma^{\bar{\nu}}}{E_\nu}}$$

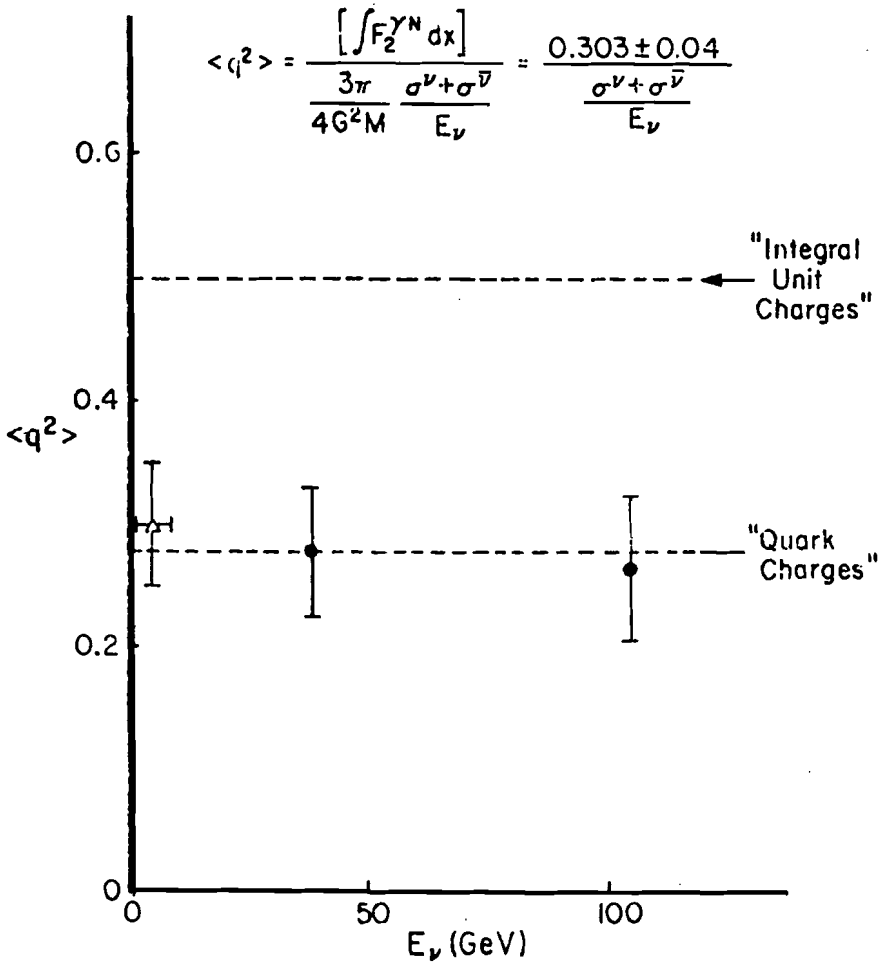

Figure 2.4b

$\sigma_T(\nu+N\to\mu+\text{hadrons})$

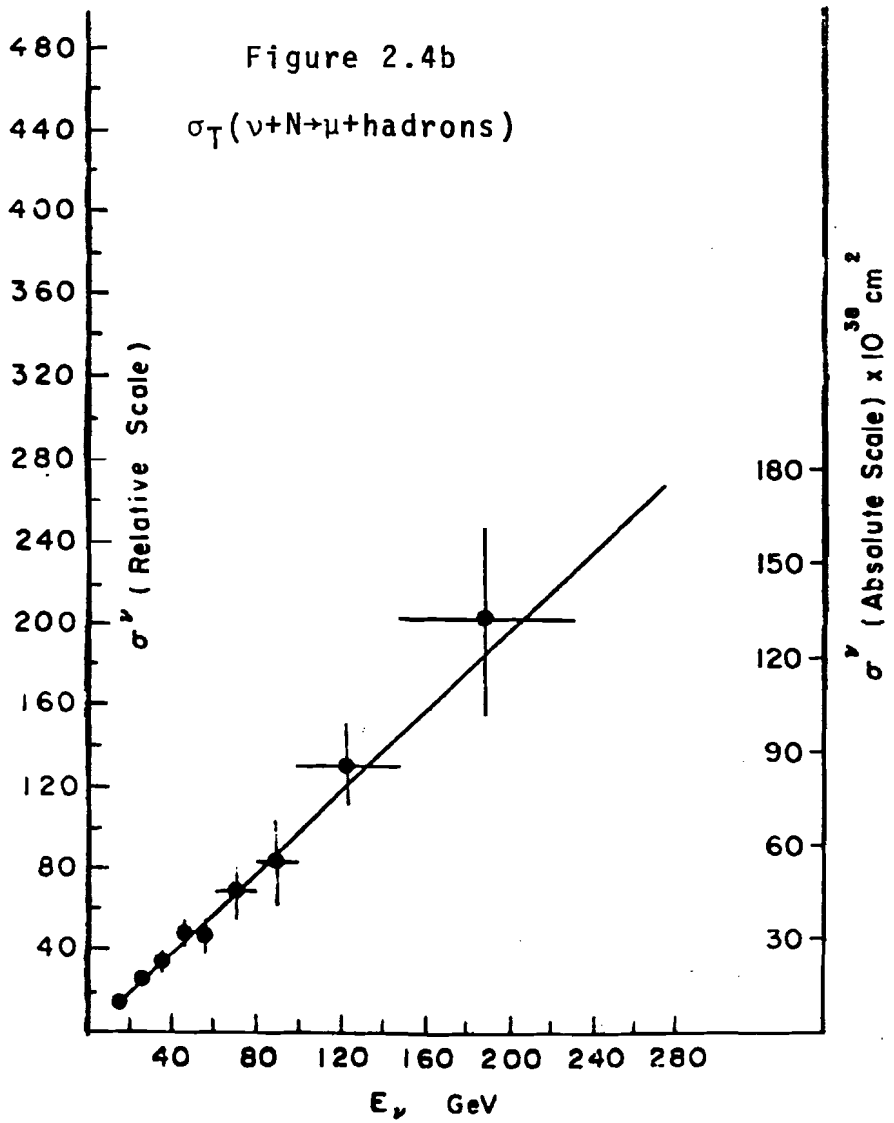

2. $e^+ + e^- \to \gamma^* \to N + \text{hadrons}$

The reaction can be related to the scattering in the space-like regions we discussed so far.

As before, we define two structure functions

$$\overline{W}_{\mu\nu} = \frac{4\pi^2 E_p}{M} \sum_f (2\pi)^4 \delta(q-P-P_f) \langle 0|J_\mu(0)|P_f\rangle \langle P_f|J_\nu(0)|0\rangle$$

$$= -(g_{\mu\nu} - \frac{q_\mu q_\nu}{q^2})\overline{W}_1(q^2,\nu)$$

$$+ \frac{1}{M^2}(P_\mu - \frac{pq}{q^2} q_\mu)(P_\nu - \frac{pq}{q^2} q_\nu)\overline{W}_2(q^2,\nu)$$

The kinematical region is shown in Figure 2.5.

In the colliding beam frame, the cross section is

$$\frac{d^2\sigma}{dE_p d\Omega} = \frac{2\alpha^2}{(q^2)^2} M^2 \sqrt{\frac{\nu^2}{q^2} - 1}\, [2\overline{W}_1 + \frac{2M\nu}{q^2}(1 - \frac{q^2}{\nu^2}) \frac{\nu\overline{W}_2}{2M} \sin^2 \frac{\theta}{2}]$$

In terms of scaling variable $\overline{\omega} = -2Pq/q^2$, and assuming Callan-Gross type relation[11] in the relativistic limit,

$$\frac{d\sigma}{d\overline{\omega}} = \overline{\omega}^2 F_2(\overline{\omega}) \cdot \sigma_{\mu\mu}$$

where F_2 is the scaling function similarly defined, and $\sigma_{\mu\mu}$ is the $e^+ + e^- \to \mu^+ + \mu^-$ total cross section.

As $\sigma_{\mu\mu}$ drops as $1/q^2$, the hadronic process should also have the same q^2 dependence, which was found to be badly broken.[7] Subsequently, new particles were discovered[8] and the observed constant cross section has been partly attributed to the threshold behavior due to the new

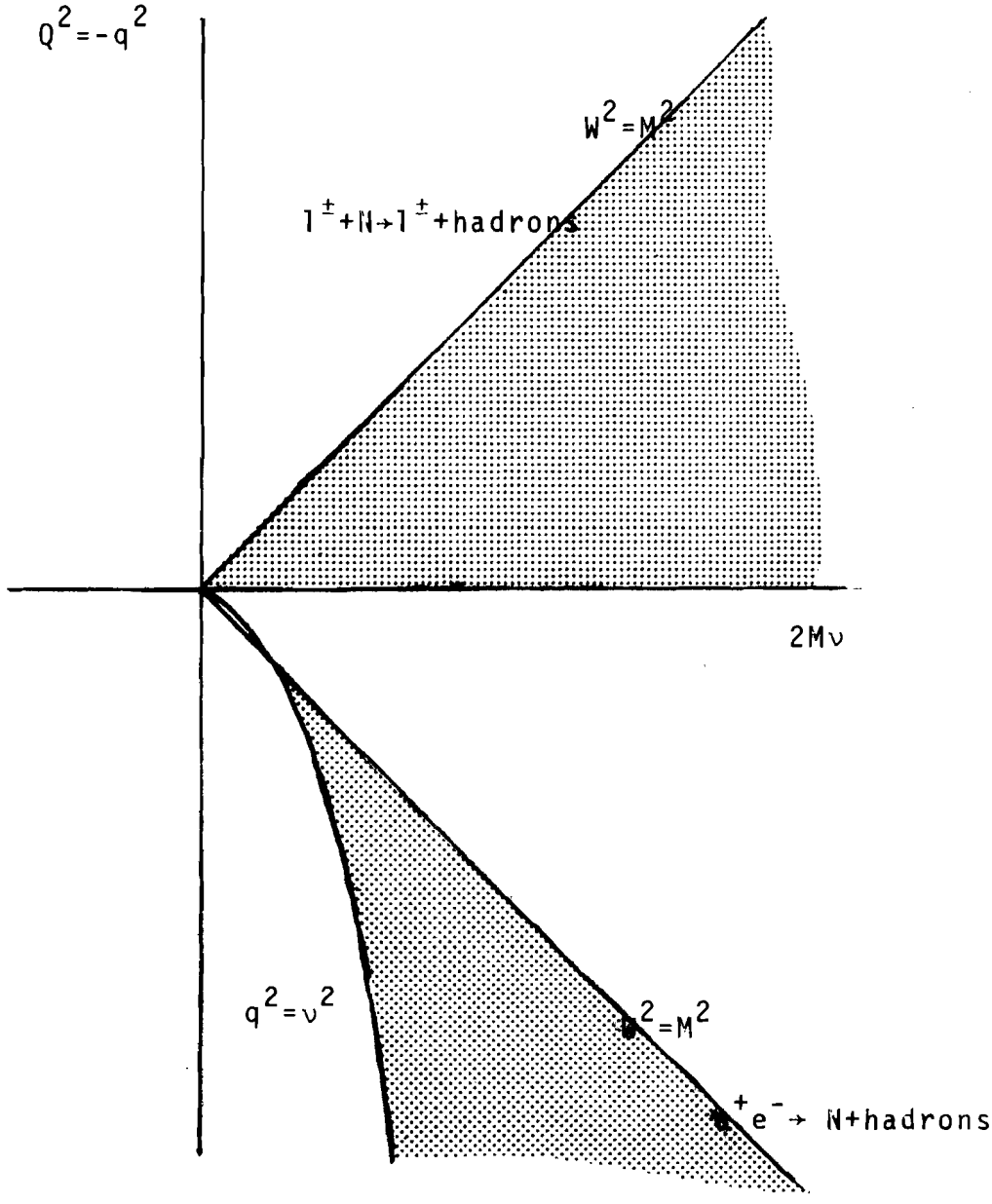

Figure 2.5 Kinematical region for $e^+e^-\to$ N+hadrons

channels. The latest result indicates that the q^2 dependence is consistent with $1/q^2$ above the threshold.[9]

3. Hadron + hadron $\rightarrow l^+l^-$ + hadrons

Considering that the l^+l^- pair is from the virtual photon of squared mass Q^2, the cross section can be written at high energy,

$$\frac{d\sigma}{dQ^2} = \frac{4\pi\alpha^2}{3Q^2} \tau W(\tau, Q^2)$$

$$\tau = Q^2/S \ , \qquad S \gg M^2$$

where S is the center-of-mass energy squared and

$$W(\tau, Q^2)$$

$$= -16\pi^2 E_1 E_2 \int dq\, \delta(q^2 - Q^2) \int dx\, e^{-iqx} \langle p_1 p_2^{(in)} | J_\mu(x) j_\nu(0) | p_1 p_2^{(in)} \rangle$$

W depends only on τ, if this process shows scaling behavior.

In the parton model, the virtual photon is created by the annihilation of a parton and antiparton in the incident hadrons. W is then the sum of the joint probability of finding pairs of the same type each from the colliding hadrons, and scaling is natural from the assumed point-like nature of the parton annihilation process.[5]

The parton model is, for most of the processes, a physical realization of the formal approach based on dominant signularities on the light cone. But the light cone analysis gives very different predictions for this process because the annihilation diagram is not light-cone dominated.

The process has been measured[13], but the current interest has been diverted from the scaling behavior due to the exciting discovery of new particles in this process also.

III. EXPERIMENTAL METHOD

Muons were obtained from the decay of pions and kaons produced by letting the 300 GeV extracted proton beam strike an aluminum target. The muon beam line consisted of four bend sections, alternately bending the beam to the west and to the east.

The typical intensity was $10^5 \sim 10^6$ muons per pulse and the halo was typically 40~100% of the beam intensity.

The muons were scattered from a solid iron target.

The position and the angle of the incident muons were detected by a proportional chamber system and the angle and the momentum of the scattered muons were reconstructed by a spectrometer consisting of iron toroidal magnets and wire spark chambers. The spectrometer had a large acceptance and azimuthal symmetry.

The trigger was the coincidence of the beam and the scattered muon vetoed by the beam veto downstream. Triggers were also produced by a random coincidence of the beam and a pulse generator, accumulating an unbiased beam sample, which was important to simulate the data by a Monte Carlo program to study the effect of the beam.

Data were taken at the incident energies of 150 and 56.3 GeV. The configurations were changed between the two energies so that the acceptance and the resolution were

independent of incident energy.

Most of the systematic errors cancel in comparing the two sets of data taken at the two energies resulting an increased sensitivity in testing Bjorken scaling.

Schematic diagram of the two configurations are shown in Figure 3.1. The characteristics of the experiment are summarized in Table 3.1.

In this section a brief description of the apparatus is given. A more detailed description can be found in Appendix A.

Figure 3.1a Schematic of the Apparatus
(150 and 56.3 GeV)

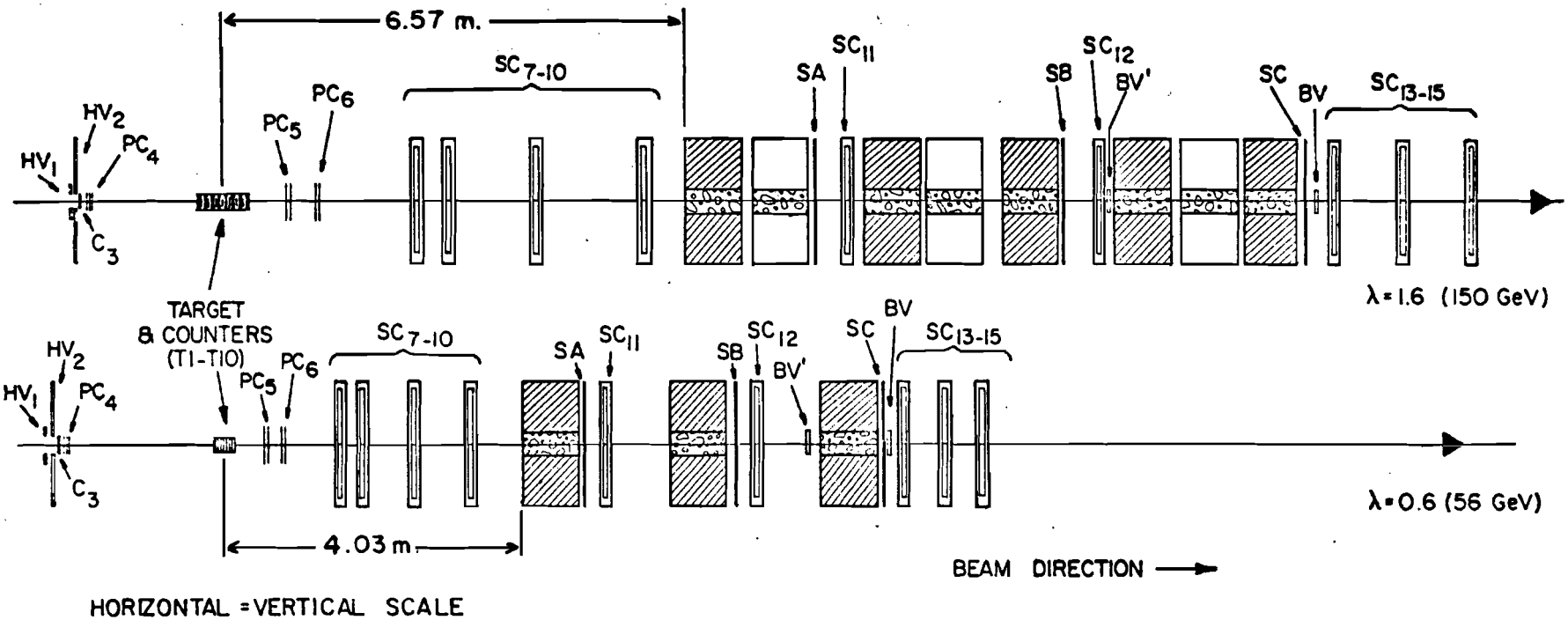

Table 3.1. Characteristics of the Experiment

Purpose	Test of Bjorken scaling in deep inelastic muon scattering at Q^2 up to 45 $(GeV/c)^2$ and ω up to 50.
Method	Apparatus was scaled so that events with fixed scaling variables go through the same point in the detector independent of incident energy.
Beam	Muon beam at 150 and 56.3 GeV at the Fermilab. Typical intensity of $10^5 \sim 10^6$ muons/pulse within 9 cm radius and 2 milliradians. Halo/beam = $0.4 \sim 1$ Spill length = $200 \sim 600$ milliseconds
Acceptance	Azimuthally symmetric. Greater than 50% for Q^2 between 10 to 40 (GeV/c). See Figure 3.2b.
Spectrometer	Consists of wire spark chambers, trigger counters and solid iron magnets. Field about 18 kilogauss. Momentum resolution $\sim$17%.
Target	Iron of thickness proportional to E_μ. (31" for 150 GeV, and 11.6" for 56.3 GeV).
Beam chambers	Proportional chambers
Trigger rate	$2 \sim 5 \times 10^{-5}$/muon
Data taking	August and October in 1973 and April in 1974.

A. Scaling the Apparatus

The experimental counting rate at scaling variables of measured x_m and y_m at an incident energy E_o ($\propto S$) can be written as an integral over the true values x and y.

$$\text{Rate } (x_m, y_m, E_o) \propto \int dx\, dy\, S \frac{d^2\sigma}{dxdy} A(x,y,E_o) \mathcal{S}(x,y,x_m,y_m,E_o) \tag{3.1}$$

where the integrand is the product of the cross section, acceptance and the smearing function. S is proportional to the target thickness.

Smearing is mainly due to the limited E' resolution of about 17% and the Fermi motion of target nucleons.

Recalling Eq. (2.15), S times the cross section becomes a function of x and y only if Bjorken scaling holds. If the experimental functions A and $\mathcal{S}$ are made independent of E_o, the counting rate at any measured x_m and y_m becomes independent of E_o. This was realized between 150 and 56.3 GeV; namely,

$$\begin{aligned} A(x,y,150) &\cong A(x,y,56.3) \\ \mathcal{S}(x,y,x_m,y_m,150) &\simeq \mathcal{S}(x,y,x_m,y_m,56.3) \end{aligned} \tag{3.2}$$

In order to understand this, we consider the following scaling transformation.

$$\begin{aligned} s &= \lambda s \\ Q^2 &= \lambda Q^2 \\ \nu &= \lambda \nu \qquad (\lambda = \text{a real positive constant}) \end{aligned} \tag{3.3}$$

The scaling variables x and y are fixed under this transformation. In the laboratory frame these can be written as

$$E_o = \lambda E_o$$
$$E' = \lambda E' \qquad (3.4)$$
$$\theta = \theta/\sqrt{\lambda} \quad (\theta << 1)$$

The last relation can be realized by

$$Z = \sqrt{\lambda} Z \qquad (3.5)$$

where Z is the longitudinal separation along the beam line between any two detectors.

The E' resolution is dominated by multiple scattering in the iron, and is roughly written as

$$\Delta E'/E' = \theta_{mult}/\theta_{bend} = (N_{all})^{\frac{1}{2}}/(N_{on})$$

where θ_{mult} and θ_{bend} are the rms multiple scattering angle and the bend angle, N_{all} and N_{on} are the number of all the magnets and that of "on" magnets, respectively.

Choosing $\lambda = 3/8$, the resolution was made the same, given an approximate relation of

$$\Delta E'/E = \sqrt{8}/5 \cong \sqrt{3}/3$$

In realizing this, extra material was required for the 150 GeV configuration, and three magnets were fully degaussed.

The acceptance and position dependent bias were made equal by requiring that the events with the same x and y go through the same point in each detector independent of E_o.

The realization of this is illustrated in Figure 3.1b, which was obtained by expanding the longitudinal coordinates of the 56.3 GeV configuration such that detectors were at the corresponding positions with the 150 GeV configuration.

The scaling of the apparatus cannot be realized exactly because of the discrete number of components. The position of magnets were adjusted to make the mean and the sigma of actual distribution about the ideal point approximately equal at each detector.

Rails were laid along the beam line to move the detectors with ease to change the configuration according to the incident energy.

Figure 3.1b
SCALE TRANSFORMATION OF MUON SCATTERING APPARATUS

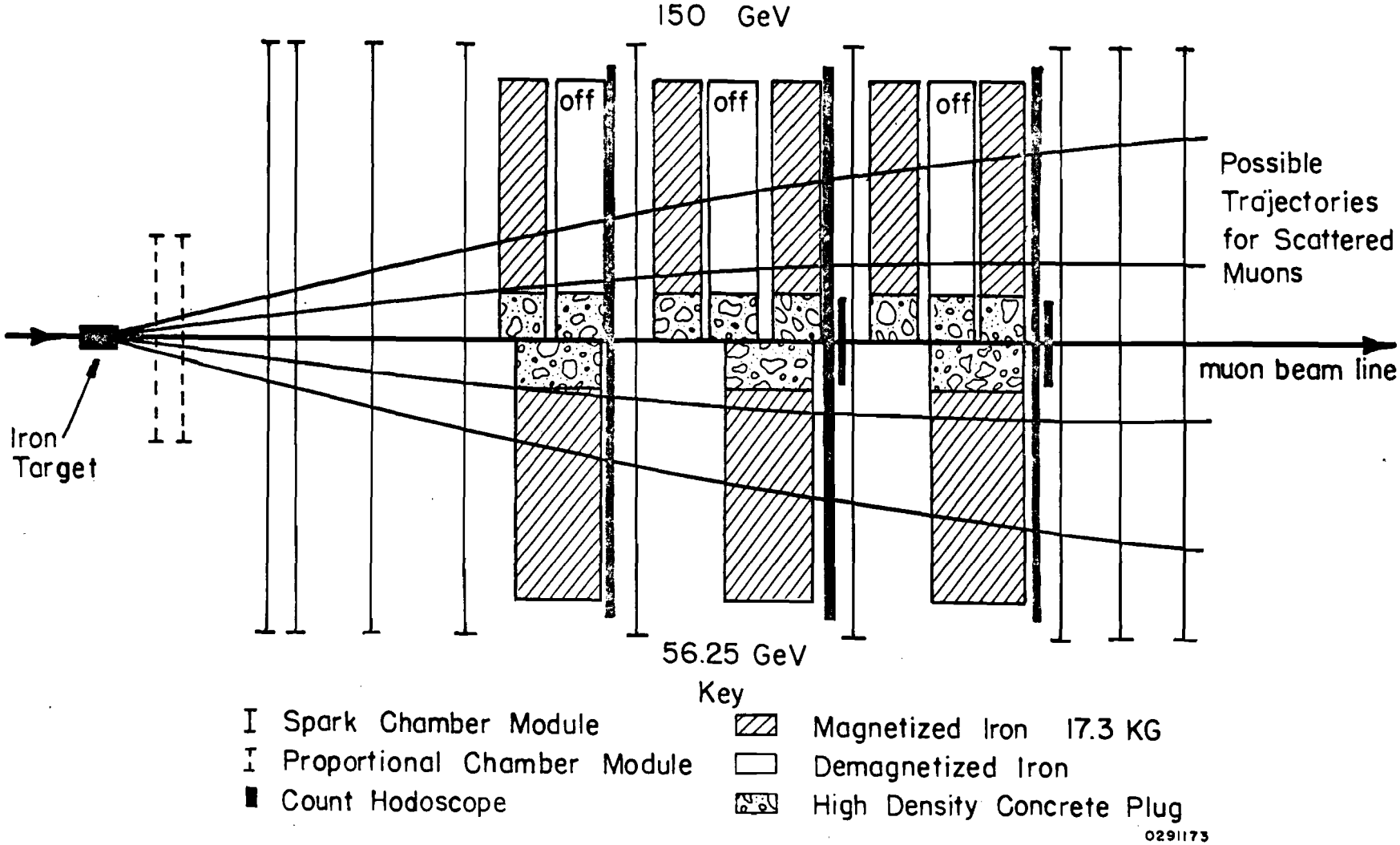

B. The Acceptance of the Apparatus

The acceptance of the apparatus can be best understood in the P-P_T plane.

The boundary of acceptance is determined by the inner and outer boundary of the fiducial region at each spark chamber module, which was defined to be well within the active region of magnets and spark chambers.

Given a scattered muon of momentum $P = E'$ and angle $\theta = P_T/p$, the mean radius of the track at a spark chamber module is

$$r = (P_T Z - M P_T^{bend})/P$$

where $P_T^{bend} \approx 0.4$ GeV/c exerted by a magnet, Z is the distance of the module from the target, and M is the sum of the distances from the module to each "on" magnet upstream. The condition $r_{min} < r < r_{max}$ is, in terms of P and P_T,

$$(P \cdot r_{min} + M P_T^{bend})/Z < P_T < (P \cdot r_{max} + M P_T^{bend})/Z$$

This condition is applied to all the modules, but the lower limit is essentially determined by the first and last module behind the iron magnets (modules #11 and 15), and the upper limit by the last four modules.

The effects of finite beam and multiple scattering in the iron magnets are to smear r_{min} and r_{max} by Δr_{beam} and $M_o \cdot P_T^{mult}/P$ respectively. $P_T^{mult} \approx 0.1$ GeV/c per one magnet, and M_o is similarly calculated as M for all magnets upstream.

The smearing of r_{max} is small but that of r_{min} is substantial.

Figure 3.2 shows the generated events according to the cross section and the accepted events passing all the cuts described later in the P-P_T plane and in the Q^2-ν plane.

By changing the distance between the target and the spectrometer, different parts of the kinematical region can be investigated.

The acceptance denoted by LA (SA) was obtained by placing the target closer to (further from) the spectrometer. The distance was scaled for 56.3 GeV, so the acceptance was the same as that for 150 GeV in the scaled variables. A consistency check among these data gives a limit to possible systematic effects due to the apparatus and the analysis.

The main discussions in this paper are confined to the LA data.

Figure 3.2a Generated Events in Q^2-ν plane (150 GeV)

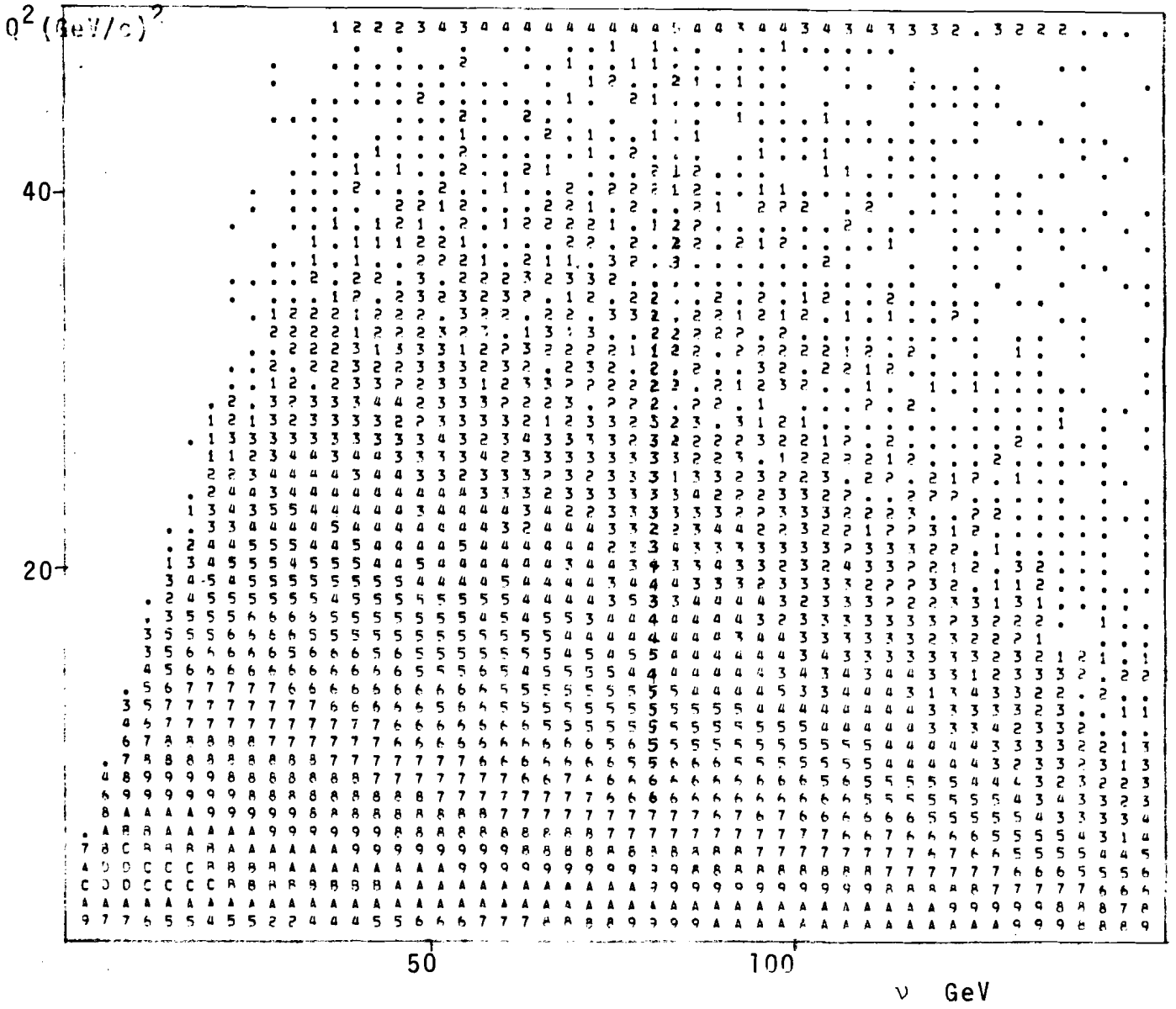

10^{10} muons
30" iron target
assumed.

(power of 2)

Figure 3.2b Acceptance in Q^2-ν plane (150GeV LA)

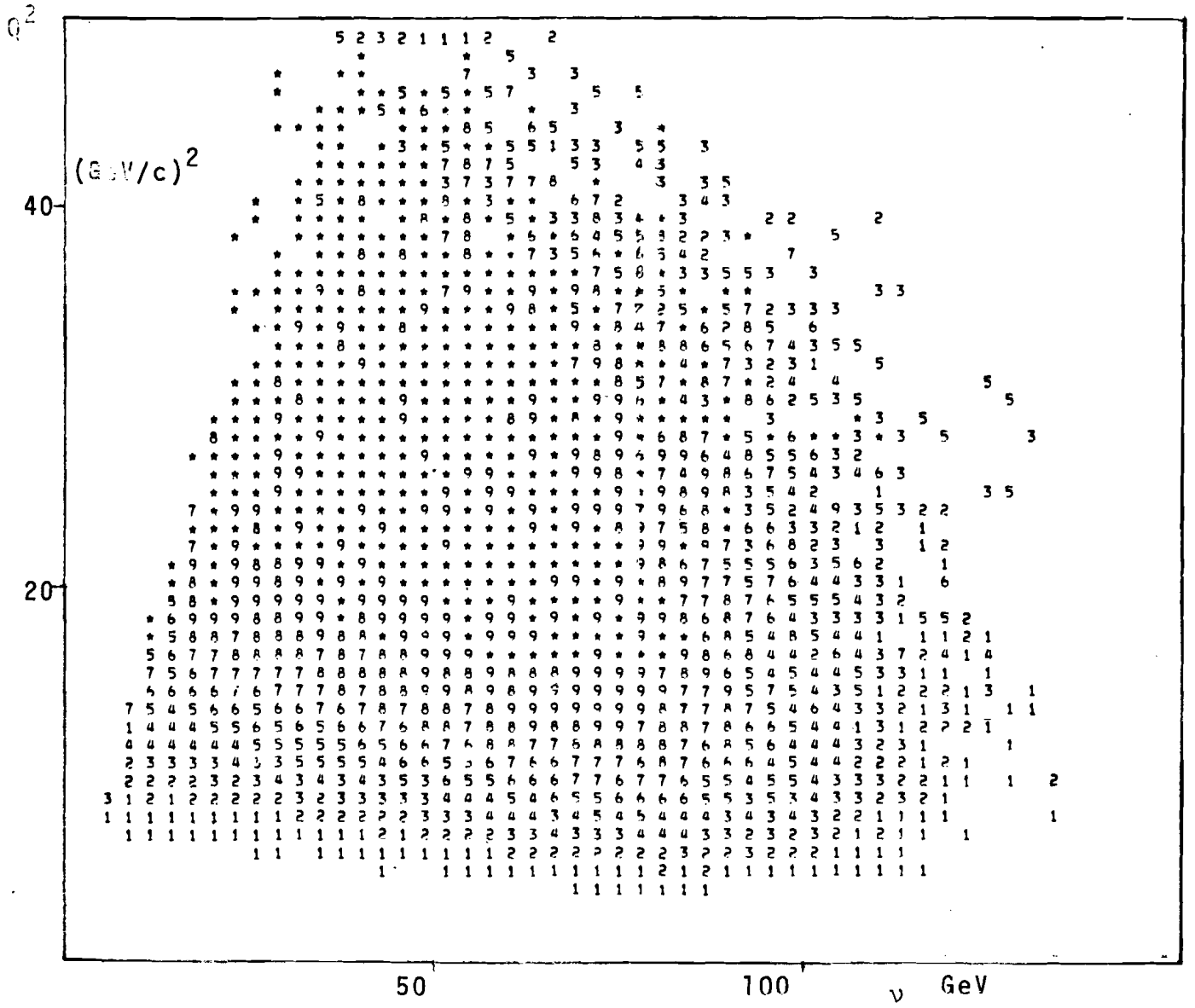

* = 100 %
9 = 90 %
etc.

Figure 3.2c

P-P_T plane

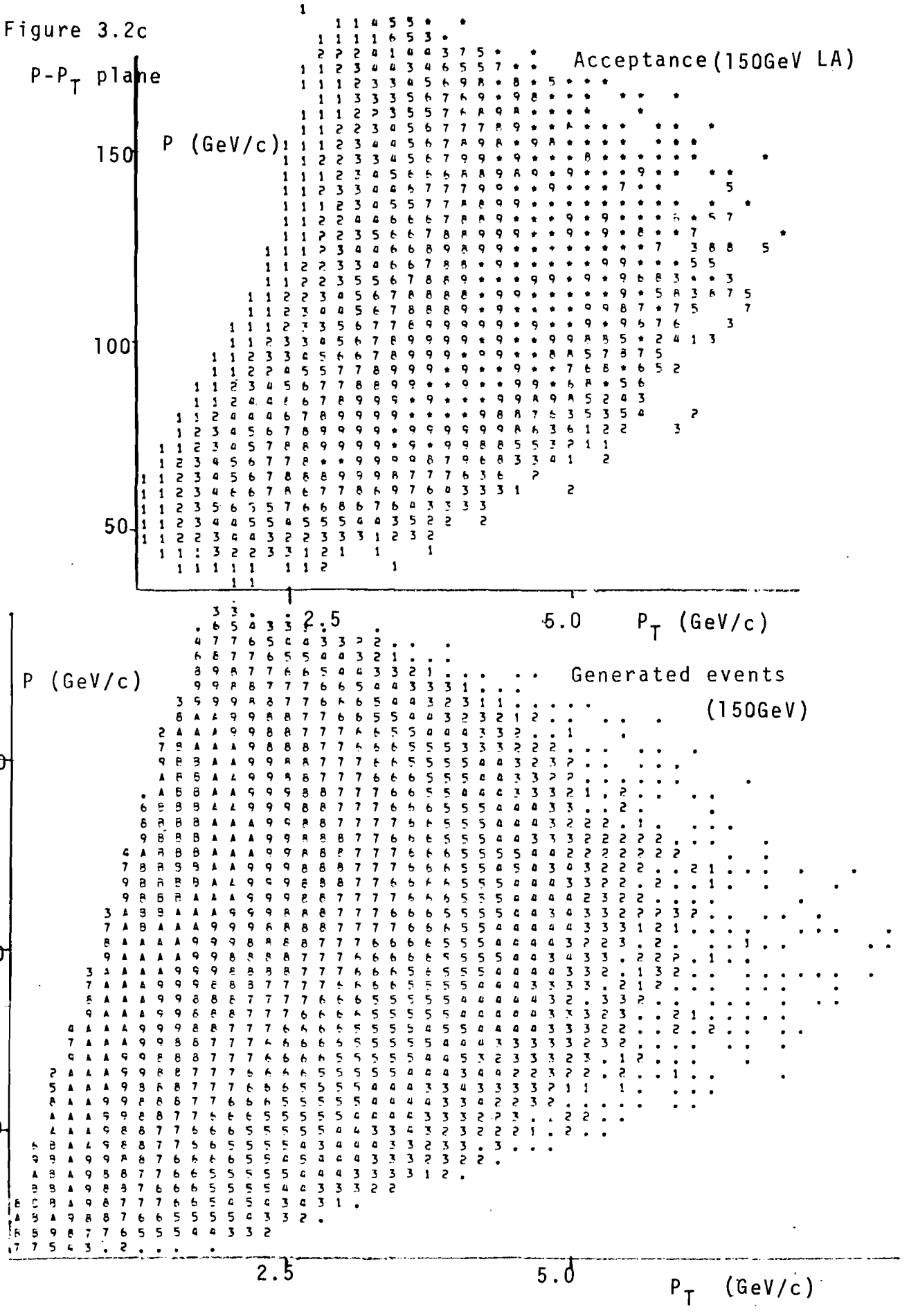

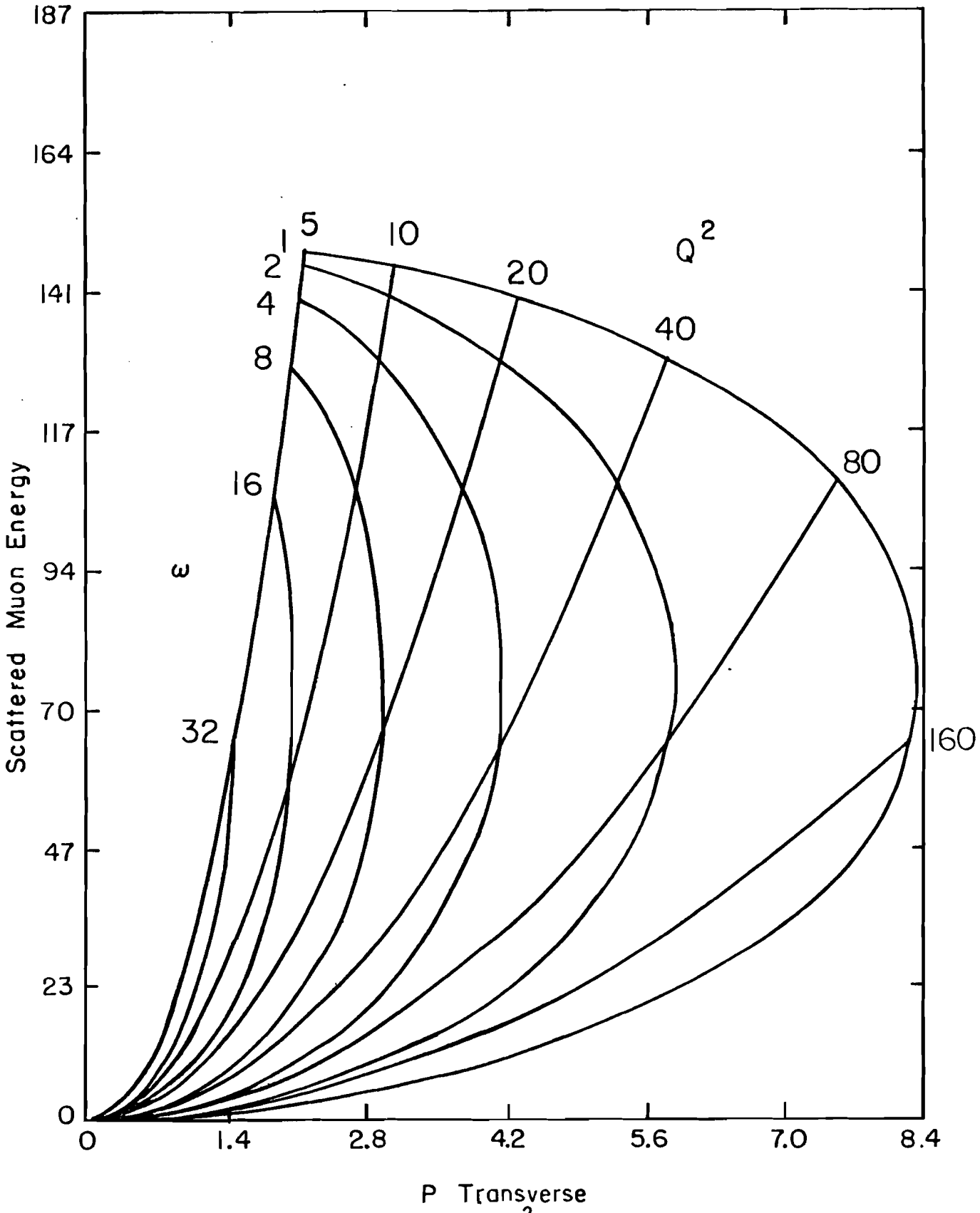

Figure 3.2d The constant Q^2 and ω lines in the P-P_T plane

Figure 3.2e. Acceptance in $Q^2 - \nu$ plane (SA)

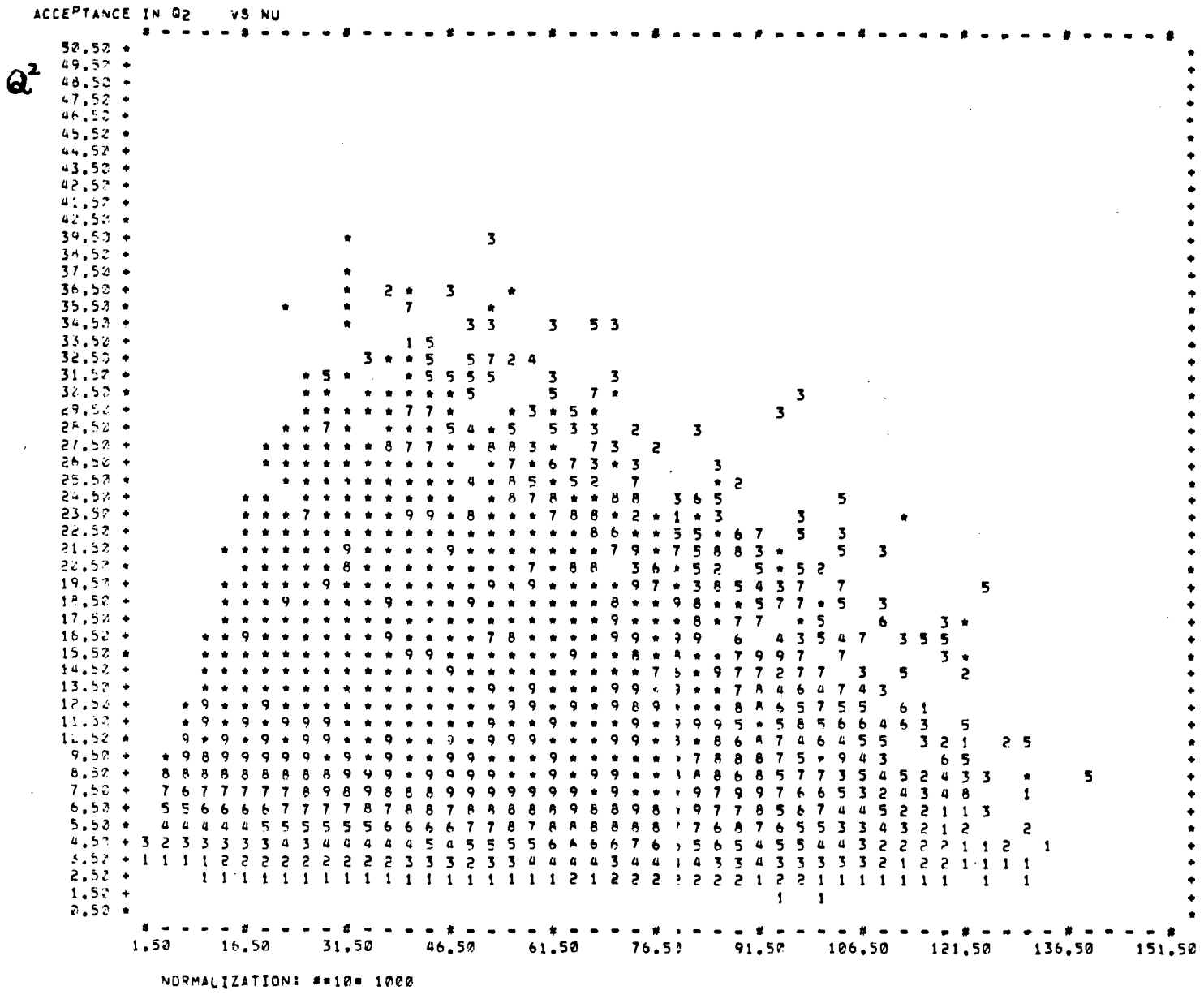

ν

C. Muon Beam

Muons were obtained from the decay of pions and kaons produced by letting 300 GeV extracted proton beam strike a 12" long aluminum target at Fermilab. The produced hadrons were focused into the 400 m long evacuated decay pipe, and the muons were captured and transported by the bending and quadrupole magnets as shown in Figure 3.3. The remaining hadrons were absorbed by 40' of polyethylene imbedded in the aperture of the bending magnets.

A typical beam intensity at the scattering target was about $2 \sim 10 \cdot 10^5$ muons/pulse, with one pulse every 6.25 seconds. Halo tracks into the spectrometer were typically 40 to 100% of the beam intensity and about half of the triggers were due to halo-beam accidental coincidence. Also about 30% of the scattering events were accompanied by extra tracks in the spectrometer. The separation of halo from events was almost unambiguous, as described later.

Most of the data were taken with positive muons. The intensity of negative muons was reduced by $\sim 1/3$ due to the production mechanism.

The pion contamination in the beam was measured[14] to be less than 10^{-5}. This was not a problem because the target and the solid iron magnets worked as an additional hadron shield.

Characteristics of the beam are summarized in Table 3.2.

Figure 3.3

SCHEMATIC OF MUON BEAM AND BEAM DETECTORS

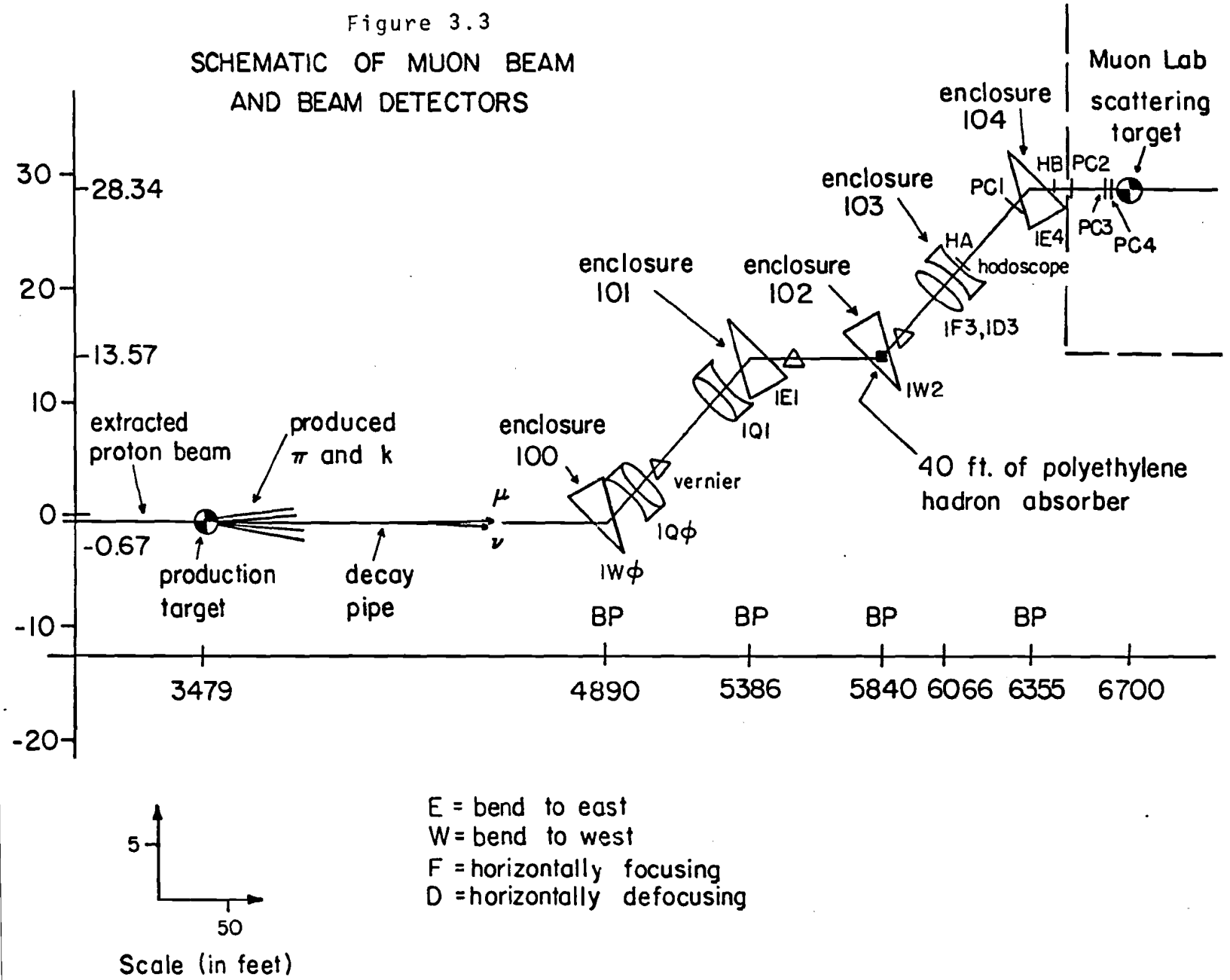

0810375

Table 3.2

Beam Characteristics

Extracted Proton Beam	
Energy	300 GeV
Spill	200~600 m sec.
Intensity	$3 \sim 8 \cdot 10^{12}$ protons/pulse
Repetition rate	6.25 sec/pulse
RF structure	19 n sec/bunch
Front end	
Train load (see Appendix A)	Dichromatic train and Triplet train
Production target	0.375"x1.5"x12" aluminum
Production angle	0 degree
Decay pipe	12" diam. 1327 feet
Energy of secondary hadron	156 GeV ±10% 62 GeV ±10%
Muon beam	
Energy	150 and 56.3 GeV ±1.5~2%
Intensity	100~500 k muons/pulse
Yield (μ/P)	10^{-8} to 10^{-7}
Occupation probability	0.5~3 %
halo/beam	0.4~1.0
π/μ	$10^{-5} \sim 10^{-6}$
Beam size	3cm x 4 cm (150 GeV) 4cm x 5 cm (56.3 GeV)

D. Targets

Most of the data were taken with an iron target of thickness 30.92" (11.6") at 150 GeV (56.3 GeV). The thickness was made proportional to the incident energy for scaling purposes.

The target was divided into 8 blocks of equal thickness 8"x8"x3.95" (1.48" for 56.3 GeV) and each block was followed by a 1/4" thick 8"x8" scintillation counter to help identify the vertex location. The signals from these target counters were fed into a Lecroy 8-channel analog to digital converter (ADC) to analyze the pulse height.

The choice of iron as the target is a compromise between the event rate at high Q^2 and relatively low Z material.

The nucleus can be regarded in our experiment as an assemblage of free protons and neutrons, which are moving in the nucleus.

The structure functions smeared by this internal motion of nucleons are a function of the scaling variable ω only and the motion gives a scaled contribution at the two energies.[15]

Another effect of using heavy nuclei is the background due to the wide angle bremsstrahlung.[16] This contribution is also a function of ω only.

Besides the iron target, a carbon target of 8"x8"x14.06" was placed at 56.25" upstream of the main target at 150 GeV (scaled values at 56.3 GeV), in an attempt to check possible

nuclear effects. These targets were placed on a target cart which could easily be moved along the beam line. The target cart also contained a halo veto bank, one of the beam trigger counters, and several proportional chamber modules.

Figure 3.4 shows the geometry of the target cart.

Data were accumulated by moving the target cart to several positions along the beam line, illuminating different regions of the spectrometer with the same physics.

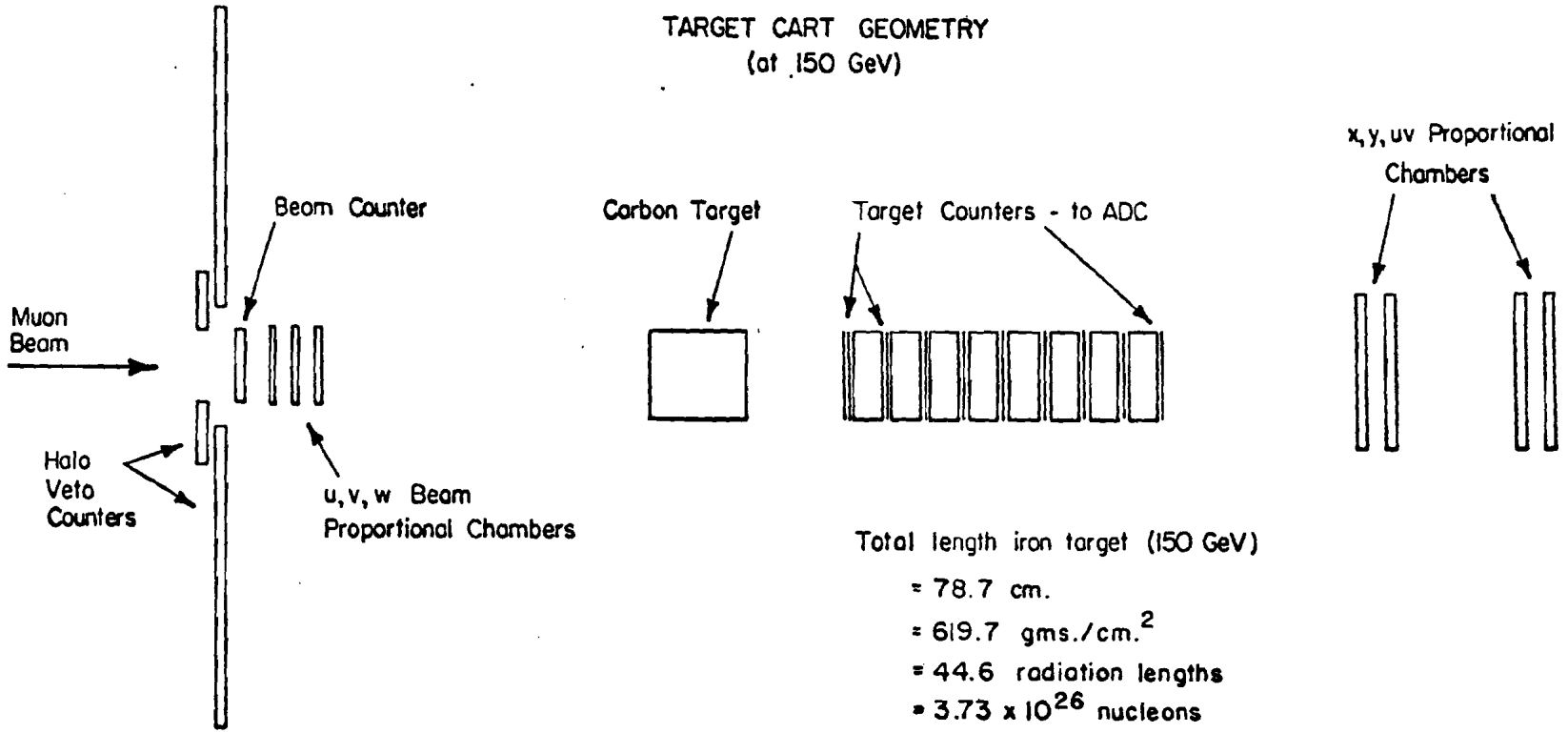

Figure 3.4

029

E. Iron Core Magnet

Because of the high penetrability of muons, it is possible to use magnetized iron as a momentum analyzer.

The advantage of the iron magnets are their low cost and ease in construction and operation. Also they work as a hadron filter absorbing pions etc. from hadron showers.

The azimuthally symmetric field provides a large acceptance and ease in track reconstruction and data simulation.

A chief disadvantage is its poor momentum resolution of about 17% because of multiple scattering through the iron. Also important is the occasional electromagnetic shower associated with the scattered muon tracks, making the reconstruction of tracks ambiguous. This point is discussed in detail in Appendix C.

The iron core magnets were toroidal with a 12" ID, 68" OD and 31" thickness.

Four 7 $\frac{3}{4}$ " thick plates were welded together to make one magnet as shown in Figure 3.5.

Approximately 16,000 Amp-turns give an average field of about 18 kilogauss with the radial dependence shown in Figure 3.6.

This was measured in two ways which agreed to better than 1%. One method used a precisely machined toroid of the same batch of iron as the magnets. A B-H curve obtained from this was projected to B vs r of the main magnets.

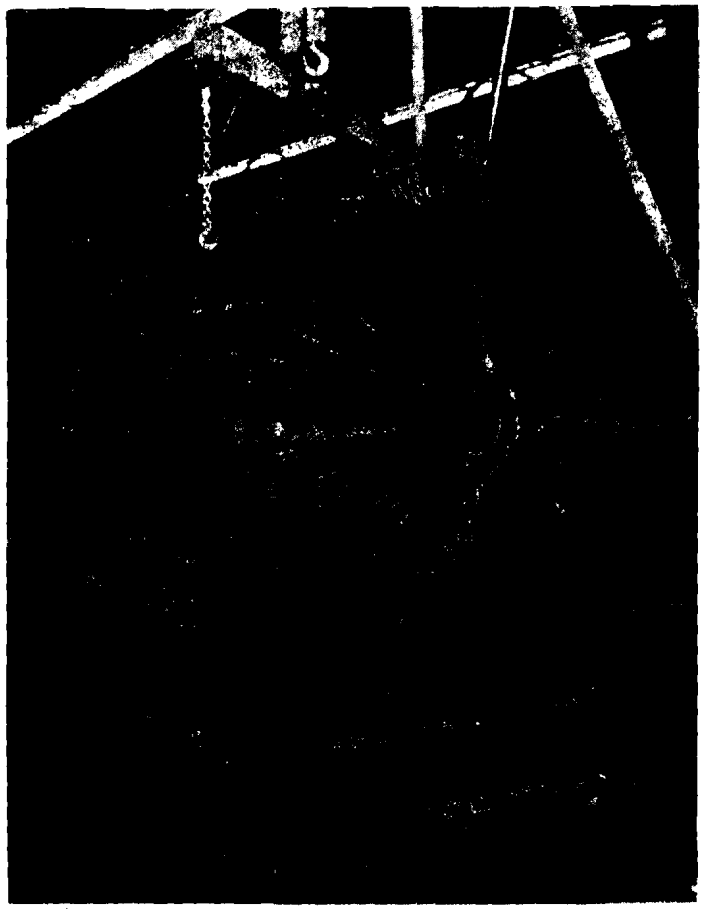

Figure 3.5

Iron toroidal magnets and
the supporting structure

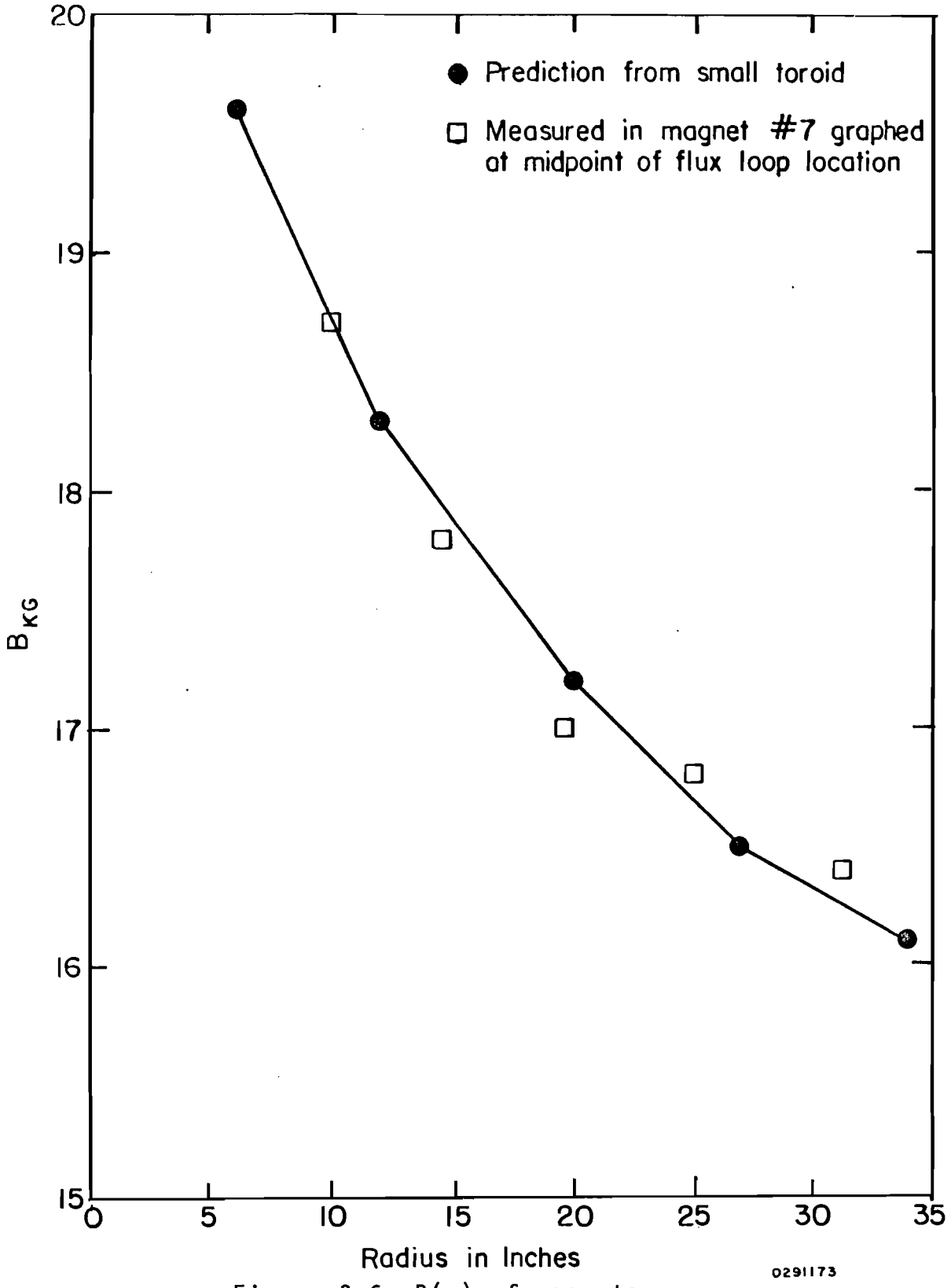

Figure 3.6 B(r) of magnets

The second method was to measure B(r) directly by drilling holes through the $7\frac{3}{4}''$ plates of the main magnets and measuring the induced voltage on a coil wound around the holes.

It is also important to know how well we can degauss the magnets because additional material was needed for the scaling purpose. This was monitored in several ways during the long degaussing cycle. The voltages were alternated in a slow time scale with slightly reduced amplitude at each step. The procedures and checks are found in S.Herb's thesis.[17]

The spectrometer was calibrated at each configuration by deflecting the incident beam of known energy into the spectrometer with the help of specially constructed small toroidal iron magnet. This is discussed in Appendix D. Figure 3.7 shows the result of the calibration.

Table 3.3 summarizes the important parameters of the magnets.

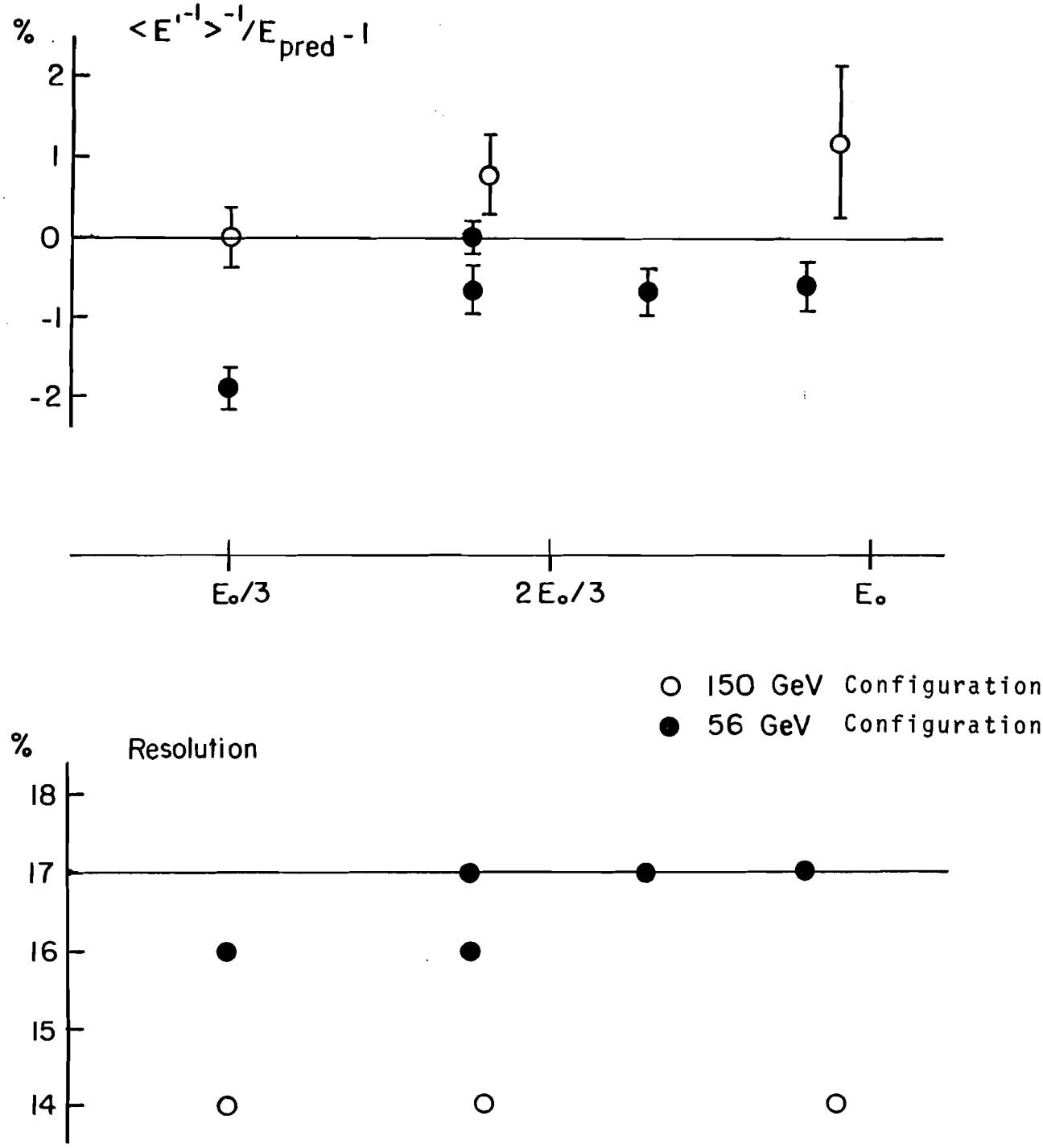

Figure 3.7

Calibration of the spactrometer (BACKFIT)

Table 3.3 Parameters of Iron Core Magnets

size	12"ID x 68"OD. Four 7.75" thick plates welded at the side.
wire	#8 wire, 450 turns
current	33 to 35A
cooling	water cooled aluminum and copper shell in the hole
B(r)	about 18 K Gauss (Fig. 3.6)
P_T (bend)	$\sim$0.4 GeV/c per magnet
P_T (mult. scat.)	$\sim$0.1 GeV/c per magnet
energy loss per magnet	about 1.3 to 1.8 GeV (slight increase with momentum)
B(r); measurement	1. A B-H curve of a small toroid of the same material was projected to B(r). 2. Directly drilled holes in the magnets and measured induced voltage on a wire wound around the holes.
calibration	Sent beam of known energies into several radii of the magnets.
E' resolution	15 to 17 %

F. Proportional and Spark Chamber System

1. Proportional Chamber System

Three sets of proportional chamber modules were used to reconstruct the incident beam tracks. Two modules consisted of three chambers at 120° to each other to help remove the ambiguity in reconstructing more than one beam track.

Two sets of larger size were placed downstream of the target to detect scattered muons.

The signals from each wire were amplified at the chamber and transported to a latch system by ribbon cables.

The signals were latched in when the proportional chamber (PC) strobe signal fired. The PC strobe was a counter coincidence which was a part of the trigger and fast enough to meet the signals from the chambers (Figure 3.8). Reset and gate signals were made from the PC strobe and fanned out to each latch card.

Several measures were taken to avoid latching wrong beam tracks. The reset signals were narrow but had a dead time of 120 ns so as not to be reset by the next few tracks. The PC strobe was gated by the event trigger as soon as the trigger was formed which was 90 ns later than the PC strobe, to avoid picking up spark chamber noise. Also in order to make sure that the gates were opened properly, one of the

PC strobe gate signals was fed into a discriminator coincidence register (DCR). The efficiency was found to be 99%.

The details of chamber construction and operation are given in Appendix A.

2. Spark Chamber System

The wire spark chamber system consisted of nine modules. Each module contained two gaps or four planes rotated by 45° to each other to remove ambiguities that occur when more than one track go through.

The active region is slightly larger than a 72" diameter circle to cover the magnets. The center of the chambers for those behind the iron magnets had a dead region of 12" diameter to avoid registering beam tracks.

The spark chambers were triggered by the main trigger signal described in the next section, and the chambers were fired about 300 ns after a track went through.

Clearing field of +90V was constantly applied to the gaps to keep the memmory time short, which was about 1 μ second.

The dead time of the system was determined by the recharging of the high voltage power supply, and set to 40 m seconds.

Readout is through the magnetostrictive pick-up.

The position of the pick-up coil was alternated from module to module to minimize possible bias due to the attenuation of signals along the wire.

The signals were amplified, discriminated and fed into time digitizers. Up to eight sparks from a wand including two fiducials were digitized.

Table 3.4 summarizes the parameters of the proportional and spark chamber system.

The detail of the chamber construction and the operation is given in Appendix A.

Table 3.4 Proportional and Spark Chamber System

1) Proportional Chamber System

Mod#	z positions	coordi-nates	active area	function
1	-2680"	Y	7.5"x10"	measure E_0
2	-1499"	XY	7.5"x7.5"	beam chambers
3	-198.1"	UVW	7.5"diam.	beam chambers
4	-89.2"	UVW	7.5"diam.	beam chambers
5	22.8"	UV	12"x12"	detect scattered muon
6	33.1"	XY	15"x15"	detect scattered muon

note;UVW is 3 wire planes rotated by 120° to each other
UV is rotated by 45° from vertical
z of mod#5 and 6 were scaled for 56.3 GeV.

2) Spark Chamber System

Number of Modules	9
one module	2 gaps, 4 wire planes one gap rotated by 45°
number of planes (wands)	36
Active area	72"diam.

G. Counters and Trigger Logic

1. Trigger Logic

The trigger is a coincidence of the beam muon signal 'B' and the scattered muon signal 'S' vetoed by beam veto counters.

Besides this event trigger, a random coincidence between the beam and a pulse generator also caused triggers. This was to accumulate unbiased beam tracks for normalization purpose and to take out dependence on the beam shape in event simulation. Thus the trigger is;

$$\text{Trigger} = (B\ S\ \overline{BV})\ \text{OR}\ (B\ \text{Pulser})$$

where B = Beam, S = Spectrometer and BV is the beam veto to veto an unscattered muon. These are detailed below.

The schematic of the trigger logic is shown in Figure 3.8. Table 3.5 summarizes the counter system.

2. Beam Counters

The beam was required to go through the aperture of the last bending magnets in the beam line and then through the active region of the beam proportional chambers without being accompanied by halo tracks. The definition is

$$B = B_1\ B_2\ B_3\ (C_1\ C_2\ C_3)\ \overline{HV}$$

Three counters of $3\frac{1}{2}''$ diameter, B_1, B_2 and B_3, were placed at up-, middle- and downstream of the bending magnets in enclosure 104 to ensure that the incident

Figure 3.8a Schematic of trigger logic

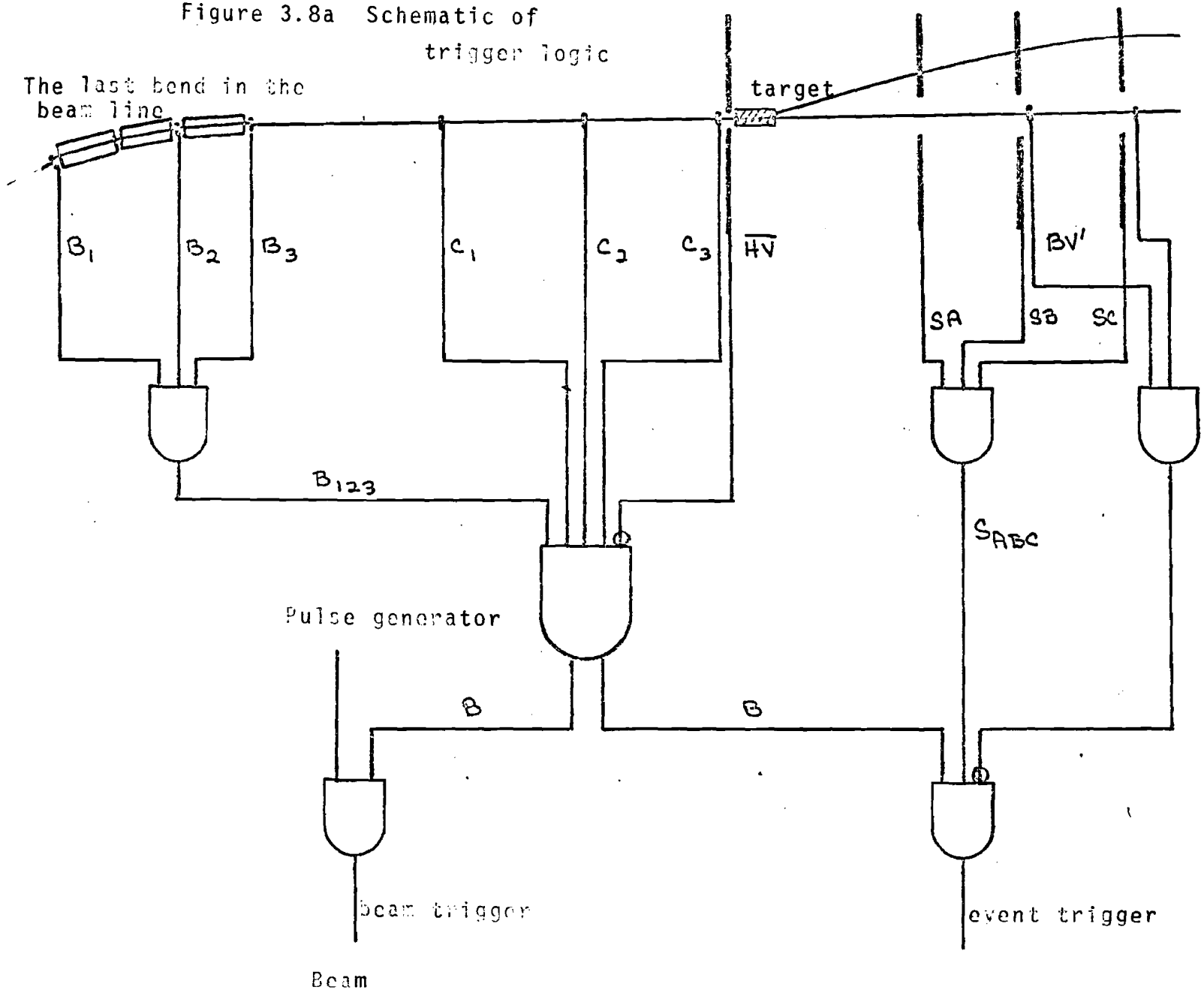

Figure 3.8b

TRIGGER LOGIC

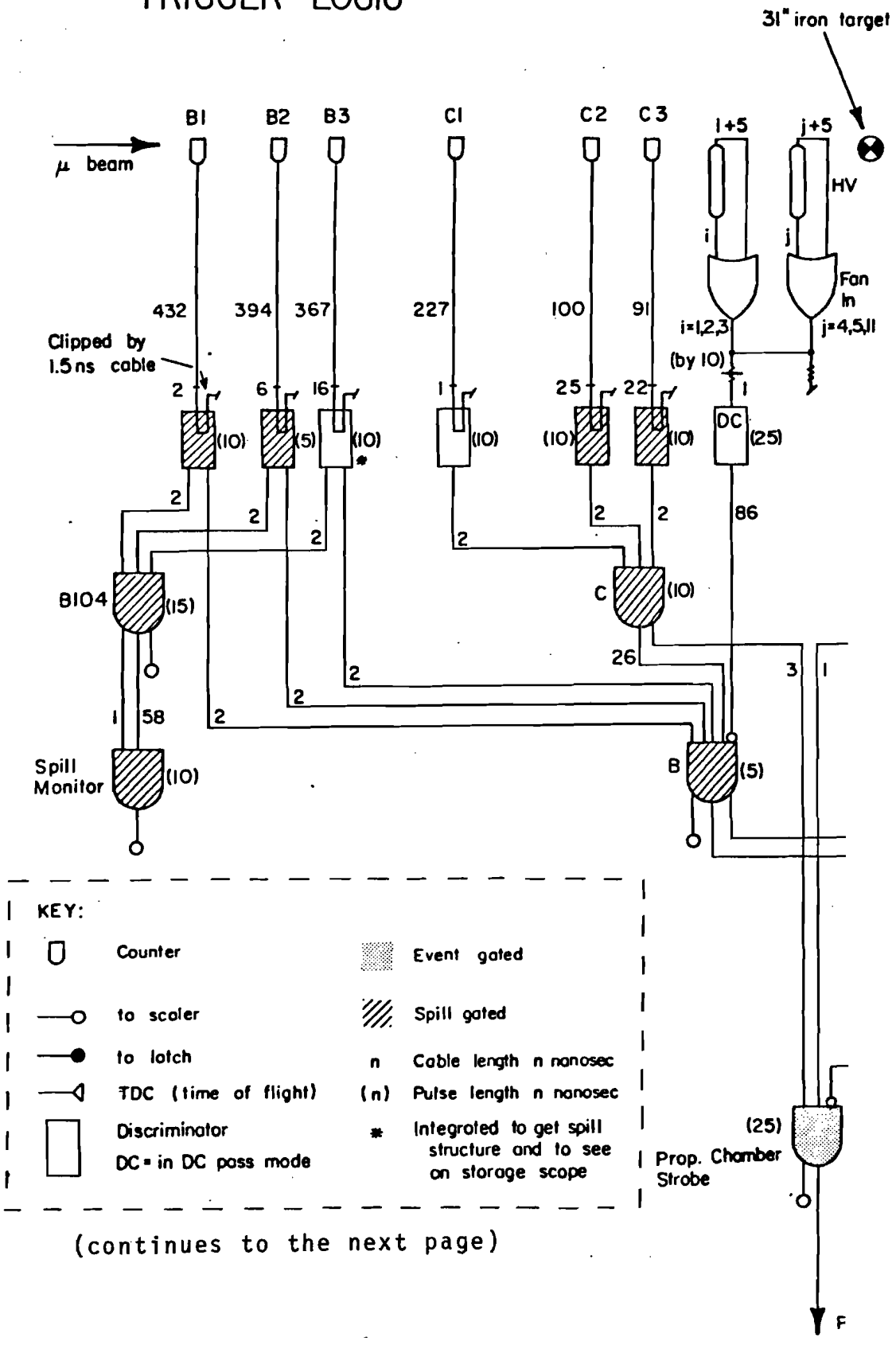

(continues to the next page)

Figure 3.8c (continued from the previous page)

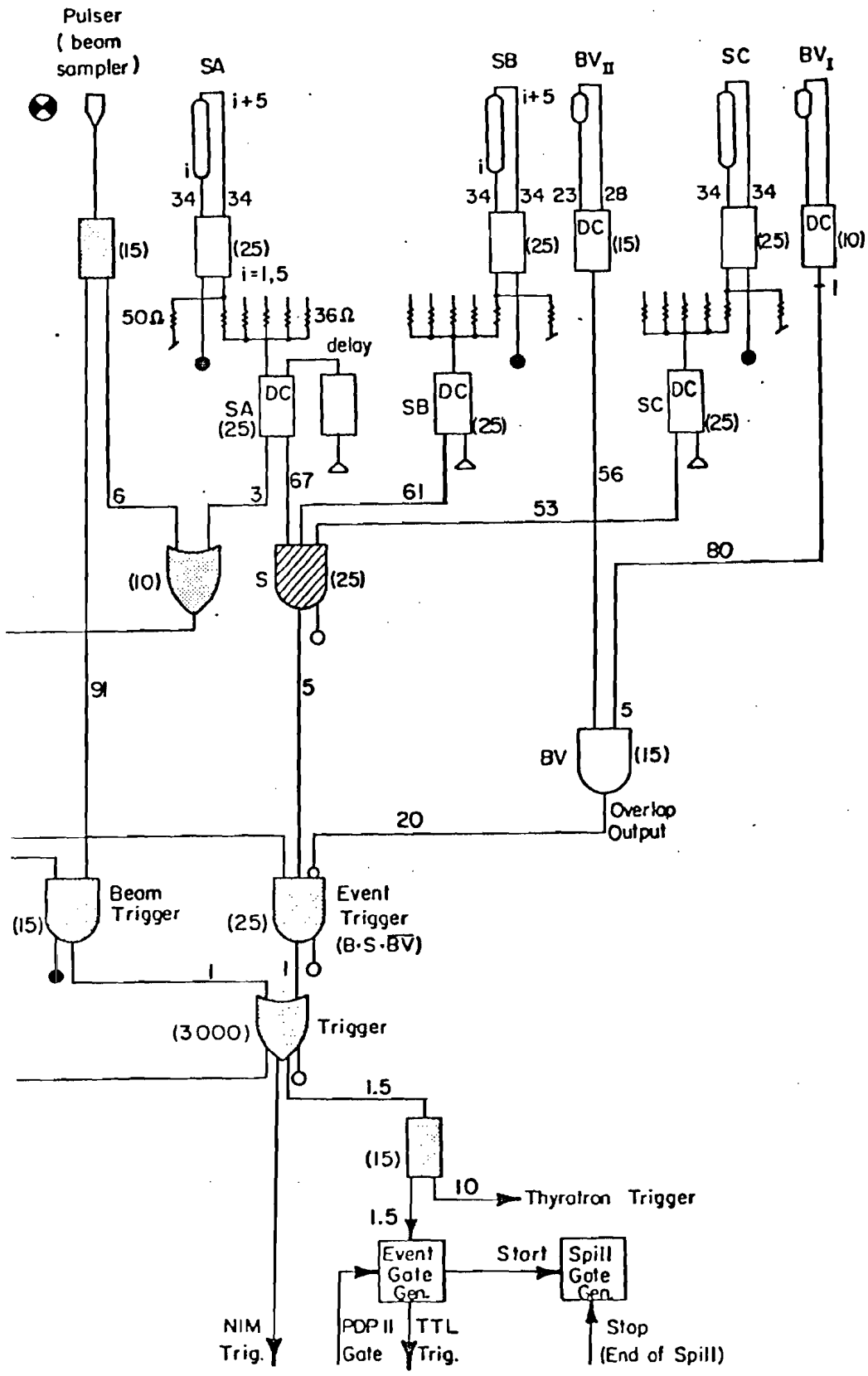

muons went cleanly through the 4" diameter aperture.

Three 7½" round counters C_1, C_2, and C_3 were placed at the face of each three sets of beam proportional chambers defining the active region of the chambers.

Beam tracks accompanied by halo tracks outside the beam region were vetoed by halo veto HV, mounted on the face of the target cart.

The active region of HV is slightly larger than 70" diameter and with a 7½" round hole in the center, sharply defined by a smaller counter with a hole in it for the beam (Figure 3.9).

Without HV, the trigger rate was increased typically by a factor of 5 to 10.

The signals from B_1, B_2, B_3 and C_1 were transported by fast cables (velocity $\sim$.97 c), so as not to delay the trigger significantly. The signals from B_1 through C_3 were clipped to 3 ns at the discriminator inputs.

Signals from the 12 tubes of HV were fed into a FAN-IN and then discriminated in the DC-pass mode.

3. <u>Spectrometer Counters</u>

A tripple coincidence of spectrometer counter banks SA, SB and SC defined the scattered muon signal. These counters were attached to 1/4" thick aluminum frames whcih were mounted behind the magnets. Thus these banks are well

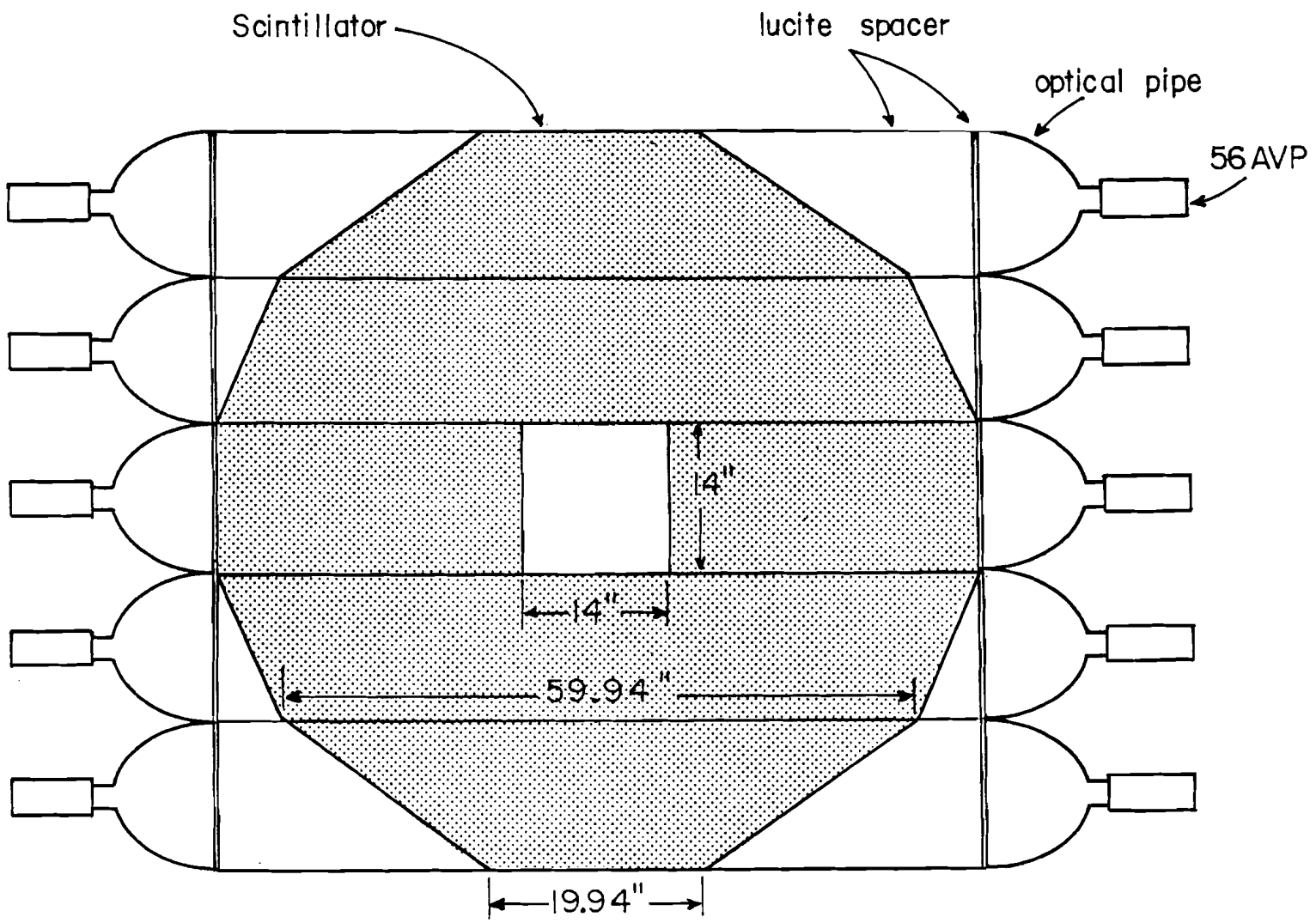

Figure 3.9

Halo veto and Spectrometer counter Bank

0810575

shielded from the hadronic and electromagnetic showers from the target. The construction of these banks is identical to that of the HV bank: the active region is slightly larger than 70" diameter with a 14" x 14" square hole in the center.

Each bank consisted of five 14" wide vertical bins with tubes looking from either side.

The signals from either end of the tubes were fed into parallel inputs of discriminators.

These five bins of a bank were added passively and then rediscriminated for the triple coincidence. Each bin was latched into a DCR to aid in selecting good tracks in the spectrometer in the analysis.

The efficiency of a counter bin in the triple coincidence was monitored by a small counter telescope, mapping the counters during the data taking.

4. Beam Veto Counters

It was necessary to veto unscattered beam muons in order to reduce the trigger rate to an acceptable level. Without BV, the rate was about 100 times higher and dominated by beam-halo accidental coincidences.

In order to prevent events which produce forward hadron showers from providing vetos, the holes in the magnets were plugged by high density concrete to absorb such showers before they would hit the veto counters. In order to monitor any bias produced, two beam veto counters placed after different

amounts of absorber were used in coincidence and the signals were latched separately.

Additional absorber put in front of the first magnet helped ensure that there was no appreciable trigger loss from hadron showers. This is further discussed in Appendix F.

The diameter of the veto counters was 12". Each was viewed by two tubes from either end, and the signals were fed into the parallel input of a discriminator in DC pass mode.

The overlap output from the coincidence of these two signals was used to veto the trigger. The use of the overlap output was necessary to eliminate dead time to ensure the stability of the trigger rate with respect to the intensity and the spill structure.

Accidental vetoing due to BV was monitored throughout the experiment, and was 0.5% to 3%. The figure is always about a factor of 2 higher than the probability of finding a beam muon in an RF bucket, which was monitored separately. This is because of the longer width caused by using DC pass mode.

5. Beam hodoscope counters

In addition to these counters participating in the trigger, signals from two sets of beam hodoscopes HA and HB were latched and written on magnetic tape. HA consisted of four 3" wide 8" high counters overlapped

as shown in Figure 3.10 to improve its resolution and placed at the downstream end of enclosure 103 where the CEA quadrupole magnets were housed.

HB consisted of four 1" wide, 4" high counters, and was placed at the downstream end of enclosure 104.

These hodoscopes were used in combination with the beam proportional chambers to determine the momentum of the incident beam muons.

These signals were clipped in the same way as those from the other beam counters.

Figure 3.10 HA Hodoscope

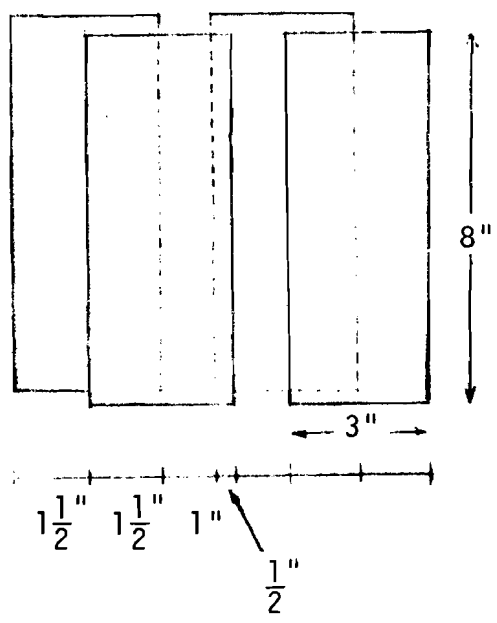

Table 3.5 Counter system

Name	Position	Active area	Photo-tubes	#	disc. width	Function
B1	US of E104	$3\frac{1}{2}$" diam.	56AVP	1	10 ns clipped	Define beam that goes through the bending magnets
B2	MS of E104		〃	〃		
B3	DS of E104		〃	〃	〃	
C1	At the Mod#2	$7\frac{1}{2}$" diam.	〃	〃	〃	Define the beam in the active region of the prop. chambers
C2	At the Mod#3		〃	〃	〃	
C3	At the Mod#4		〃	〃	〃	
HV_I	At the face of the target cart	see Fig. 3.9	RCA7850	10	25 ns DC pass	Veto halo tracks
HV_{II}		15"x15" 7.5"diam. hole	RCA7746	2		sharply define HV
SA	In the spectro-meter	see Fig. 3.9	56AVP	10	25 ns	Trigger on scattered muon
SB			〃	〃	〃	
SC			〃	〃	〃	
BV_{II}	At SB	12"diam.	56AVP	2	15 ns DC pass	Veto unscattered muon
BV_I	At SC		RCA7746	〃		
HA	DS of E103	Fig. 3.10	RCA8575	4	10 ns clipped	Beam hodoscope to obtain incident energies
HB	DS of E104	2"x4"x4				

Note; all the counters were 1/4" thick plastic

H. Scalers

Several scalers monitor the normalization and the dead time, and the rest monitor the stability of data taking.

All scalers were read into the CAMAC system and written on magnetic tape with other information. In addtion, some important scalers were monitored visually in the Muon lab.

As noted in Figure 3.8b, crates were gated in two ways. The gate for spill gated (SPG) crates stayed open during the spill on time and went off during the off time. The gate for event gated (EVG) crates closed whenever a trigger occurred until it was ready for another trigger.

The spill on-off signals were generated by a delayed pulse generator which produced appropriate pulses after receiving timing signal from the main ring. The dead time of typically 40 m seconds needed for the recharging time of the spark chamber power supply was set by an event gate generator which controlled the event gated crates receiving PDP11 gate signals and also provided open signals for a spill gate generator.

Scalers and the ratios monitored and their functions are summarized in Table 3.6.

The most direct measurement of the number of effective muons is $(B \cdot \overline{BV}_{delayed})_{EVG}$, the coincidence between B(beam) and $\overline{BV}$(beam veto) delayed by 60 ns (3 RF buckets), automatically correcting the number of usable beam buckets for the dead time and for the accidental vetoing due to the beam veto.

This accidental vetoing has a close relationship with the spill structure which was measured by $(B104 \cdot B104_{delayed})/B104$. B104 is the coincidence of B_1,B_2 and B_3 measuring the flux going through the last bending magnets in enclosure 104. The delay was also 60 ns and the ratio measured the probability of finding a muon in an RF bucket.

A several counter signals were latched into the Discriminat r Coincidence Register (DCR). The event trigger and pulser trigger were also latched in to avoid confusion.

Table 3.6a Scalers

Name	gating	meaning	typical value
SEM	EVG	Incident proton flux at the prod. target	$1\sim8*10^{12}$/pulse
B	EVG	# of beam muons in the event gate	$2\sim10*10^{5}$/pulse
$B\cdot S\cdot\overline{BV}$	EVG	# of event triggers	$2\sim5*10^{-5}$
B•pulser	EVG	# of beam triggers	∿25% of event trigg
Spills		# of spills	
B	SPG	# of beam muons in the spill	
$B\cdot S\cdot\overline{BV}$	SPG	# of event triggers(SPG)	
PC strobe	EVG	Prop. Chamber strobe	∿10% of beam
$B\cdot\overline{BV}_d$	EVG	# of effective muons	80∿95% of B
$B\cdot S\cdot\overline{BV}_d$	SPG		
$B\cdot\overline{BV}$	EVG	Beam outside of BV	∿1% of B
B104	SPG	Beam through the aperture of the last bending magnets	1.5∿2 times B
B•S	EVG	Accidental(mostly) coincidence of B and S	0.01∿0.03% of B
S	EVG	# of halo tracks into the spectrometer	0.4∿1 of B
$B104\cdot B104_d$	SPG	Spill monitor	0.5∿3% of B104

note; d means delay of 60 ns (3 RF buckets)

Table 3.6b Ratio of Scalers

B/SEM	Muon yield/proton	$10^{-7} \sim 10^{-8}$
B/SPILL	Intensity	200∿1000 k
$B \cdot S \cdot \overline{BV}/B \cdot \overline{BV}_d$	Trigger rate	$2 \sim 5 \cdot 10^{-5}$
$B104 \cdot B104_d/B104$	Probability of finding a muon in an RF backet	0.5∿3%
$B \cdot \overline{BV}/B$	BV performance and beam steering	10^{-3}
S/B	Halo rate and check of B or S	0.4∿1
B_{EVG}/B_{SPG}	Dead time of the system	85∿95%
B·S/B	Also spill monitor	1∿6%

I. On-Line Computer

All the information, such as the scalers, time digitizer counts, and proportional chamber bits, were registered in the CAMAC modules when a trigger occurred. This information was read into a PDP11/20 16 k-core computer via a branch driver BD011. The PDP11 software was supervised by a specially written disk operating system, which allowed maximum use of the limited core size.

The most important task of the system was to write the information onto magnetic tape for later off-line analysis.

Four events were stored in the core and transfered to tape as one record. A maximum of 100 events could be buffered into the disk, but the data taking rate was limited to about 30 triggers per spill by the recharging time of the spark chamber power supply.

The word structure of the event block written on tape is given in Table 3.7.

Besides writing tape, various on-line programs were developed to monitor the operation of detectors. The disk operating system allowed scheduling these programs upon request without interrupting the data taking.

Table 3.7 Primary Tape Format

1 block	4 events
1 event	704 words
1 word	16 bit integer

words	contents
1 - 15	ID words (2=run#, 3=event#)
16 - 47	16 24 bit scalers (2 words/scaler)
48 - 49	2 DCR(Discriminator Coincidence Register)
50 - 53	4 TDC(Time to Digital Converter)
54 - 65	10 ADC(Analog to Digital Converter) (pulse heights of target counters)
66 - 395	10 time digitizers (8 sparks x 4 coordinates x 10 modules)
396 - 509	Proportional chamber bits
510 - 653	Proportional chamber bits
654 - 671	8 ADC(pulse heights of target counters)
652 - 704	blank

IV. DATA COLLECTION AND ANALYSIS

A. Data Taking

The detectors constructed at various places were assembled at Fermilab and the apparatus was ready by the summer of 1972.

By that time the main ring reached 10^{12} protons/pulse, started extracting beam successfully, and the muon beam line was about to be energized. We participated in developing the muon beam, while testing the apparatus with cosmic rays and developing the analysis program.

Significant data were collected in three separate periods: in August and October,1973 and in April of 1974.

A summary of run condition is given in Table 4.1.

Each period consisted of about 2 to 3 weeks of calendar time.

Besides the inelastic muon scattering data, we collected calibration data by sending beam muons of various energies into the spectrometer, as discussed in Appendix C.

Table 4.1 Summary of Data Taken

Date	E_0 (GeV)	Target* position	Angular range	#incident muons (10^9)	#triggers (10^3)
Aug.'73	150	SA	15-58	0.6	1
	150	LA	24-88	1.9	25
Aug.'73	56.3	LA	39-144	0.1	25#
Oct.'73	150	VSA	13-50	0.8	30
		SA	15-58	1.1	50
		MA	19-70	0.8	25
		LA	24-88	1.0	23
	75	LA		0.3	20
Apr.'74	56.3	LA	39-144	3.7	80
		SA	24-95	2.8	129
	150	$LT\mu^+$		3.4	57
		$LT\mu^-$		2.9	42

* Target position

SA	small angle
VSA	very samll angle
MA	moderate angle
LA	large angle
LT	long target

no beam veto in the trigger

B. Secondary Analysis

The secondary analysis consisted of decoding the primary tapes written by the PDP11 on-line computer, reconstructing beam tracks in the beam chambers, reconstructing and fitting the tracks in the spectrometer and writing them onto secondary tapes.

The Cornell production analysis which is discussed primarily in this paper was done on the PDP10 at Cornell and later on the CDC7600 at Berkeley through a telephone link.

Two other analyses developed are compared in Table 4.2.

A preliminary first pass analysis of almost half of the data was done on the PDP10 and CDC6600 at Fermilab.

The first pass analysis was very instructive in uncovering various subtleties in analysis, as listed below.

1) In the original approach, tracks were sought by looking a ϕ window which was opened for each point found, where ϕ is the azimuthal angle at each chamber.

This window was inevitably larger at larger radius, and was confused by noise points, which occured about 10% of the time due to the electromagnetic showers from the iron associated with the muon tracks. This resulted in a long χ^2 tail which produced a cut dependent bias.

2) Beam track reconstruction efficiency for some of the data was rather low and appeared to be biased.

Table 4.2. Two Other Analyses

MSU analysis

1. Independent track hunting in the spectrometer.

   Tracks were sought in each projected plane, and two views were combined to reconstruct tracks in space. The best track that was consistent coming from the target was selected out of many duplicates.

2. The same momentum fitting program was used.

3. BACKFIT was used as the final analysis.

4. An independent Monte Carlo program was developed and compared to the data.

Berkeley analysis

1. Track hunting uses the same technique as Cornell's. Improvements were made in reducing the window sizes etc.

2. Independent momentum fitting program was developed.

3. TIEFIT was used as the final analysis, where fit was made by constraining the found tracks to the target center.

4. An independent Monte Carlo program was developed to compare to data.

3) Originally a track found in the spectrometer was linked to the target without paying much attention to the consistency between the found line in front and the track.

The front chambers which were between the target and the first iron magnets were essentially unshielded from the showers originating either from produced hadrons or from electromagnetic processes. If, for instance, front points were sought for a halo track in the spectrometer, it was often easy to find a line linking them to the target and these false trajectories were fitted with a lower energy and with a reasonable .

The analysis program was subsequently improved by replacing the track finding part in the spectrometer entirely, improving and refining the beam finding algorithm and taking great care in linking spectrometer tracks to the target.

Figure 4.1 shows the flow of analysis.

After decoding the PDP11 words of the primary tape, the beam tracks were sought in the beam chambers.

Then scattered muon tracks were reconstructed in the last five spark chamber modules. As mentioned, these modules were well protected from the showers originating in the target.

The found points were fitted to obtain the momentum and angle. This fit is called BACKFIT.

Figure 4.1 The Flow Diagram of Secondary Analysis

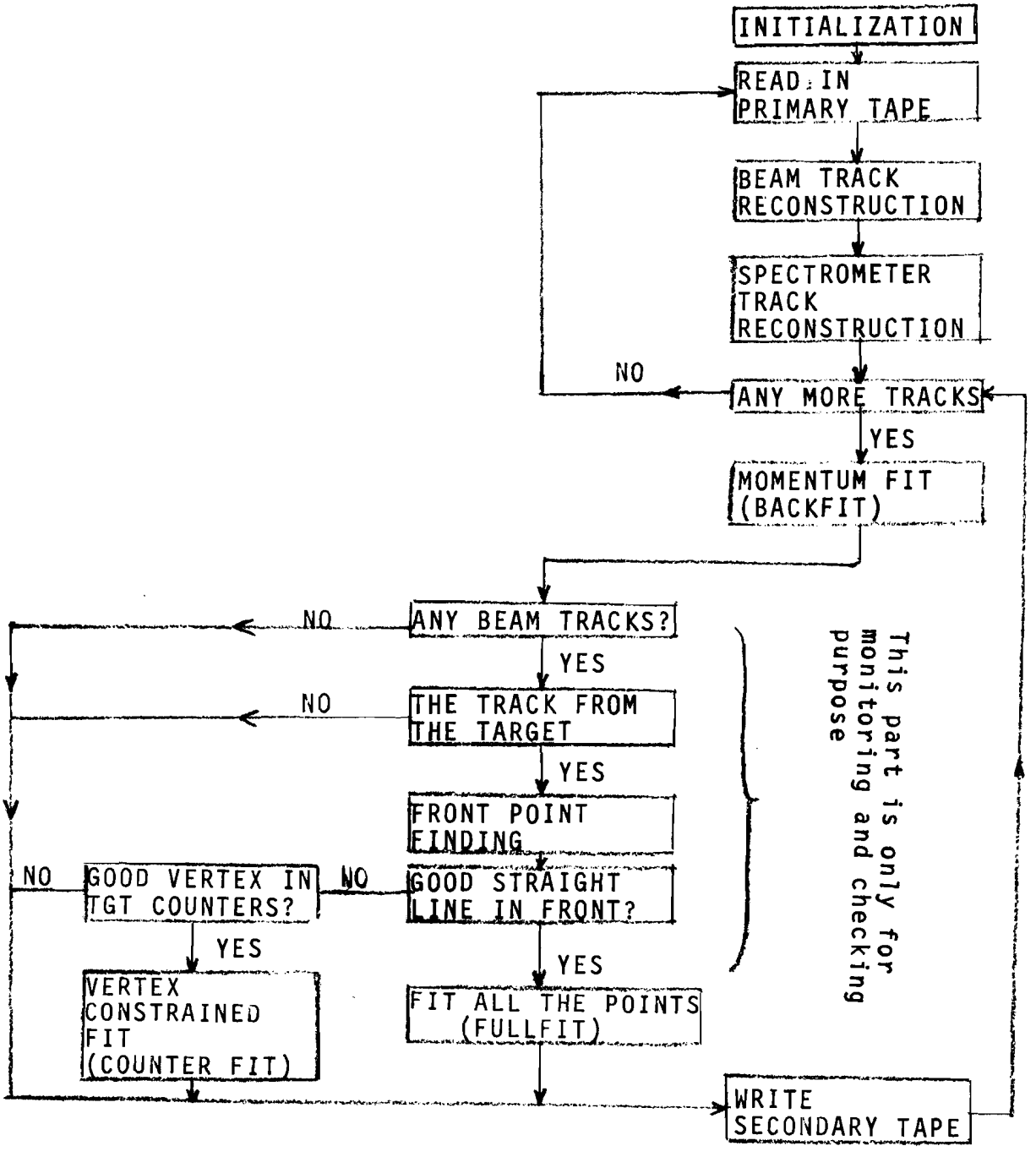

Using the BACKFIT information, the analysis program proceeded to finding the points in the front chambers and fitting entire points (FULLFIT), or if this failed, to finding the vertex in the target counters and fitting by constraining the vertex.(COUNTER FIT).

The properties of FULLFIT and COUNTER FIT were studied in detail using the BACKFIT as a monitor. FULLFIT was on average about 75% efficient, with an E' dependent bias, and COUNTER FIT was not reliable.

We decided to use BACKFIT for the final analysis, and the other fits were used for various checks.

Every BACKFIT track found was written on to secondary tape independent of beam track finding. The information written is summarized in Table 4.3.

Although BACKFIT did not have the problem of the hadron showers, it had the following undesirable features:

i) E' resolution was poorer than for the other two. It was about 15% for 150 GeV data and 17% for 56.3 GeV data.

ii) BACKFIT has larger sensitivity to misalignment of detectors.

iii) The reconstructed angle and the momentum are coupled.

These are studied in detail in obtaining the results.

Table 4.3 Secondary Tape Format

90 words / event
10 events/record
1 word = 32 bit integer
800 BPI 9 track IBM compatible

words	
1 - 5	1=run#*10^5+event#, # of beam tracks etc.
6 - 20	measured x(modules#1 - 15)
21 - 35	measured y(modules#1 - 15)
36 - 40	(P_x,P_y,P_z) and (x,y) at z = 0; incident
41 - 45	(P_x,P_y,P_z) and (x,y) at z = 0; scattered
46 - 47	χ^2*10^2 and dof*10^2 of the fit
48 - 58	fitted x(modules#5 - 15)
59 - 69	fitted y(modules#5 - 15)
70 - 73	(x,y) at module#10 and (x',y') of BACKFIT
74 - 75	E' and χ^2/dof of BACKFIT
76 - 87	data ;# of sparks and contribution to the track, ADC and DCR coded
	Monte Carlo;Z_{int},E_o,$Q^2/2ME_0$,ν/E_0,weight*10^3 and E' true values
88 - 90	scalers;$(B\cdot\overline{BV}_d)$, B104, SPILL MONITOR

note; 1. units are in MeV, MeV/c, 0.1 mm and 0.01 mrad.
2. beam trigger information was written on the same tape as follows

Beam Trigger

1	-(run#*10^5+event#)
2 - 5	(x,y) and (x',y') of the beam at z=0
6 - 14	measured x(modules #2 - 10)
15 - 24	measured y(modules #1 - 10)
25 - 30	DCR, # of beam tracks, ADC etc.

C. Tertiary Analysis

Event selection was done by reading in the secondary tape and applying cuts. Events passing through the cuts were histogramed and also written onto a tertiary tape to compare various sets of data.

The standard cuts are summarized in Table 4.4.

Geometrical cuts were applied to the reconstructed points in the last five modules, in order to ensure that the scattered muons were well within the apparatus. All five modules are required to contribute to the tracks.

About 60% of the reconstructed tracks passed this cut.

The number of beam tracks per trigger was required to be one and only one, because BACKFIT had a poor resolution in distinguishing the correct beam track.

The minimum scattered energy was set at $E_0/3$. At lower energy, the track reconstruction started breaking down and the momentum fit gave a large shift according to a Monte Carlo study.

Also from the physics point of view, effects such as radiative corrections and wide angle bremsstrahlung background become large and less certain.

χ^2/dof of the BACKFIT did not have a long tail in the improved analysis. Less than 2% of events were χ^2/dof between 5 and 10. (dof is the degrees of freedom).

Table 4.4. Summary of Cuts

Geometry	$\|x_m\|>8''$ or $\|y_m\|>8''$	$m = 11 - 13$
	$6.5''<r_m< 33''$	$m = 11 - 13$
	$6.5''<r_m< 33''$	$m = 14 - 15$
Beam	$r_B<9$ cm, $dr_B/dz<2$ mrad. at the center of the target. one and only one beam track. per trigger	
E'	$E'(\text{BACKFIT}) > E_0/3$	
χ^2/dof	$\chi^2(\text{BACKFIT})/\text{dof} < 10$	
Z_{int}	$-180''<Z_{int} - Z_{tgt}< 80''$ for 150 GeV data and scaled values for 56.3GeV	

The Z_{int} cut was very effective in separating out events from halo tracks.

The Z_{int} for the BACKFIT was calculated by minimizing the angle necessary for the scattered muon track to coincide with the beam track. Figure 4.2 shows a typical distribution after the standard cuts except for the Z_{int} cut. The Z_{int} for halo tracks were well separated, peaked at the last bend point of the muon beam line.

About 60 to 70% of the tracks passing all the other cuts were halo tracks cut out by this.

Figure 4.3 shows the stability of the event rate.

Run 463 for 150 GeV LA data is several standard deviations away from the average, but an investigation revealed nothing peculiar.

The event rates for 150 and 56.3 GeV data were different mainly because of different beam shape.

Condensed tape was written to combine and compare various data sets. The information written is given in Table 4.5.

Figure 4.2
Z_{int} Distribution (150 GeV)

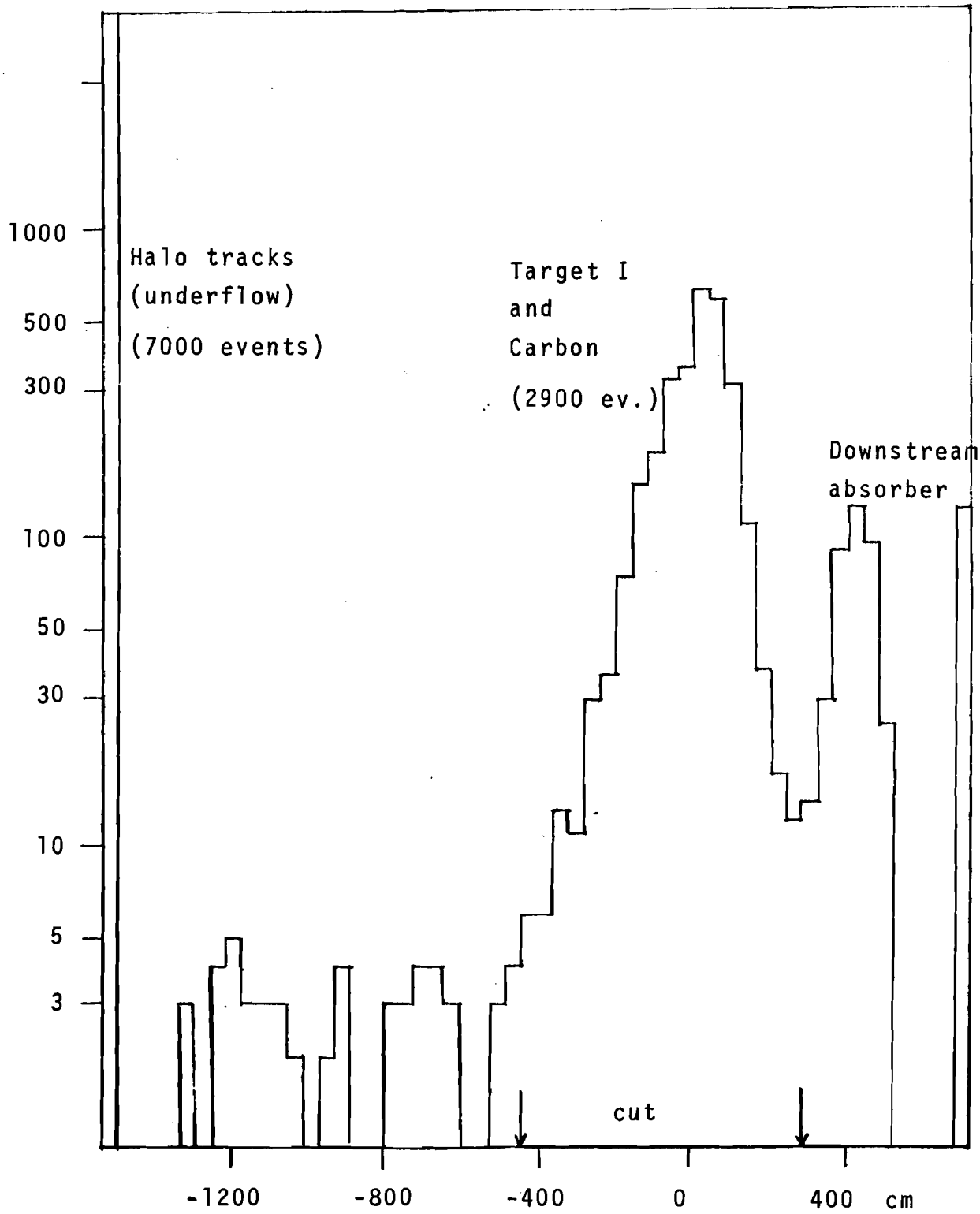

Figure 4.3a The stability of event rate (150 GeV)

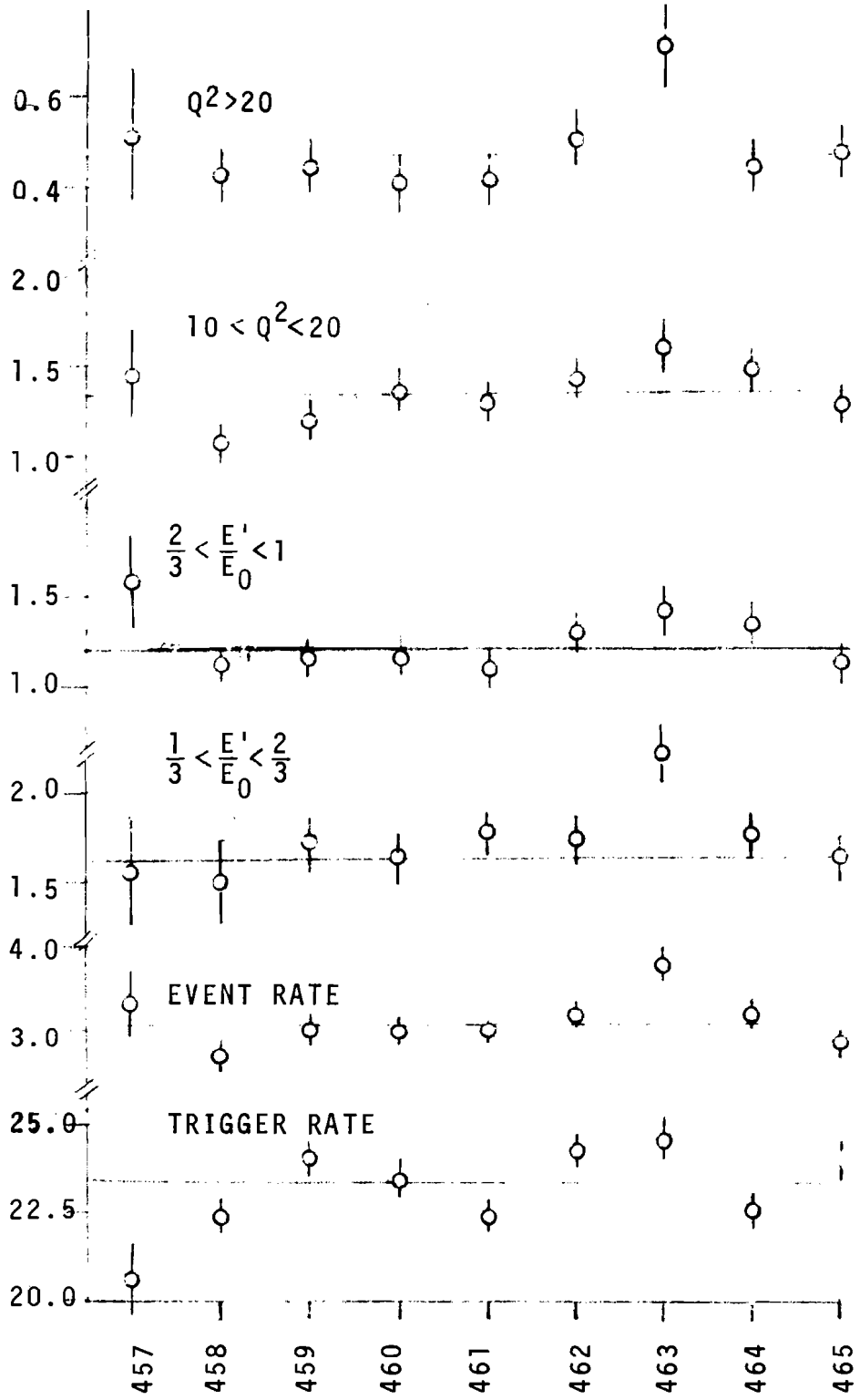

Figure 4.3b The Stability of Event Rate (56.3GeV)

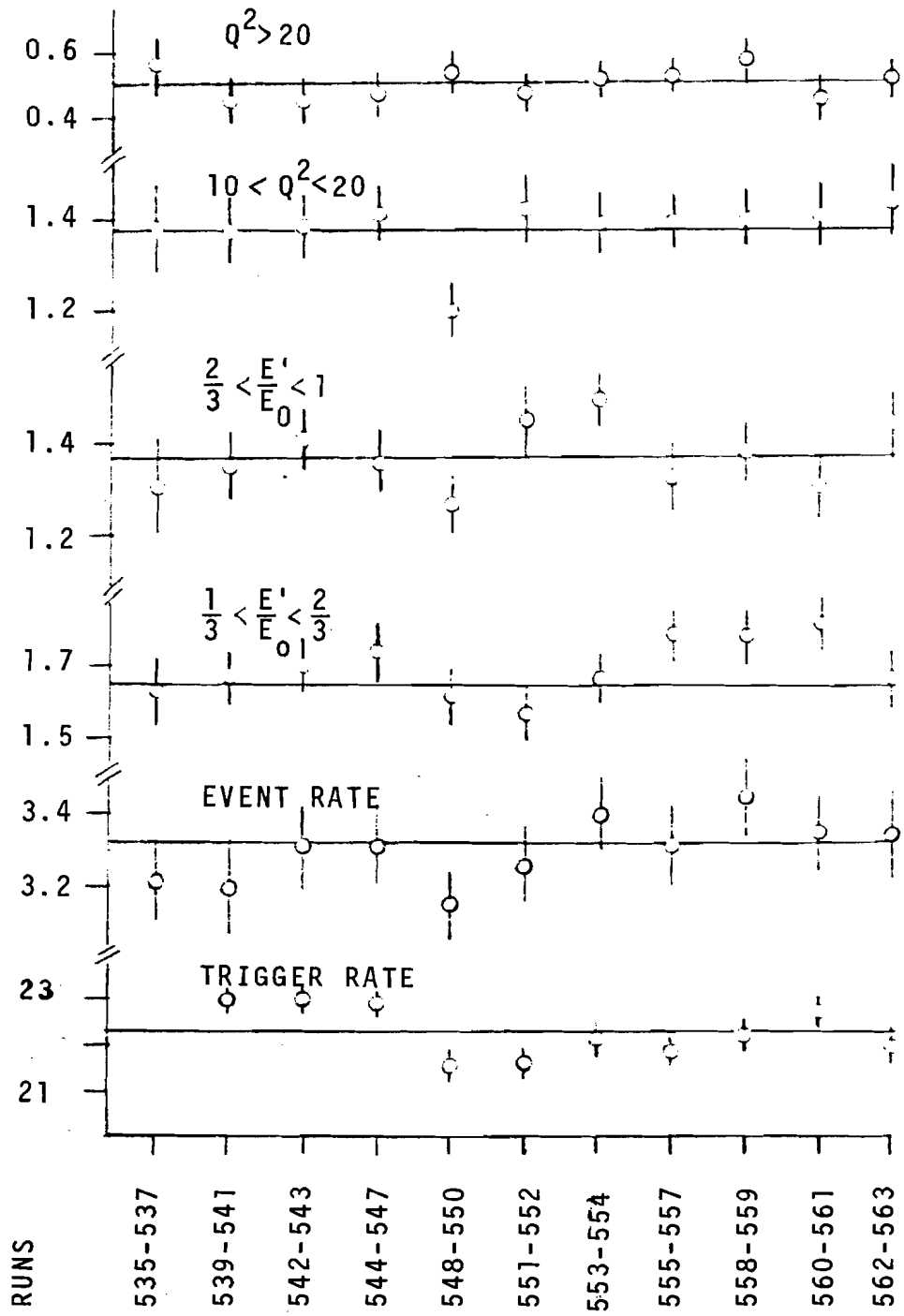

Table 4.5. Tertiary Tape Format

15 words/event
60 events/record
1 word = 32 bit integer
800 BPI 9 Track IBM compatiable

words	
1	run# * 10^5 + event#.
2	E'
3	$E' * \theta$.
4	$\phi = \text{atan2}\ (P_X, P_Y) * 1800/\pi$.
5	E'_{true}
6	$(E' * \theta)_{true}$ } if Monte Carlo
7	$E_{0\ true}$
8	Z_{int} (in absolute coord)
9	X_B
10	X'_B
11	Y_B at $Z = Z_{TGT}$
12	Y'_B
13	$x_{11} \cdot 2^{15} + y_{11}$
14	$x_{13} \cdot 2^{15} + y_{13}$
15	$x_{15} \cdot 2^{15} + y_{15}$

Note :
1. Units are MeV, MeV/c, 0.01 m rad. and 0.1 mm
   x_{11} etc are measured ones.
2. E', θ and Z_{int} are from BACKFIT.
3. Words #13-15 need a special care for negatives.
4. Words #5-7 for data are, DCR, #tracks, etc.

D. Monte Carlo simulation

Simulated data by a Monte Carlo program were used to correct apparent nonscaling effects in comparing 150 GeV and 56.3 GeV data.

These effects are:

i) Different beam shape for the two energies.

ii) Different E' resolution of BACKFIT.

iii) Small nonscaling effect due to the radiative corrections.

The Monte Carlo program was also useful to estimate various effects in studying systematic errors.

The beam tracks used for the simulation were accumulated during the data taking by the beam trigger.

Events generated according to an assumed cross section were propagated through the spectrometer, and the generated tracks were written onto secondary tape just like data.

The detail of the program is described in Appendix E.

V. RESULTS AND FITS

A. Histograms

Histograms of the data taken at incident energies of 150 and 56.3 GeV are shown in Figure 5.1. The kinemaic values of the 56.3 GeV data were scaled to those of the 150 GeV data.

We test Bjorken scaling between the two energies by comparing the corresponding histograms.

In the figures, the smooth curves are the simulated data from the Monte Carlo program, and the ratio of the two is also shown. It is worthwhile to observe a general feature of the data, although we do not draw physics conclusions from this: different systematic effects are important, which are not fully studied yet. The characteristics of the data to Monte Carlo comparisons are:

i) The normalization of the data is higher by about 7%. This appears to be due to more events in the high ω region.

ii) The high E' end of the 1/E' ratio has some structure. This structure could be almost taken out by shifting E' by 1%, which is within the systematic uncertainties of the data.Without an independent support for this, it is however not permitted to make such an arbitrary adjustment to fit the Monte Carlo results.

iii) The θ distribution has little structure, and is consistent with being flat.

iv) The slope of the P_T distribution is again sensitive to an E' shift.

v) The low ω region is sensitive to a small resolution difference and E' shift between Monte Carlo and data.

Figure 5.1 1/E' Distribution

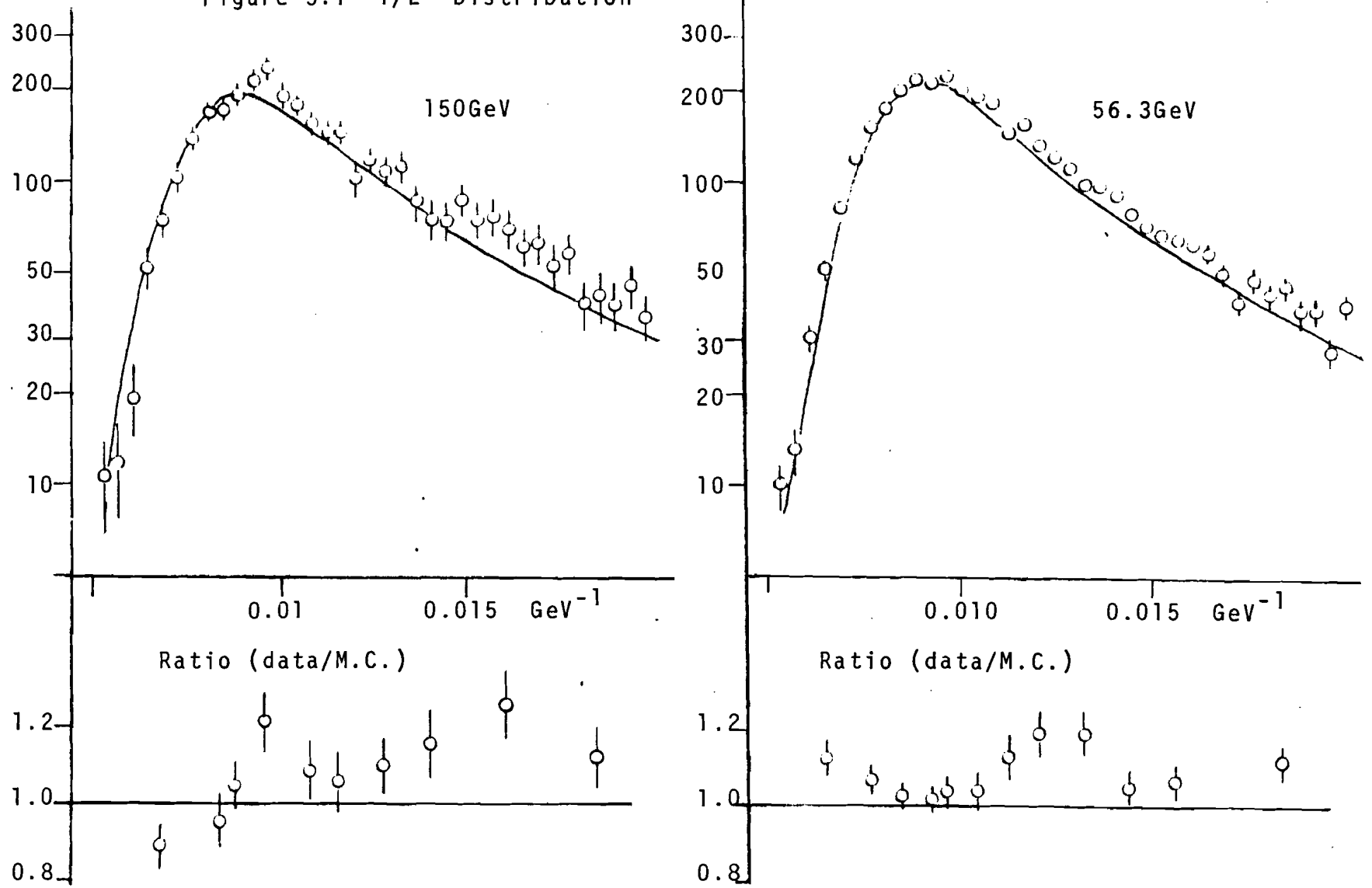

Figure 5.1 θ Distribution

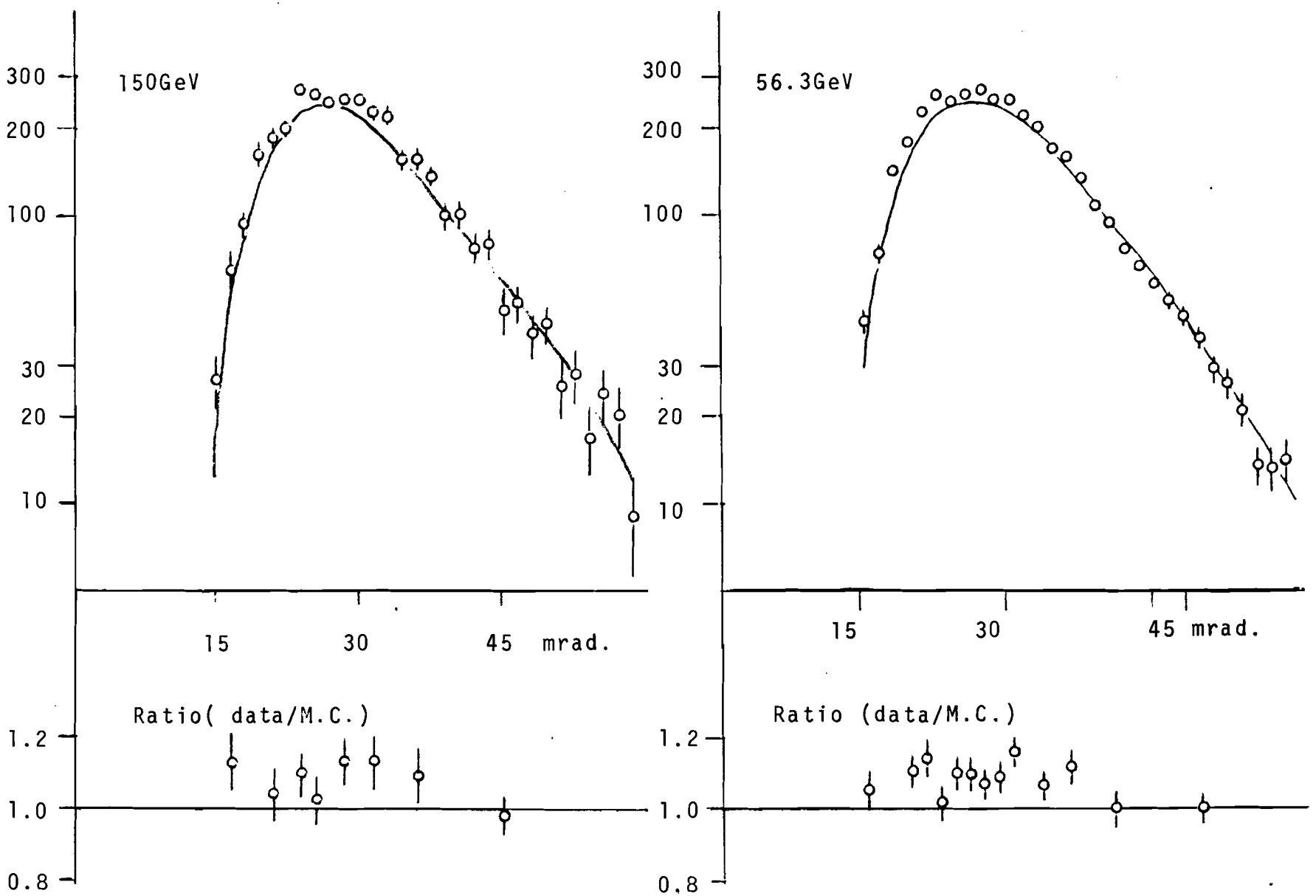

Figure 5.1 P_T Distribution

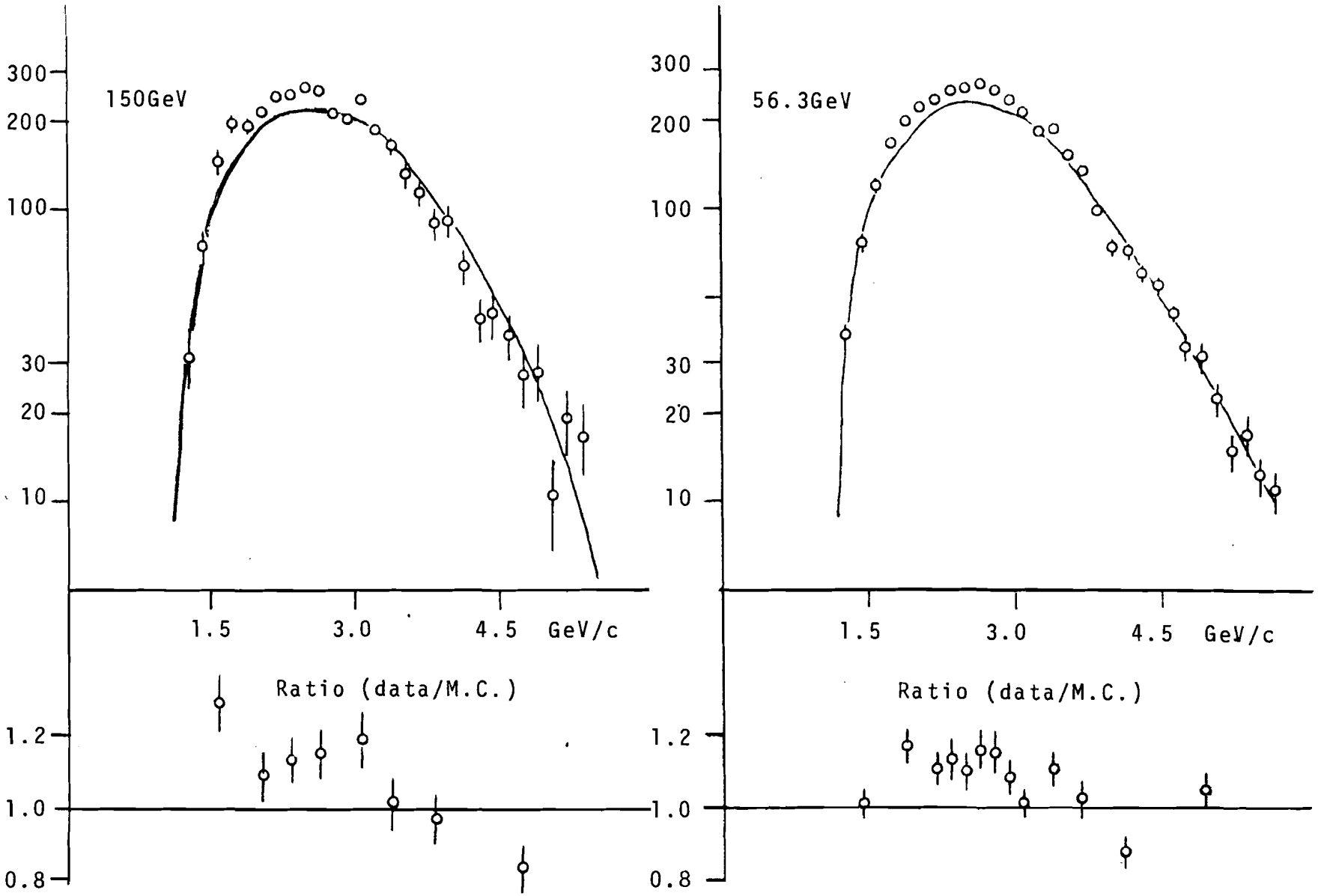

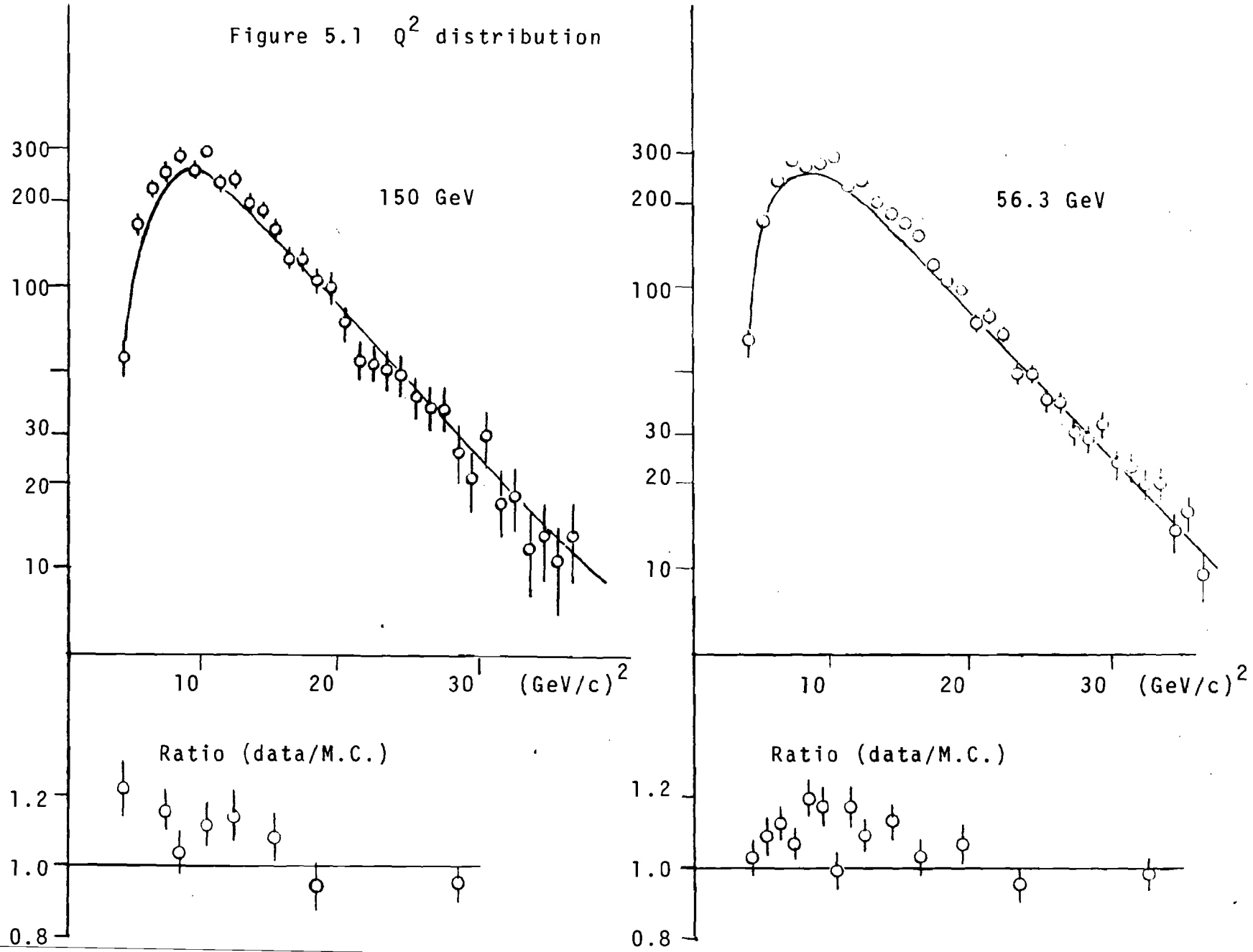

Figure 5.1 Q^2 distribution

Figure 5.1 ω Distribution

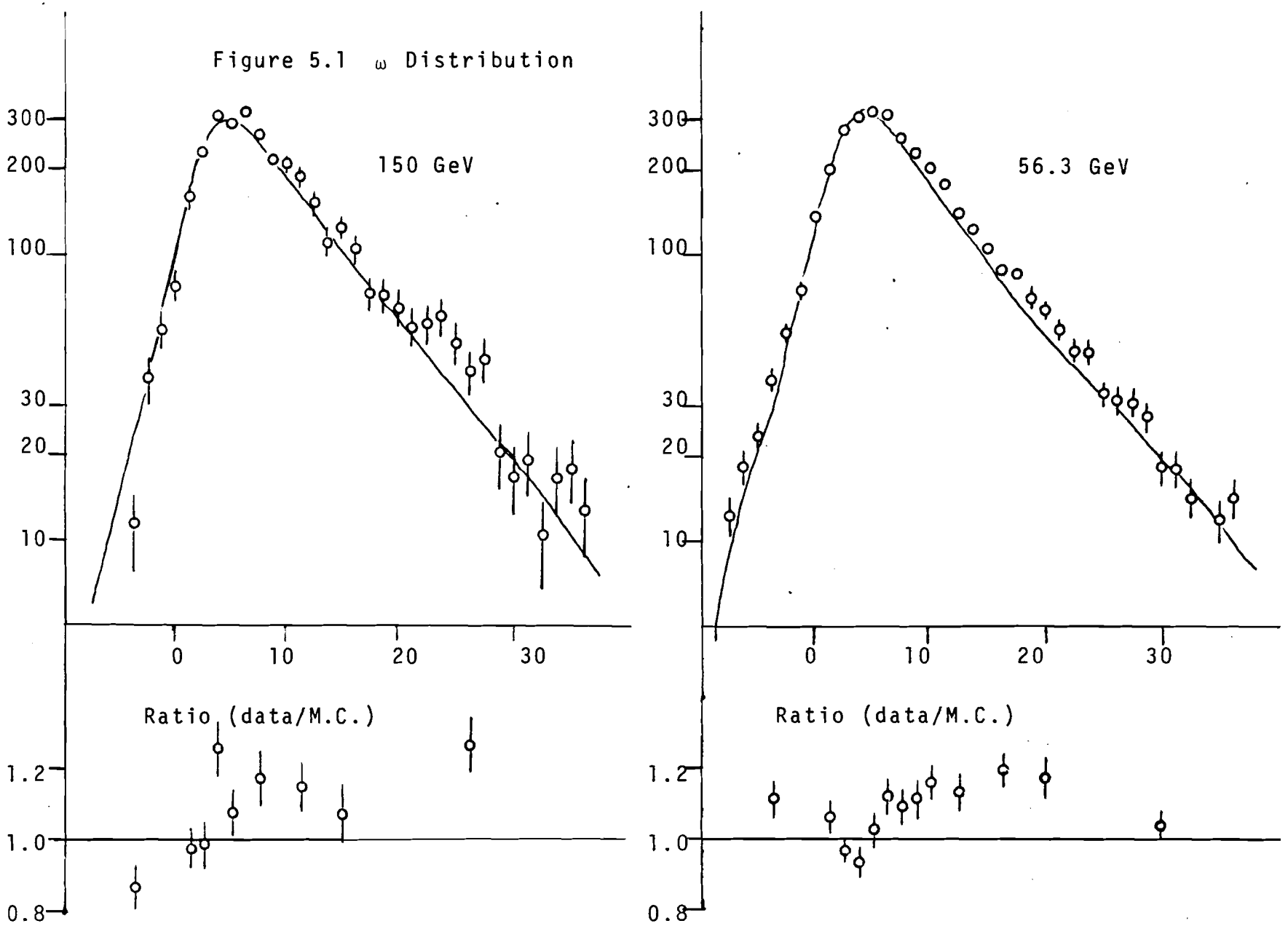

Figure 5.1 R_{13} Distribution

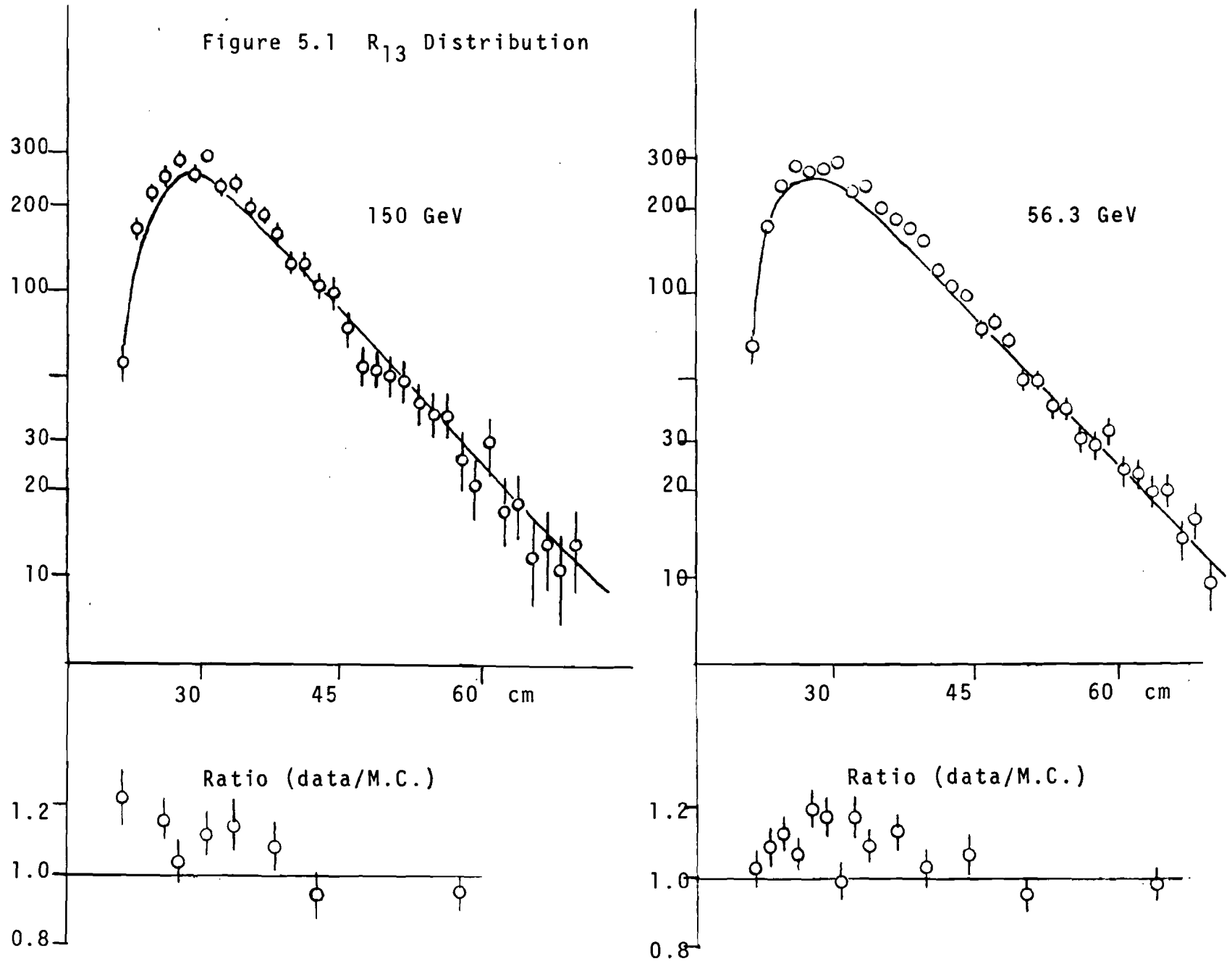

B. Ratio of 150 and 56.3 GeV Data

Taking the ratio of 150 and 56.3 GeV data, we test the validity of Bjorken scaling between the two energies.

The ratios shown in Figure 5.2 are obtained in the following way.

$$\text{Ratio} = \frac{(150\ \text{GeV data}/56.3\ \text{GeV data})}{(150\ \text{GeV Monte Carlo}/56.3\ \text{GeV Monte Carlo})} \tag{5.1}$$

The reason for dividing the ratio of data by that of Monte Carlo results is to take out the apparent nonscaling effects listed in Chapter IV.D.

The Ratios of Monte Carlo alone are shown in Figure 5.3. The dominant effect for the deviation from unity is that of different beam shape for the two energies, as shown in Figure 5.4. The 56.3 GeV beam was larger due to larger multiple scattering in the hadron absorber in the beam line. The beam size effect is seen to become negligible at large θ or in the large Q^2 region.

That the nonscaling of the two configurations is in fact small can be seen in Figure 5.5. This shows the ratio of Monte Carlo obtained by propagating the same generated events through the two configurations. The kinematic values were appropriately scaled, and the same beam sample was used.

In taking the ratio of (5.1), the different E' resolution

of the BACKFIT at the two energies was taken out by folding in an 8% gaussian error into 1/E' of the 150 GeV data and Monte Carlo. Neglecting the difference had little effect provided that the E' of "nonphysical events" (i.e. $\omega < 1$) was recomputed to that of $\omega = 1$, fixing θ. This eliminates the region sensitive to the resolution.

Figure 5.2 The Ratio of 150GeV/56.3GeV data

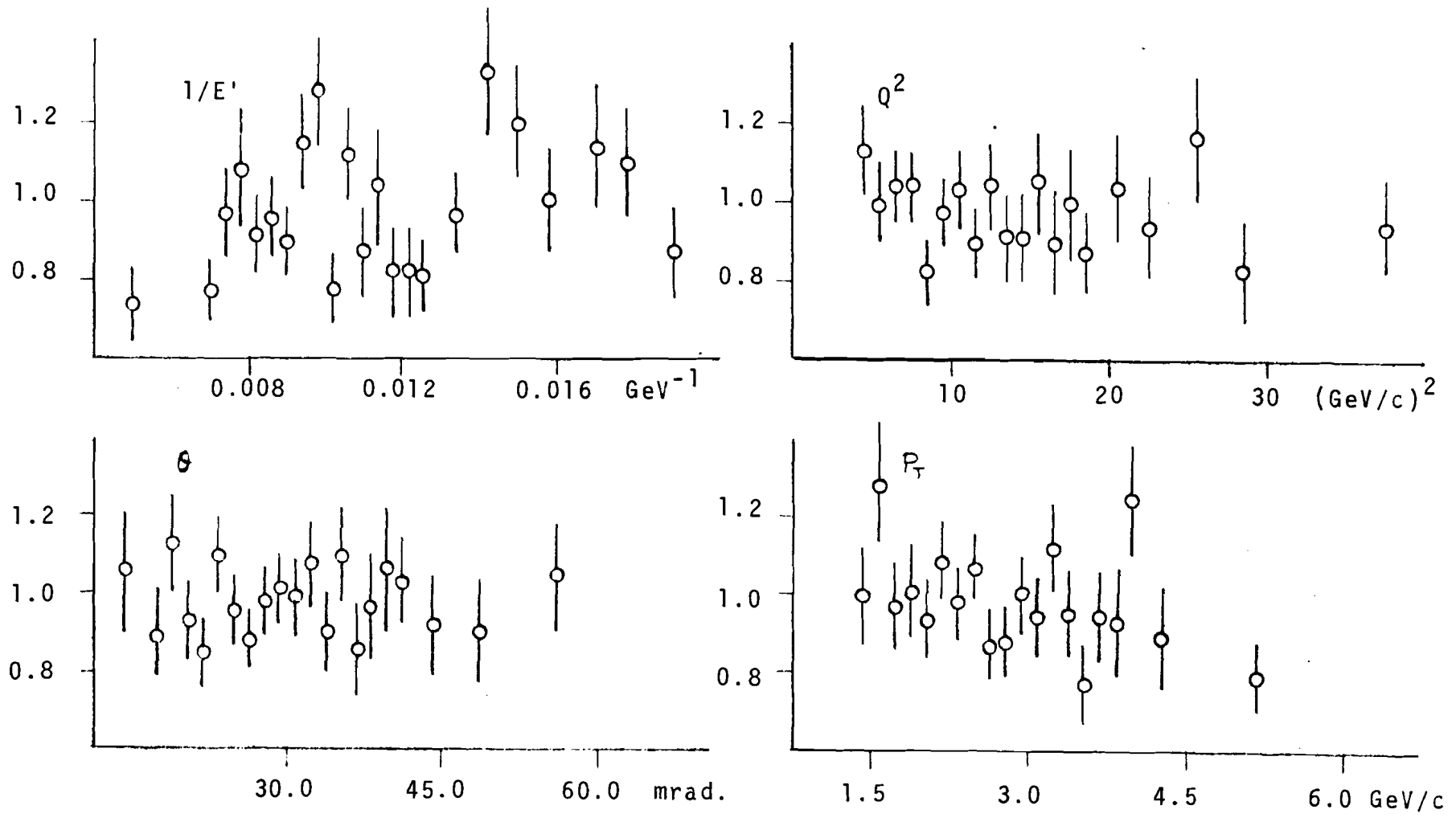

Figure 5.2 The Ratio of 150GeV/56.3GeV data

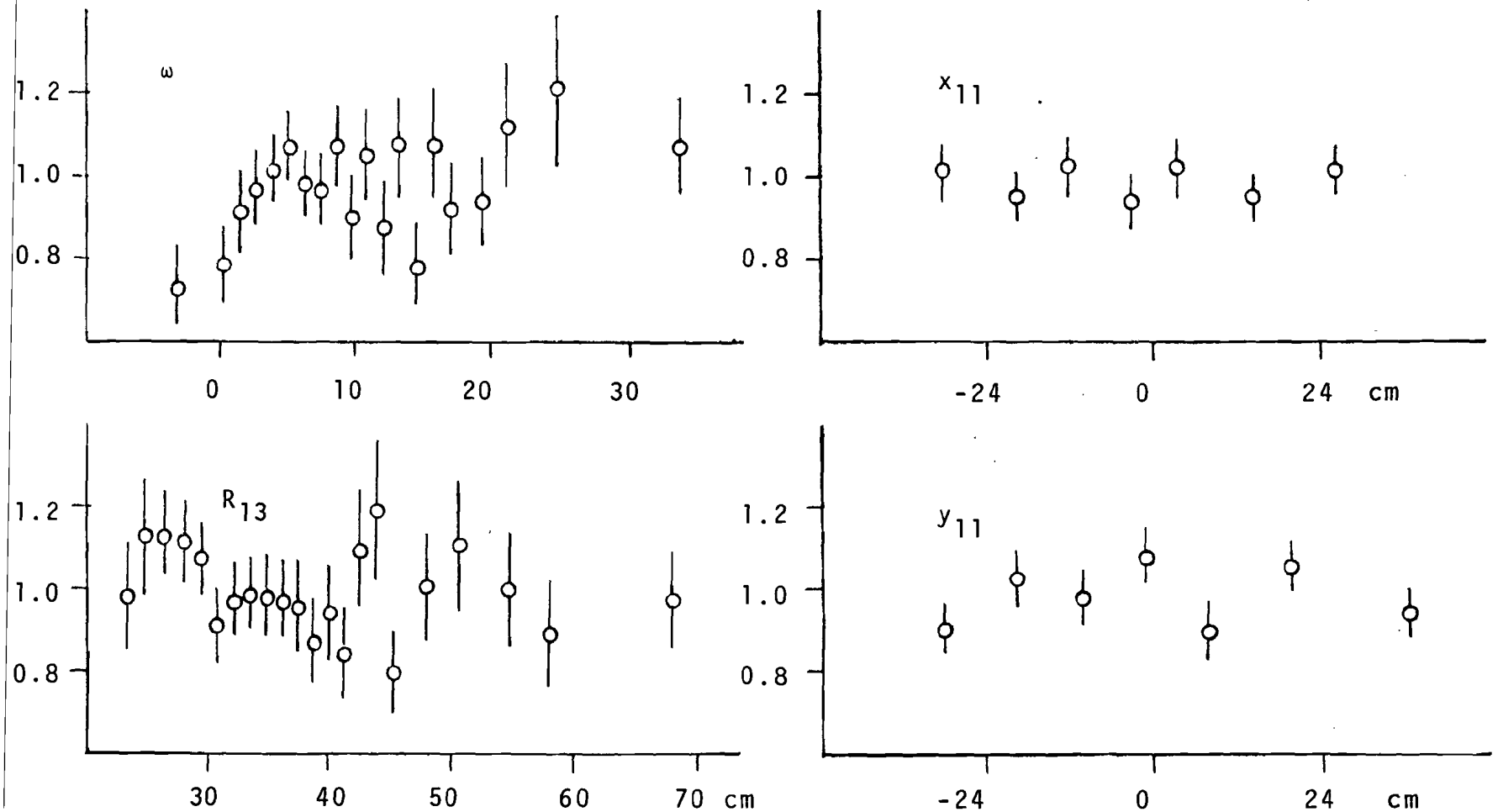

Figure 5.3 The effect of Beam Shape (150GeV/56.3GeV Monte Carlo)

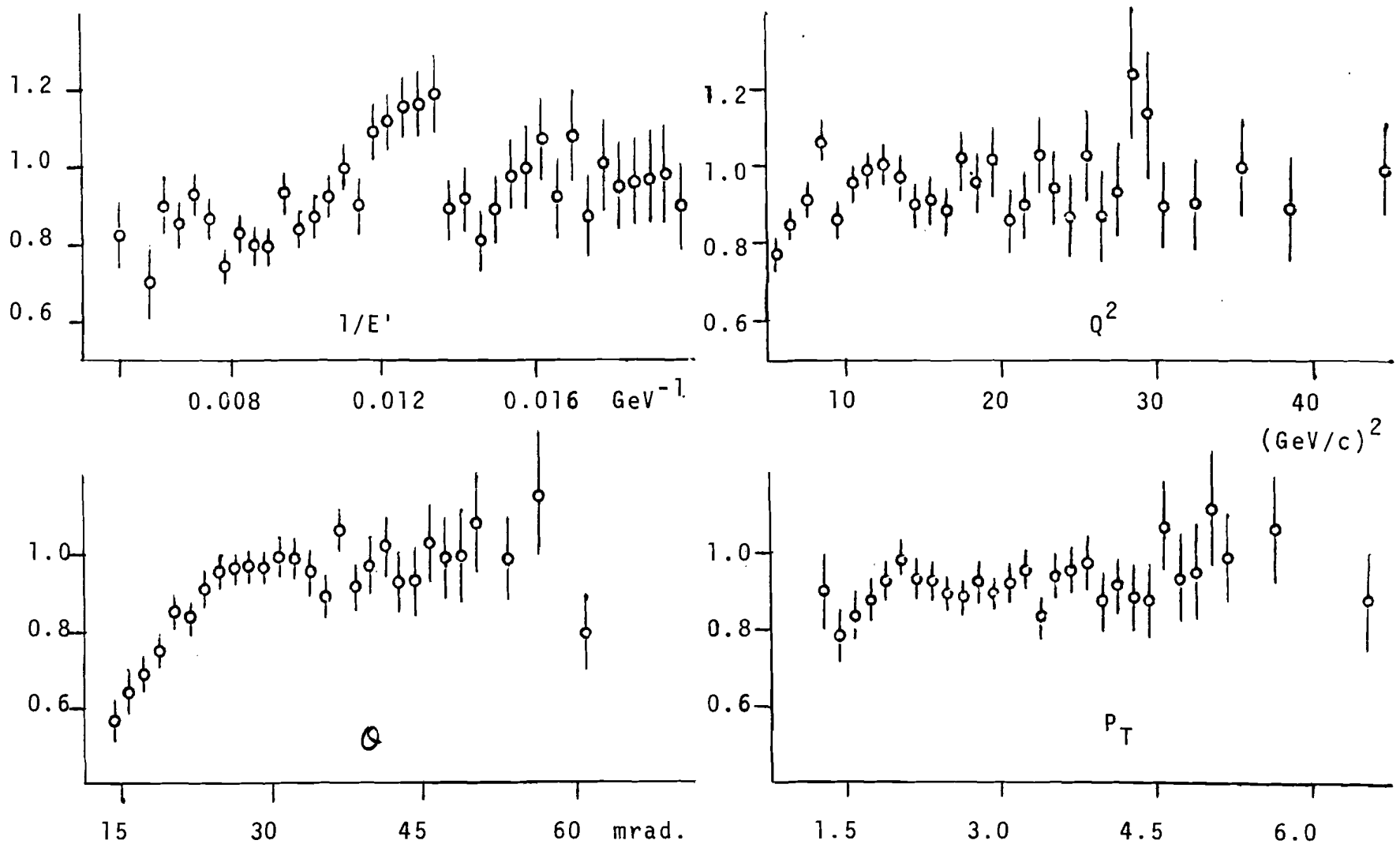

Figure 5.3 The Effect of Beam Shape (150GeV/56.3GeV Monte Carlo)

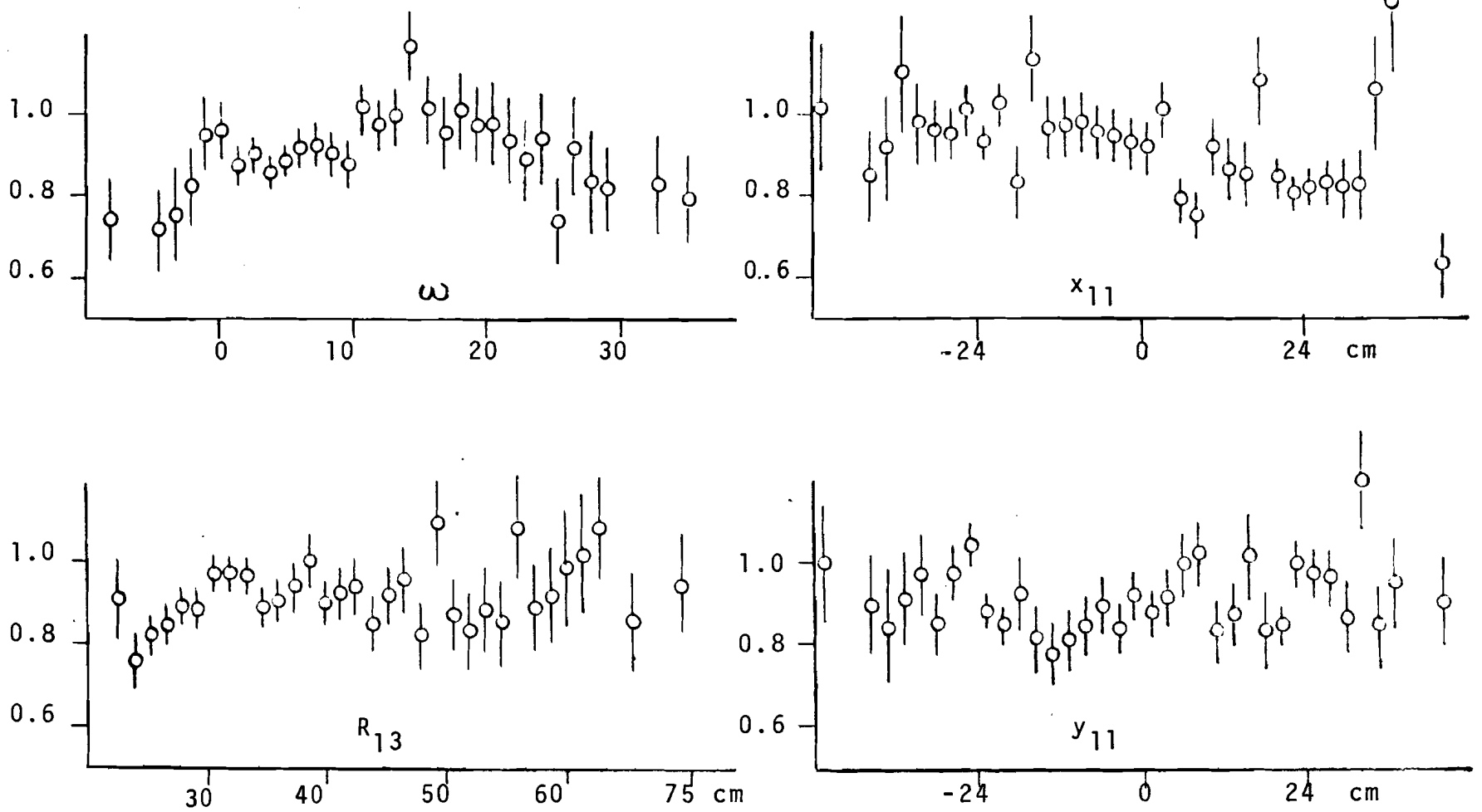

Figure 5.4

r_B^2 distribution of 150 and 56.3 GeV beam

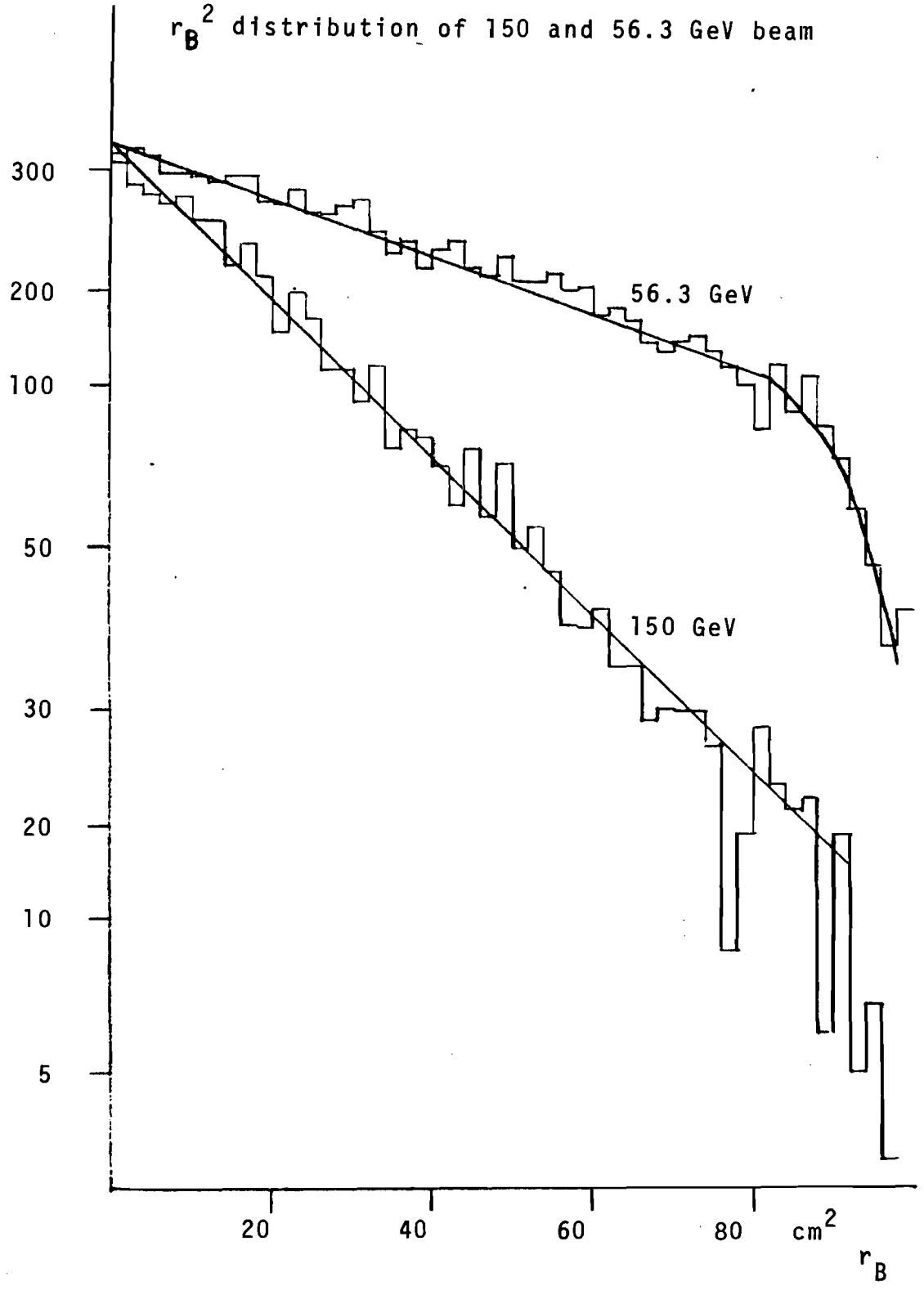

Figure 5.5 The Scaling of Apparatus (150GeV/56.3GeV Monte Carlo)

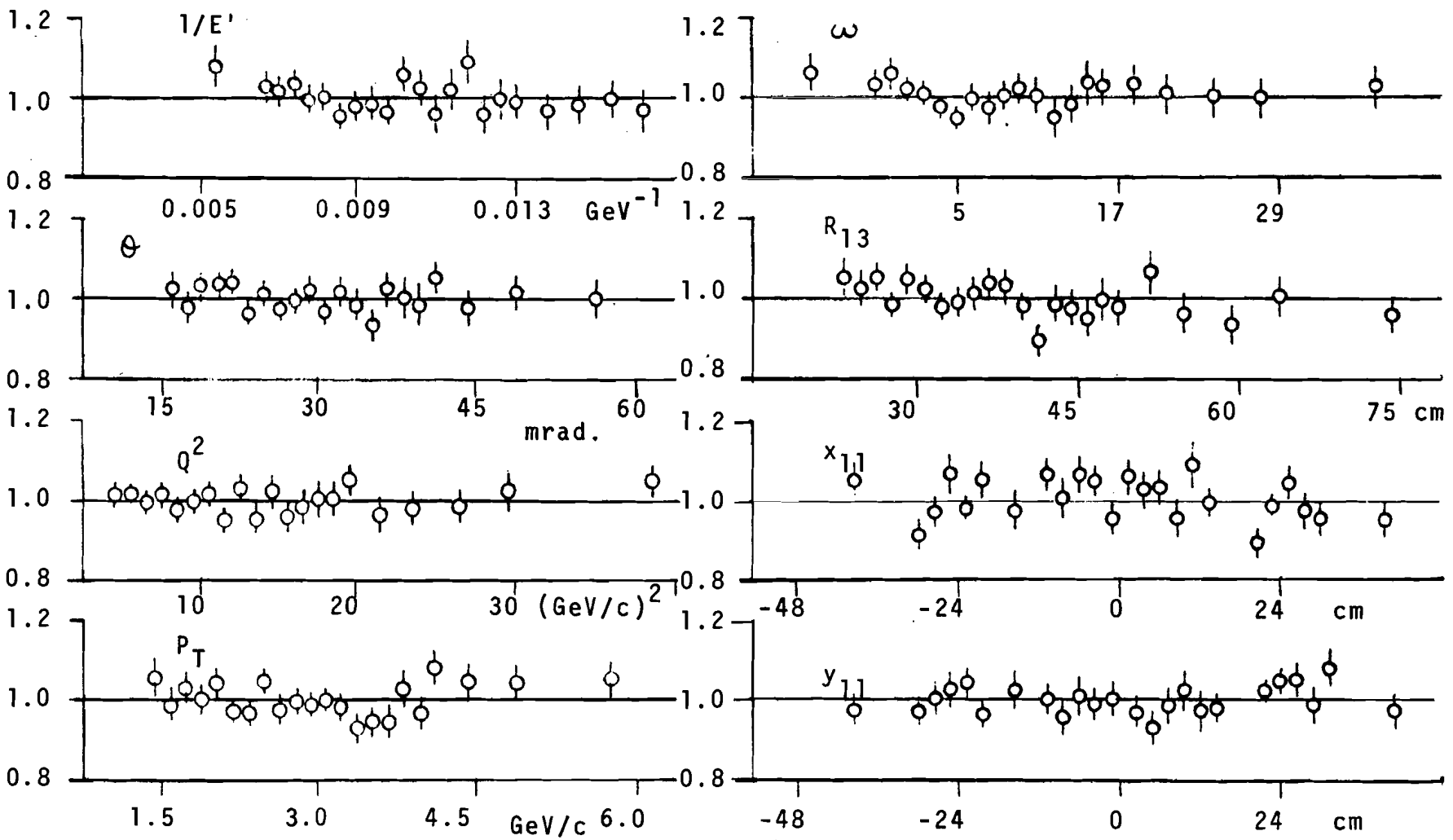

C. Propagator fit

According to Figure 5.2, the scaling is a good approxomation between the two energies.

To study scaling, the ideal way is to show the Q^2 dependence of the structure functions at fixed ω. It is difficult for us to do this because of the limited statistics and the poor E' resolution.

Instead, we parametrize a possible breakdown of scaling in the "propagator" form, to make a quantitative study.

$$\nu W_2(\omega,Q^2) = \nu W_2(\omega) \frac{N}{(1 + Q^2/\Lambda^2)^2} \qquad (5.2)$$

N is the normalization factor and Λ is the mass parameter relevant to scale breakdown. N = 1 and $1/\Lambda^2 = 0$ if the scaling is perfect. Note that this is only one particular form of possible breakdown, emphasizing the high Q^2 behavior of the structure functions is implied.

Other forms of breakdown are not considered here. This form is mainly used as a convenient parametrization. The physical interpretation of the parameter Λ is given in the next section.

Given this form, the ratio of scaled Q^2 distributions at the two energies is expressed as follows:

$$R_i = N \frac{(1 + \lambda Q_i^2/\Lambda^2)^2}{(1 + Q_i^2/\Lambda^2)^2} \qquad (5.3)$$

where N is the relative normalization, R_i is the ratio of the number of events in a bin of Q_i^2 and λ is the ratio of the incident energies for the two sets of data. Figure 5.2 is plotted in terms of measured values,but the Q_i^2 for the fit was obtained from Monte Carlo by accumulating the true value and by calculating the mean for each bin.

N and $1/\Lambda^2$ and the errors were obtained by minimizing the χ^2 defined as follows.

$$\chi^2 = \sum_i \left\{ \frac{R_i - N \dfrac{(1 + \lambda Q_i^2/\Lambda^2)^2}{(1 + Q_i^2/\Lambda^2)^2}}{\delta R_i} \right\}^2 + \left(\frac{N - 1.0}{\sigma_N}\right)^2 \tag{5.4}$$

R_i is the statistical error of the ratio R_i and σ_N is the assigned error in constraining the normalization.

Fits were made with $1/\Lambda^2 = 0$, free normalization ($\sigma_N = \infty$) and constrained normalization ($\sigma_N = 0.05$). N and $1/\Lambda^2$ are correlated as shown in Figure 5.6.

As the propagator fit only makes sense physically if N=1 at low Q^2, the result of this paper is based on the constrained fit. $\sigma_N = 0.05$ was chosen based on the study in Appendix F.

Table 5.1 shows the result of the fits.

Figure 5.7 shows the Q^2 behavior in several bins of ω to investigate a possible ω dependence. The ratios are consistent with being flat, but the normalization is smaller in

the low ω region. Q^2 and ω are in fact strongly correlated as shown in Figure 5.8. Projected on the Q^2 axis, the low Q^2 region gets equal contributions from the low and high ω regions. Binned in ω, there is not much Q^2 range to investigate in the high ω region. Also, the normalization in the low ω region is sensitive to the E' shift as shown in Figure F.1.

Table 5.1. Summary of Fits

Fits	N	$1/\Lambda^2 \cdot 10^4$	χ^2/dof	Confidence level
Constant ($1/\Lambda^2 = 0$)	0.96 ± 0.03	-	18.7/12	9.7%
Unconstrained ($N = \infty$)	1.03 ± 0.06	36^{+38}_{-32}	17.4/11	9.7%
Constrained ($N = 1 \pm 0.05$)	1.01 ± 0.04	27^{+26}_{-23}	17.5/11	9.3%

Table 5.2. ω Dependence

ω range	constant fit N	constant fit χ^2/dof	constrained fit $1/\Lambda^2 \cdot 10^4$
$\omega < 4$	0.87 ± 0.04	1.2	43.3 ± 35
$4 < \omega < 8$	1.02 ± 0.05	0.97	-0.5 ± 32
$8 < \omega < 16$	0.98 ± 0.05	0.10	12.3^{+49}_{-45}
$\omega > 16$	1.04 ± 0.06	1.04	-53.6^{-87}_{+78}

Figure 5.6 N - $1/\Lambda^2$ contour plot

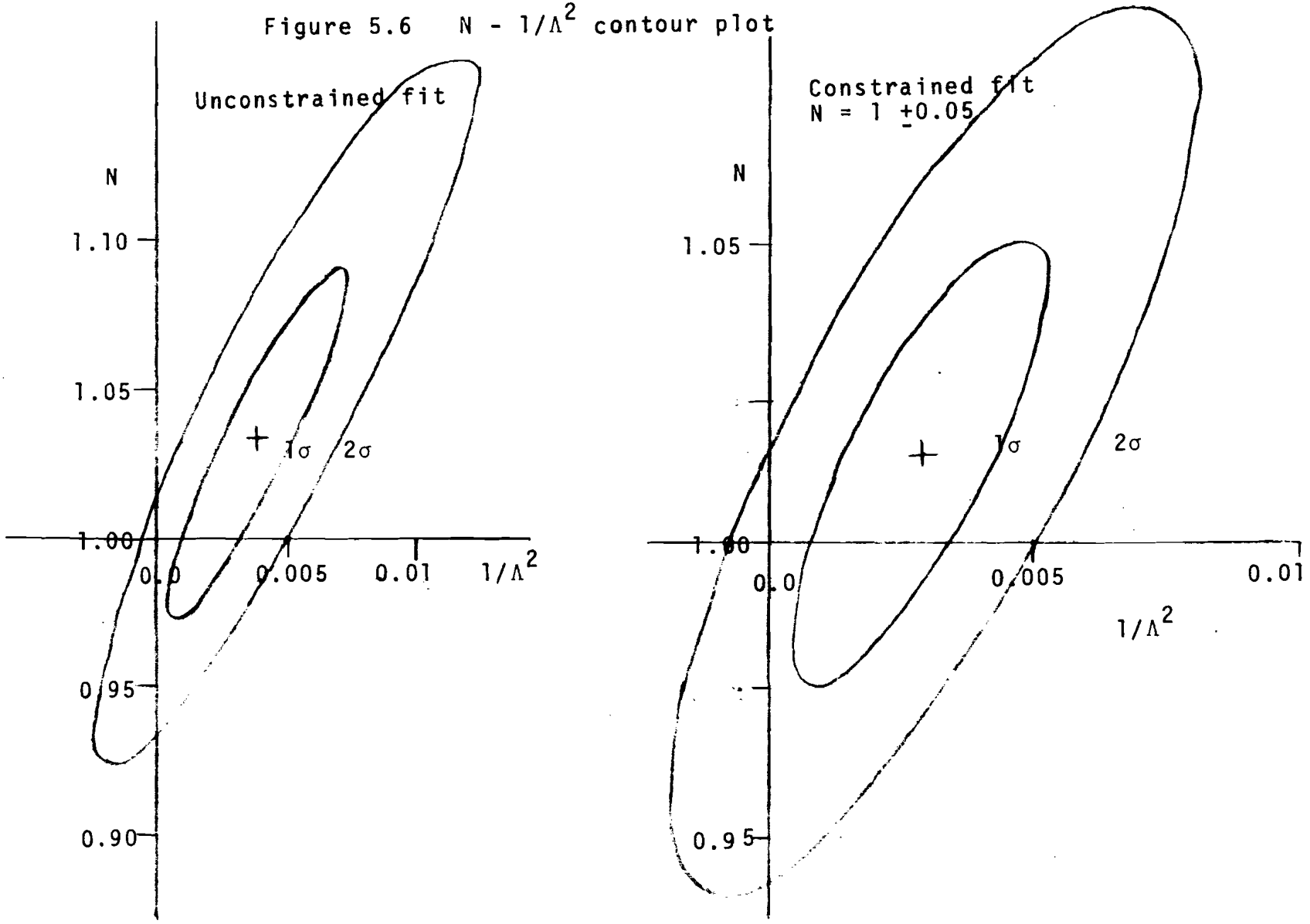

Figure 5.7 The ratio 150/56.3 GeV data vs. Q^2_{true}

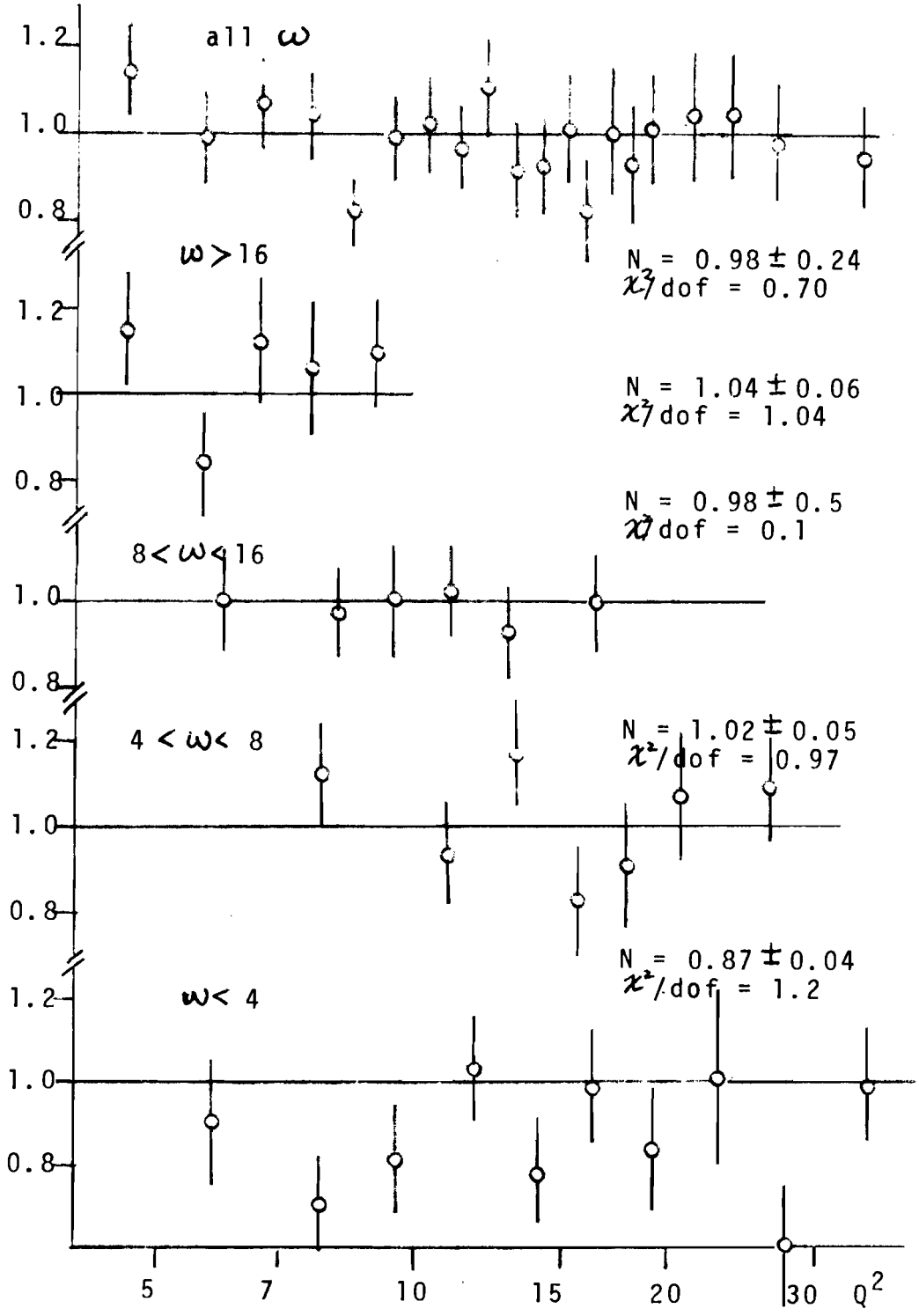

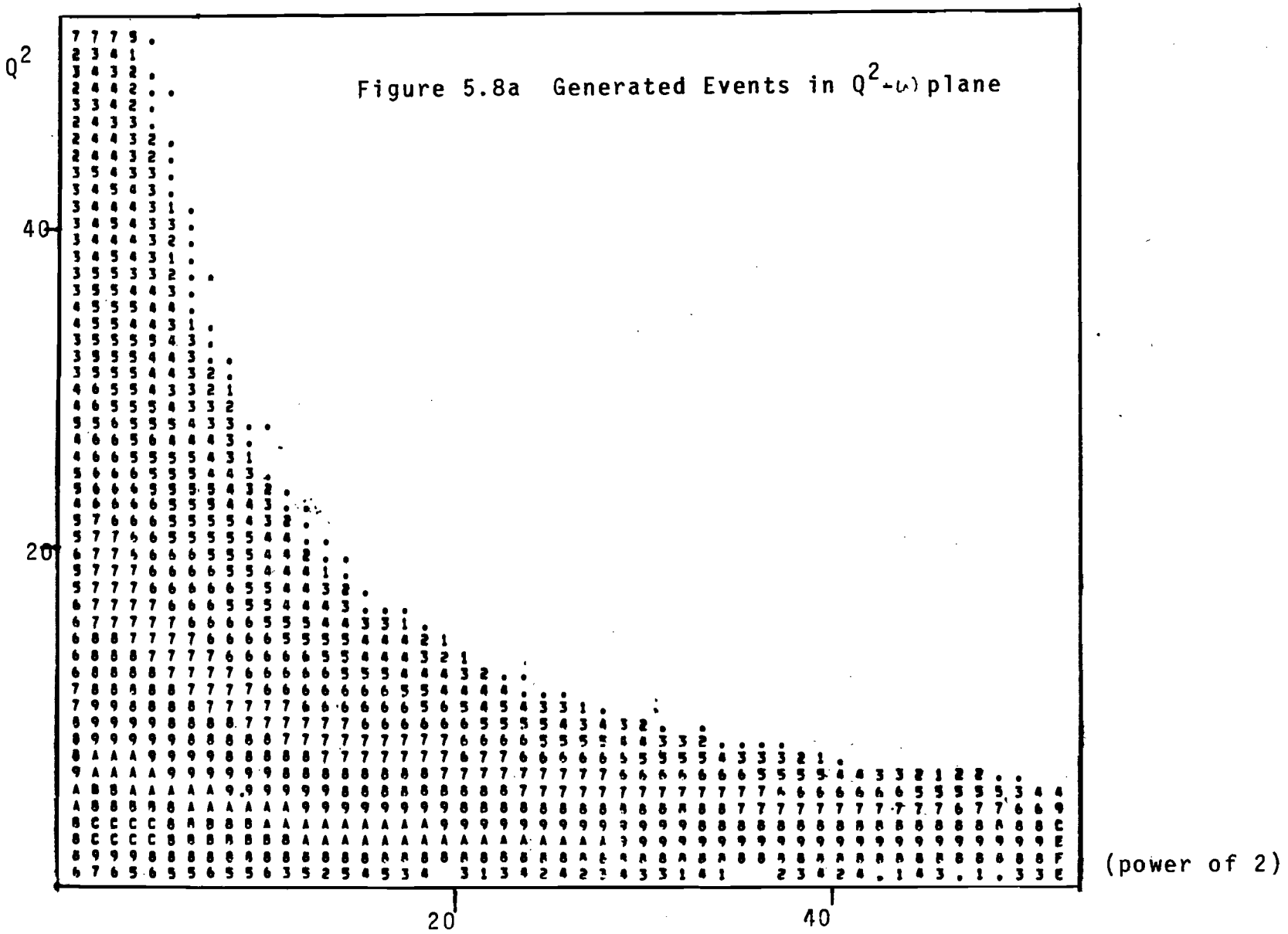

Figure 5.8a Generated Events in Q^2-ω plane

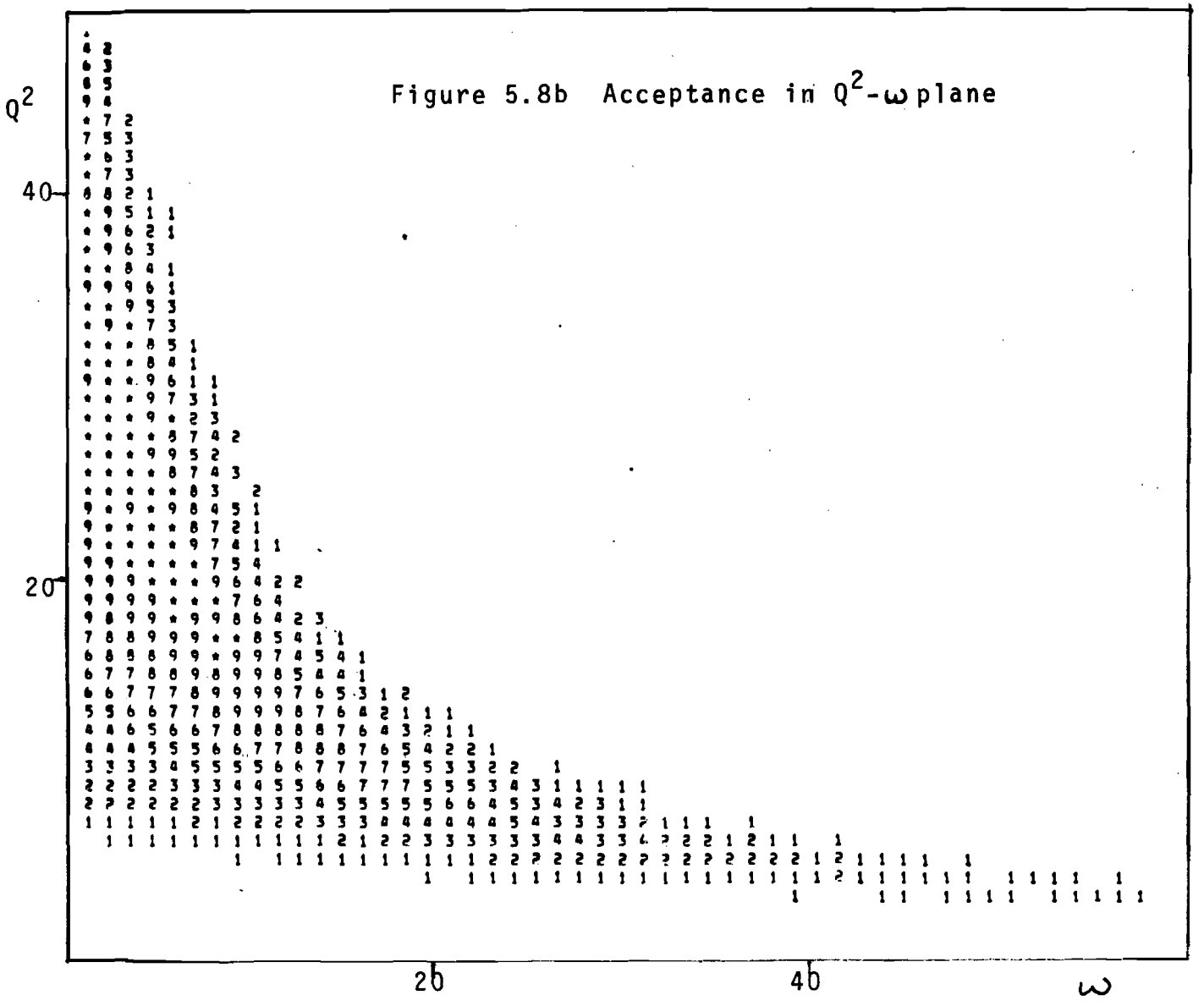

Figure 5.8b Acceptance in Q^2-ω plane

* = 100 %
9 = 90 %
etc.

D. Systematic Uncertainties

The data are subject to various systematic effects.

Some of them are smaller in taking the ratio, some are corrected by the Monte Carlo.

The possible effects, the estimated uncertainties and the effect to the constrained propagater fit are summarized in Table 5.2. The magnitudes of the uncertainties are estimated in Appendix F. The effects of errors on the constrained fit were studied by modifying the data accordingly.

The shift of the fitted value was considered to be the effect of the uncertainty.

Adding the errors in quadrature, the parameter Λ was obtained to be $1/\Lambda^2 = (27 \pm 36) \cdot 10^{-4}$GeV or $\Lambda \geq 10$ GeV/C^2 with 95% confidence.

The study of various physics effects is also made in Appendix F.

Table 5.3. Systematic errors and the constrained fit

	estimate of maximum uncertainty	$1/\Lambda^2 \cdot 10^4$ (GeV^{-2})
Fitted value	-	27^{+26}_{-23}
normalization	± 5%	$^{+15}_{-14}$
E' shift	± 1%	± 9
E_0 shift	± 0.5%	± 1
Misalignment		
$\Delta 1/E' = \alpha/E_0 \cos\phi$	α = 5%	± 9
$\theta = (1+\beta\cos\phi)*\theta$	β = 5%	±12
radius dependent bias(assuming linearity) ($+\Delta$ at r=8", $-\Delta$ at 32")		
Efficiency	$\Delta \simeq$ 2.5%	± 4
E' shift	$\Delta \simeq$ 0.5%	± 0.5
Incomplete modeling of Monte Carlo		±10
OVER ALL		27^{+36}_{-34}

VI. DISCUSSIONS AND CONCLUSIONS

A. The Parameter Λ

The propagator (or form factor) form of $(1 + Q^2/\Lambda^2)^{-2}$ has been used extensively as a convenient parametrization to express the limit to QED breakdown.

In the process of μN inelastic scattering, the parameter represents combinations of several possible effects as listed in Table 6.1.

Severe limits have been placed on most of them in recent experiments at SPEAR from $e^+e^- \rightarrow e^+e^-$ and $e^+e^- \rightarrow \mu^+\mu^-$ data. We therefore interpret a nonzero value of $1/\Lambda$ as a deviation from scaling at the nucleon vertex.

From the time of the observation of scaling at SLAC, it was known that the data showed a definite nonscaling behavior if plotted in $\omega = Q^2/2M\nu$ instead of $\omega' = \omega + M^2/Q^2$

If ω is used as the scaling variable at SLAC, $\Lambda^2 = 75 \pm 7\ (\mathrm{GeV}/c^2)^2$ is obtained.[19]

The distinction between ω and ω' is not important in the data reported here.

Table 6.1. Interpretations of Λ in $(1 + Q^2/\Lambda^2)^{-2}$

		Best limits (95% c.l.)
$\left(1 - \frac{Q^2}{Q^2 + \Lambda_\mu}\right)$	muon form factor	$\Lambda_\mu^+ > 27$ $(\mathrm{GeV}/c)^2$ $\Lambda_\mu^- > 16$
$\Lambda_{B_0}/(Q^2 + \Lambda_{B_0})$	modification of the propagator by heavy photon (e.g. Lee-Wick B_0)	$\Lambda^+ > 35$ $\Lambda^- > 47$
$\left(1 - \frac{Q^2}{Q^2 + \Lambda_P}\right)$	parton form factor	-
$\left(1 - \frac{Q^2}{Q^2 + \Lambda_e}\right)$	electron form factor (in comparison to SLAC)	$\Lambda_e^+ > 21$ $\Lambda_e^- > 19$
	μ -e universality	$\Lambda_{\mu e}^+ > 13$ $\Lambda_{\mu e}^- > 15$

$\Lambda^\pm$ are for positive or negative metrics

and $(1 \mp Q^2/(\Lambda^\pm)^2)^{-1} \simeq (1 \pm Q^2/(\Lambda^\pm)^2)$

B. Theoretical Ideas on Scaling Breakdown

The simple picture of the parton model which demonstrated scaling in an intuitive manner was field theoretically realized by Drell,Levy and Yan.[5]

The crucial assumption for obtaining scaling in this model was the need for a cut-off in the transverse momenta of partons. Without the cut-off, field theory predicts logarithmic breakdown of scaling.

A violation of the type $(1 + Q^2/\Lambda^2)^{-2}$ was suggested by Drell and Chanowitz.[20] They showed that this form naturally emerges from a representative model in which a nucleon is a weakly bound system of light constituents mediated by heavy gluons. Λ in this model is the gluon mass, which comes from the vertex correction. $\Lambda \simeq M_g \simeq 10$ GeV/c^2 was suggested from the observed deviation of the proton elastic form factor from the dipole form, and by interpreting the need for ω' instead of ω as a scaling breakdown.

West and Zerwas studied the consequences of introducing both finite sizes and anomalous magnetic moments into the naive quark parton model.[21] It was shown possible to have an observed violation of scaling in the e^+e^- annihilation process, leaving the scaling in $l^{\pm} + N$ channel unaffected. In neutrino scattering, unlike antineutrino scattering, a sizeable deviation was predicted.

The discovery of asymtotic freedom in certain gauge theories gave a natural explanation for the scaling behavior.[6]

In this picture, the coupling constants for the strong interaction become smaller at shorter distance, and the constituents behave almost free during the interaction.

Theory can calculate values of the moment integrals of the structure function. By inverting them, the behavior of the structure function as a function of Q^2 was predicted.[22]

According to the picture, the area under νW_2 plotted on $x = Q^2/2M\nu$ slowly decreases with Q^2, while the curve becomes more sharply peaked at smaller x.

Physical understanding of this behavior can be obtained in terms of the scaling invariant parton model.[23] As Q^2 gets large, the probe can resolve the next level of structures inside of partons, which carry a smaller fraction of the longitudinal momentum.

In an attempt to explain the increase of $\sigma_T(e^+e^- \to \text{hadrons})/\sigma(e^+e^- \to \mu^+\mu^-)$, Bigi and Bjorken studied the consequence of introducing a direct coupling of leptons to hadrons.[24]

The adjusted coupling constants to reproduce the data predict sizable scaling breakdown in the scattering channel.

For instance,if a scalar coupling is assumed, νW_2 scales, while $R = \sigma_L/\sigma_T$ approaches -1.

The direct coupling of leptons to hadrons naturally emergies in the unified theory of leptons and hadrons.[25]

Introducing charmed quarks and color symmetry gives a natural reason to include leptons to form SU(4) x SU(4) multiplets. The simplest model proposed by Pati and Salam predicted any sizeable effect to occur at much higher energies, but they showed it was possible to modify the theory to be relevant at SPEAR energies. The deviation from scaling in the scattering channel has terms proportional to εQ^2 and $(\varepsilon Q^2)^2$. ε is about $2\sim5\cdot10^{-2}$ GeV^{-2} to explain the e^+e^- channel behavior. The $(Q^2)^2$ term is proportional to the distribution function of the quark to which the lepton couples. If it is an n-type quark, the deviation could be as large as 50% at $Q^2 = 25$, while for the λ-type the deviation is much smaller but increases rapidly with ω at fixed Q^2.

An increase of νW_2 at large ω has been predicted phenomenologically; for instance, Nieh argued that the observed violation in the e^+e^- annihilation process should be reflected in the inelastic scattering channel at $\omega>14$.[26]

C. Summary of Results

We have made a test of Bjorken scaling in deep inelastic muon scattering by comparing two sets of data taken at 150 and 56.3 GeV at Fermilab. The apparatus was scaled so that the events with the same values of scaling variables e.g. $x = Q^2/2M\nu$ and $y = \nu/E_0$ go through the same region of the detectors at the two energies. Most of the systematic uncertainties cancel in comparing the two, thus increasing the sensitivity to the scaling behavior.

The ratios of the 150 and 56.3 GeV data corrected by Monte Carlo calculations were observed to be consistent with unity, indicating the scaling is a good approximation between the two energies. A possible breakdown of scaling was expressed in the propagator form,

$$\nu W_2(\omega,Q^2) = N(1 + Q^2/\Lambda^2)^{-2}\nu W_2(\omega)$$

By constraining N to 1 ± 0.05, the Λ from the two sets of data was observed to be

$$\Lambda^{-2} = (27 \pm 36)\cdot 10^{-4}(\mathrm{GeV}/c^2)^{-2} \text{ (9.3\% confidence)}$$

and a lower limit of Λ was obtained to be 10 GeV/c^2 with 95% confidence.

We have not excluded a smaller deviation from scaling as most theories predict, but that the scaling works to this accuracy at these energies should be regarded as a pleasant surprise. A stronger test is possible by comparing the results to the extraporation of SLAC data, which shows more clealy the direction of deviations.[28]

D. Concluding Remarks

1. SA(small angle) data

The results presented here are based on subsets of data denoted by LA(large angle). The results sent to publication includes SA data.[27] This might cause inevitable confusion to the reader. First of all the latter is the result of combined group effort based on slightly different analysis. A problem of SA data was the observed inefficiency at large radius for the 150 GeV data. Azimuthally asymmetric cuts were necessary and the result was much more sensitive to slight misalignments of the system. The problem was greatly reduced if TIEFIT was used instead of BACKFIT. TIEFIT is the momentum fit made constraining the vertex to the target center. This is used in the final result to be published, but not in this thesis work. The second reason for not including SA here is related to the emphasis of the propagator fit for the form of scaling breakdown. The SA sample did not increase the sensitivity to the parameter Λ, because the contribution is mainly at low Q^2 region, and the additional normalization uncertainty dominates the statistical gain.

But use of the SA data certainly widens the ω range investigated and gives valuable information on the high ω behavior of the structure functions.

2. The Emphasis of the Propagator fit

Use of the propagator fit has been a simple form of scaling breakdown with which to investigate the sensitivity of the apparatus and various systematic errors. The parameter Λ can be interpreted as the size of the constituents.

But the use of this form assumes a particular Q^2 dependence everywhere, and also must be unity at low Q^2. It was possible to use this form to represent the ratio of 150 and 56.3 GeV data only because the deviation from scaling in the Q^2 dependence was observed to be small.

3. Improvements of the Apparatus

The present experiment was proposed to investigate a general feature of deep inelastic scattering at higher energy available at Fermilab. Now the second generation experiments have been approved, which would increase both the kinematic region of investigation and the statistic and systematic sensitivity. Based on the experience of participating in this experiment, it may be worthwhile to make some suggestions for improvements, most of which are already incorporated.

a. On the construction

i) The spectrometer trigger counters could have a round hole to have a truly azimuthally symmetric system. The beam veto counter could be the same size as the hole.

ii) The counter bins could be azimuthal to help reconstruct tracks, or at least one of them could be horizontal allowing an efficiency map of the spark chambers.

iii) Front spark chambers should be moved into the spectrometer. Front chambers could be replaced by proportional or drift chambers. Some of the spark chambers could be placed upstream of the target to identify halo tracks both in time and out of time, although this could be physically difficult.

iv) Low Z material behind the iron magnets might be useful to absorb electromagnetic showers associated with muon tracks.

v) One of the beam chamber modules was XY instead of UVW. It is probably better to have UVW also, even if the area becomes smaller due to the limited number of ribbon cables.

vi) The carbon target placed upstream of the iron target when we were hoping to study the Z dependence, might not be a good idea, even if drift chambers locate the vertex accurately, due to the rescattering and back scattering in the main target.

b. On efficiency checks

i) A continuous check of the efficiency of each counter

bin was very important because of occasional failure of electronics. This could be monitored on-line, if the counter bins are arranged in certain ways (e.g. azimuthal bins)

ii) Overall track reconstruction could be more easily obtained if the counters are binned more finely. An efficiency check of spark chambers along the wands is also important and could be done on-line using the counter bins.

iii) To make the consistency check between Monte Carlo and data easier, some data could be taken maximizing the acceptance at the SLAC region for each energy.

c. On the Calibration of the Spectrometer

i) The incident energy could be determined more accurately by finner bins of beam hodoscopes with good alignment information. Some consideration is needed to place a limit to the low energy tail in the beam, possibly using cyclotron magnet upstream.

ii) The magnet power supply needs to be monitored more accurately.

iii) Extra material at 150 GeV configuration was needed for the scaling purpose, and magnets were degaussed. The degaussing procedure was tedious, and probably it would be better to substitute non-magnetic material.

iv) Alignment of the system was not crucial due to the

azimuthal averaging, but needs a better method.

d. On Electronics and other matters

i) The proportional chamber strobe signal to latch signals from chambers had better be the event trigger itself. The reason why we could not was because of the insufficient length of ribbon cables. Also the gate width could be reduced.

ii) Obviously the photo tubes need high voltage "boosts" for high intensity beam.

iii) The coincidence of beam veto counters placed at different amount of absorber was a very good idea. But is it still possible at higher intensity?

Appendix A

DETAILS OF APPARATUS

1. Muon Beam

1) Extracted protons

The proton beam was accelerated to 300 GeV at Fermilab, and was extracted in a combination of fast and slow extraction modes during the flat top period of about 400 to 600 msec.

The extracted proton beam (typically $3\sim8\times10^{12}$ protons per pulse) was transported to the switchyard where it could be split to the three main experimental areas, west to Meson, east to Proton, and straight to Neutrino areas (Figure A.1).

2) Front end

The proton beam was focused at the production target made of 12" long aluminum. Two sets of configurations were used in accepting the produced hadrons and in focusing into 400 m long evacuated decay pipe. Dichromatic train load was designed to produce narrow band sign selected neutrino beam.[30] This was used in this experiment during August and October in 1973 for the 150 GeV running

Triplet train load was designed to increase the muon flux especially at lower energies and was used during April in 1974 for 56.3 and 150 GeV running.[30] The characteristics of these are summarized in Table A.1.

Figure A.1

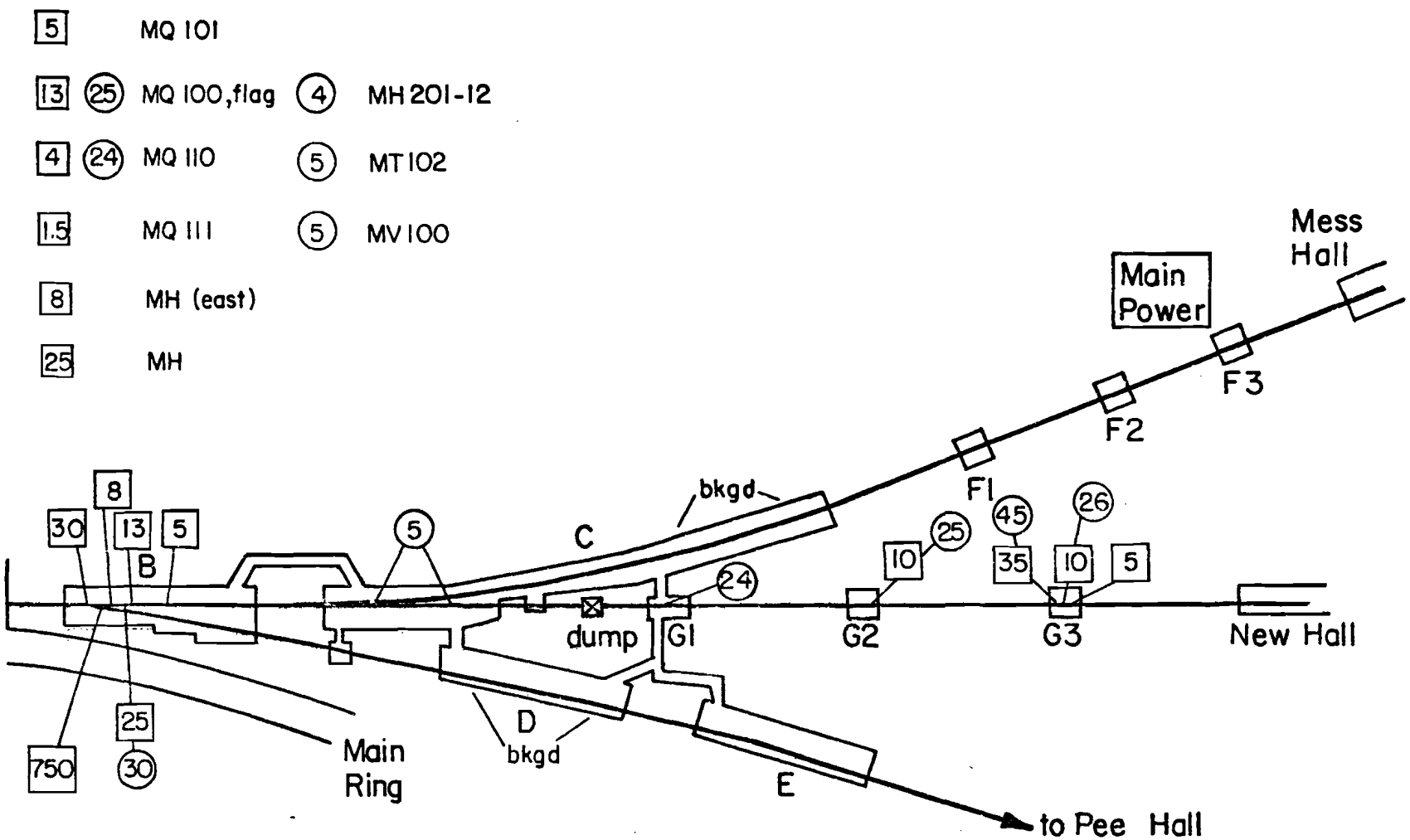

SWITCHYARD

Table A.1. Front End Parameters

		Dichromatic train	Triplet train	
Tuned momentum		156 GeV/c	60 GeV/c	156 GeV/c
Used in this experiment in		August 1973 and October 1973	April 1974	April 1974
Production angle (mrad)		0	0.5	0.5
Production target		12" aluminum	12" aluminum	12" aluminum
Beam spot size: Horizontal		0.07"	0.10"	
Vertical		0.118"	0.10"	
Solid angle acceptance (μstr)		11.63	2.2	
Angular acceptance (mrad)	Horiz.	±3.04	±1.53	±3.5
	Vert.	±1.22	±2.54	±3.0
Muon/proton		$10^{-8} \sim 10^{-7}$	$\sim 10^{-7}$	$\sim 10^{-7}$
Halo/beam		$0.4 \sim 1.0$	$0.6 \sim 1$	$0.6 \sim 1$

3) Muon beam line

About 5% (15% at 56 GeV run) of the pions decay into muons and neutrinos in 400 m of evacuated decay tube. At the end of the decay tube, muons were captured and separated from neutrinos by bending magnets. The beam was further bent to the east and to the west alternately to form the beam line parallel to the neutrino beam line. A 28.68 mrad bend angle was provided by three 20' long bending magnets at each bend point.

A 40 feet polyethylene absorber was embedded in bending magnets in Enclosure 102, in order to remove the remaining hadrons. Angular divergence caused by the decay and the multiple scattering in the absorber was cancelled by quadrupoles in Enclosures 101 and 103, respectively.

Table A.2 lists the parameters of this Mark II design.

Table A.2. Parameters of Muon Beam Line

Name	Enclosure	Function	Size (H*V*L) (inches)	z	y	P (GeV)/I(A) or G(KG/in)/I(A)
Target	E99			3484"	-0.667"	
				4848"	-0.620"	
1W0	E100	Bend to west	4*4*240	4886	-0.260	0.0474
				4936	+0.700	
1V01		Vert. vernier	4*4*30	4948.4	1.008	
1Q0		Quad	5D*36	5005		0.00417
				5045		
1Q1	E101		3D*84	5336.5	12.14	0.00137
				5345.5	12.40	
1E1				5365.0	12.91	
		Bend to east	4*2*240	5386.4	13.32	0.0735
				5407.8	13.52	
1V1		Vert. vernier	4*4*30	5419.8	13.57	
	E102			5819.0	13.62	
1W2		Bend to west	4*2*240	5840.4	13.82	0.0735
				5861.8	14.23	
1V2			4*4*30	5873.9	14.53	
	E103			6042.0	19.36	
1F3		Quads		6048.0	19.53	
		Horiz. focus		6054.0	19.70	
			12D*48	6076.0	20.33	4.50
1D3		Quads		6082.0	20.50	
		Horiz. defocus		6088.0	20.67	
1E4	E104	Bend to east		6333.9	27.68	
			4D*240	6355.3	28.09	0.0474
				6376.7	28.30	

2. Proportional Chambers

Construction

Cross-sectional view of a proportional chamber is shown in Figure A.2. A wire plane of 2 mm spacing was sandwiched between two aluminum foil high voltage planes separated by 1/4". The guard strips and grooves were to avoid edge breakdown. Chambers were made gas-tight by 6 mil Kapton film as seals at both sides.

1/16" and 1/32" thick strips of G-10 were combined and glued to make picture frames of 12"x12" outer dimension with 10"x10" holes. Four of these 1/4" thick frames made one chamber.

To keep the separation between high voltage planes and wire plane uniform, the inner two pieces were glued while a hydraulic press kept them at a uniform thickness. These frames were carefully polished.

The outer two pieces were glued onto a tightly stretched 3 mil aluminum foil. The inner two pieces were glued to this, making a top half and a bottom half. Gas circulation holes, high voltage terminals, etc., were put on. These two halves were then glued onto a stretched 6 mil Kapton film for a gas seal. Finally, the wires were strung and soldered onto printed circuit boards.

Twenty micron thick gold plated tungsten wires were strung by hand using spacing bars, applying approximately

Figure A.2

CROSS SECTIONAL VIEW OF A PROPORTIONAL CHAMBER

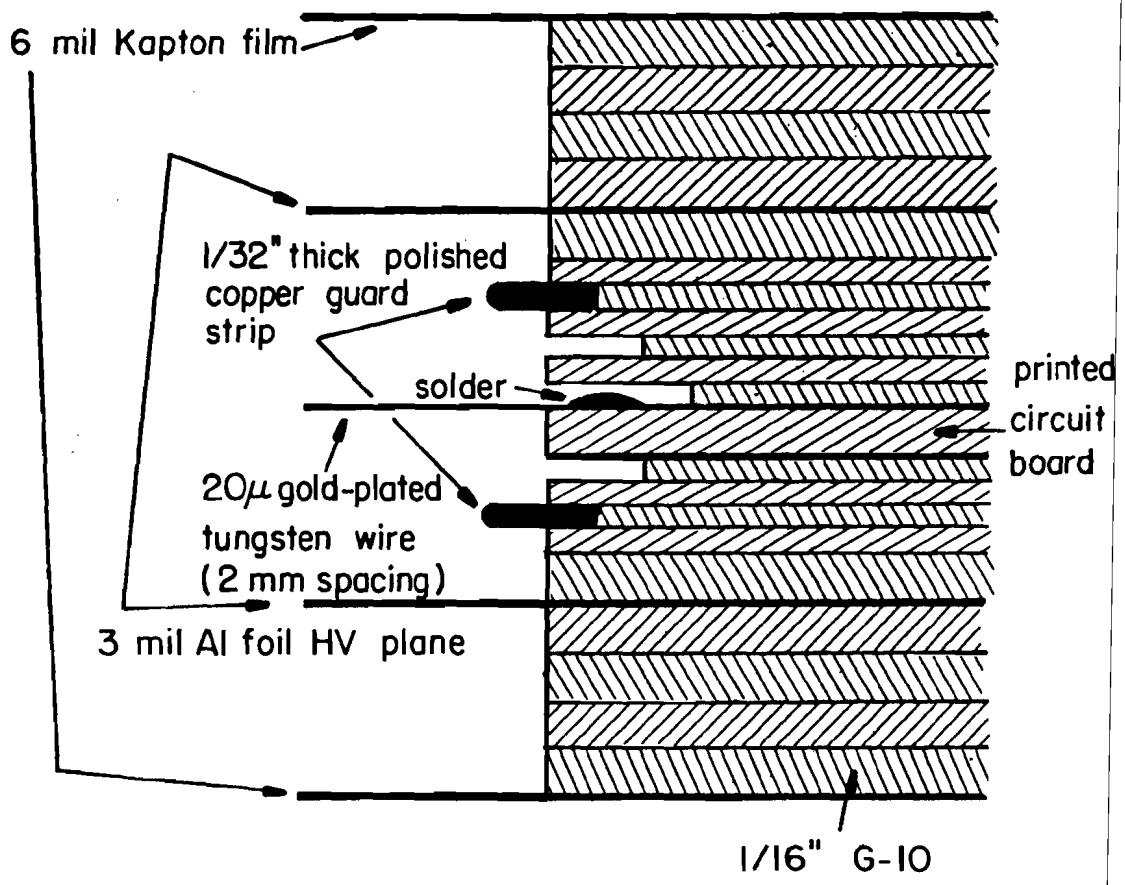

08/0375

50 grams of tension. Ninety-six wires were thus soldered, and the last four wires at either end were made progressively thicker to prevent edge breakdown.

Finally, after cleaning and checking, the top half and the bottom half were glued together, and a gas seal was made with epoxy.

Operation

We used so-called magic gas: 66% Argon, 34% isobuthane, 0.16% Freon-B1. Argon gas was bubbled through methylal kept at $0^{\circ}C$. The methylal was to prevent accumulation of fragmented hydrocarbon compounds on the wires. The gas was mixed by keeping the pressure of Argon and isobuthane at 2 to 1, going through equal lengths of catheter tubing. The gas was vented out after going through outlet bubblers.

High voltages to each chamber were adjusted in 70 volt steps using a Zener diode chain. Typical voltage was -5kV.

The principle of operation is the same as a proportional counter. The wires acquire positive charge because of the high voltage.

Electrons released by ionization due to charged particles are attracted toward the nearest wire and accelerated due to an increasingly strong electric field. They start releasing more electrons and develop an avalanche. This gives the fast rise for the signal pulse, while the long tail is due the

positive ions repelled away from the wire. The signals from the wires are amplified and discriminated individually and are latched in when a desired event occurs.

The signals from each wire were amplified at the chamber, by the circuit shown in Figure A.3. Each amplifier card contained 16 channels. The circuit had a threshold of about 5 mV with high rejection ratio for induced positive going signals. The individual amplified signals were transported to the latch system by 100Ω ribbon cables. One cable contained 32 channels, and each channel consisted of three signal wires, up, down, and ground to avoid cross talk and noise pickup.

The latch circuit is shown in Figure A.4. Each latch card contained 32 channels and was plugged into a CAMAC slot.

Table A.3 summarizes the parameters of construction and operation.

Figure A.3

CHARPAK DISCRIMINATOR

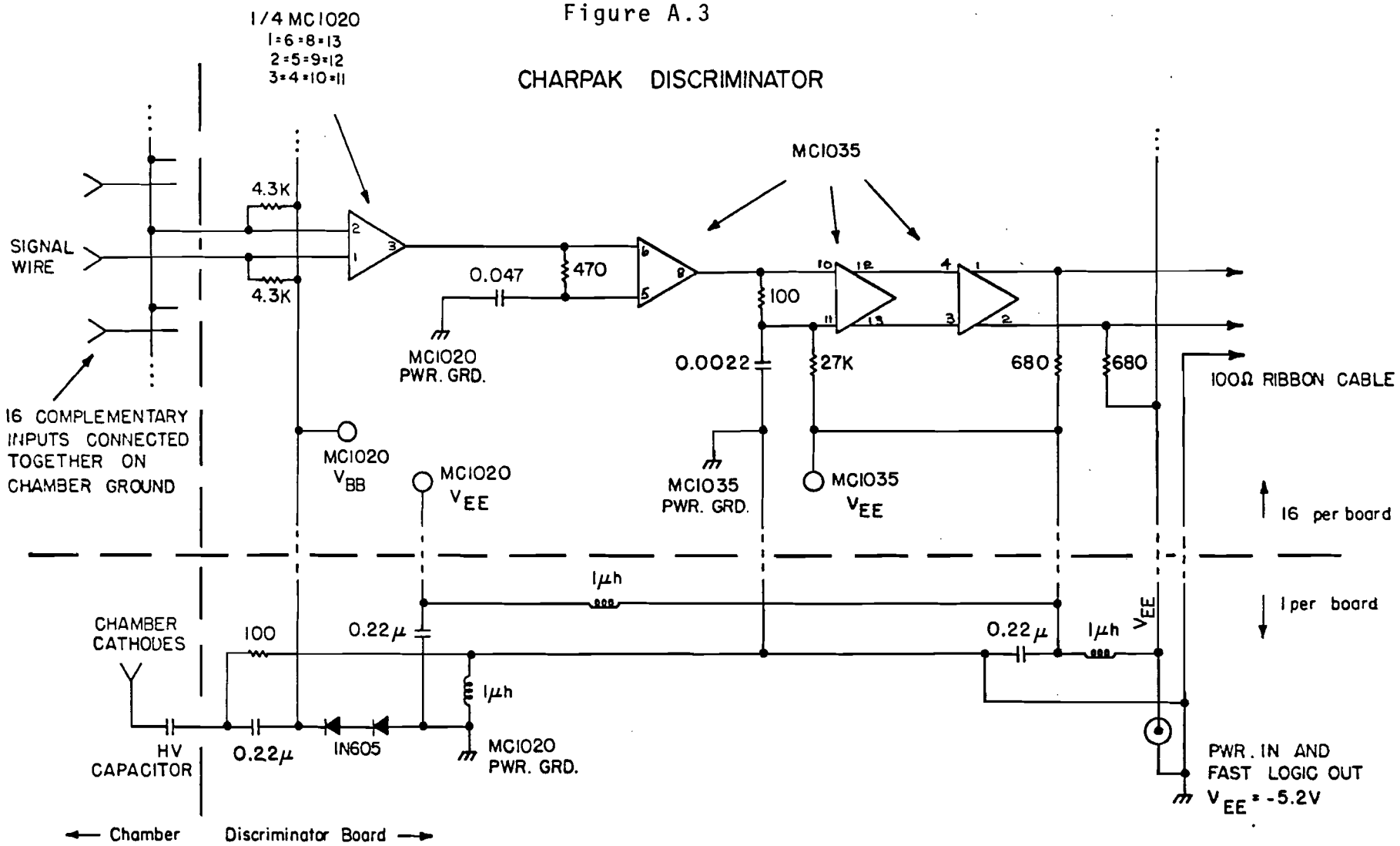

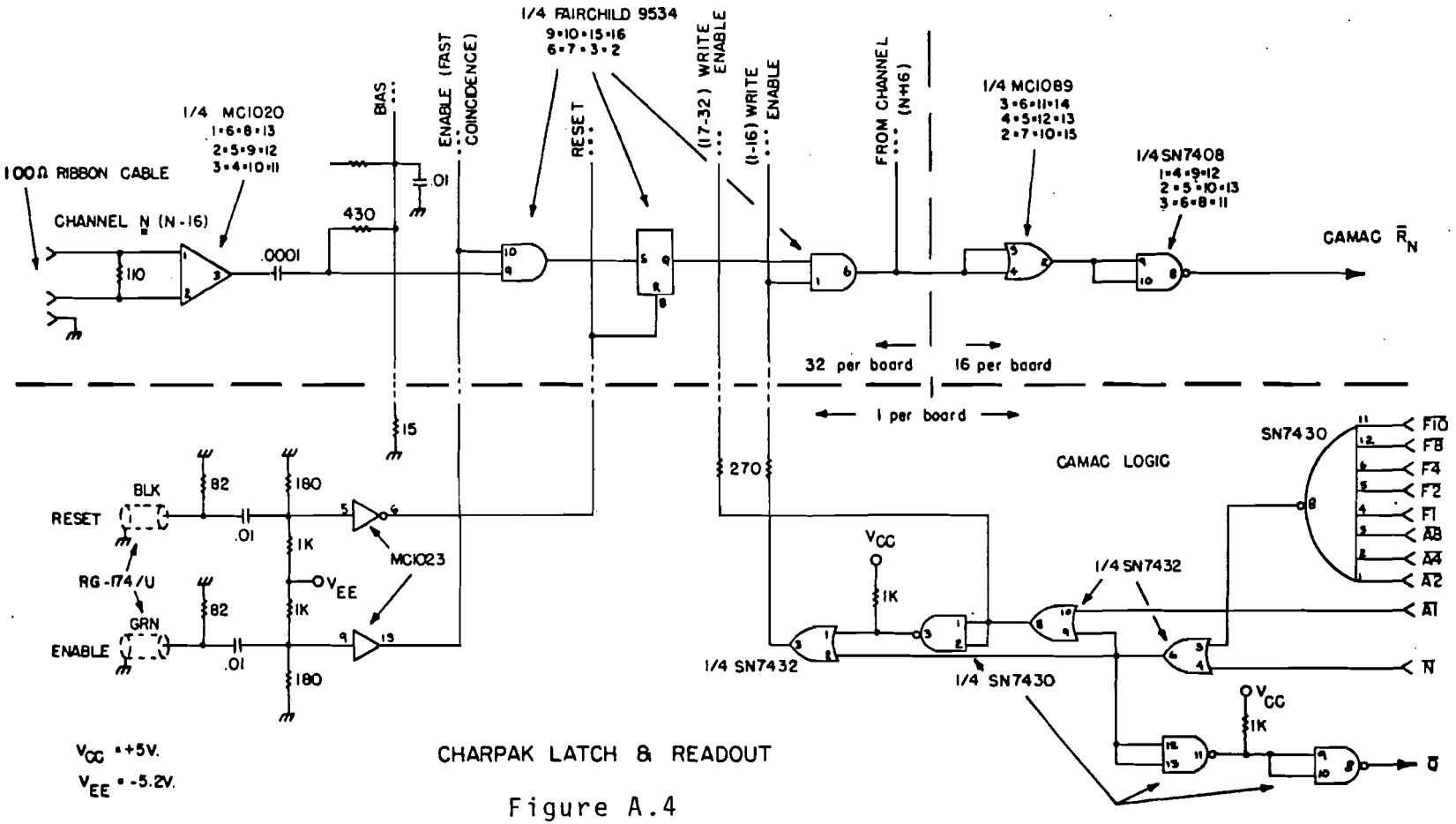

CHARPAK LATCH & READOUT

Figure A.4

0810375

Table A.3. Construction and Operation of Proportional Chambers

1) Construction	
Wire	20 μ thick gold plated tungsten. Tension 50 gm.
Wire spacing	2 mm
Number of wires	96 for beam chambers 182 for scattered muon chamber
High voltage plane	3 mil aluminum foils, 1/4" above and below the wire plane.
Frame	Mainly 1/16" thick G-10 glued to make a uniform thickness
Guard strips	1/16" thick copper, 1/8" sticking above and below the wire plane at either end
Gas seal window	6 mil Kapton film
2) Operation	
Gas mixture	66% Argon balanced with 0.24% Freon B1, 34% Isobutane bubbled through $0^{o}C$ methylal
High voltage	-4.2 to -5.0 KV adjusted by zener diode chain divider. Guard voltage -0.8 kV
Amplifier	Gain of about 2000; threshold 5 mV; rejection of positive 200; typical output ±0.7V; 16 channels/card
Ribbon cables	Transmit signals and give enough delay (0.67c), 32 channels/cable; 3 wires/channel (up-down-ground) (100Ω).
Latch	Latch each channel with gate width 75 ns; dead time for reset 120 ns.

3. Wire Spark Chambers

Construction

The chambers were made by winding 5 mil thick Be-Cu wire on rigid 80"x80"x1" plates shown in Figure A.5. The plate was made of 4"x1"x80" or 72" pressed wood, gluing 25 mil aluminum plates at both sides. The inside was stuffed with 1" thick hexell material and styrofoam. 0.75" diameter fiducial holes were drilled at the four corners for optical alignment and for the support in assembling a module out of two chambers. The holes were stabilized by gluing a 1/8" thick aluminum piece into the recessed places.

The plates were routed, sanded and painted for the gas seal.

Six 1/4" diameter holes were drilled at 8" inside from either edge for the gas holes. 1/4" G-10 tubings were glued into the holes with 1/4" sticking out. 1/2"x1"x72" rectangular aluminum tubings were glued to these for the gas manifold.

After gluing the spacing material ABS, and the bus bar, the wire was wound on the two plates at the same time held back to back. Then 1/4" and 3/16" thick 1" wide lucite windows were glued for the gas seal. The wires were soldered to the bus bar by folding back 4 mil copper shim stock. The resulting plate is shown in Figure A.6.

Figure A.5

CONSTRUCTION OF A SPARK CHAMBER - PLATE

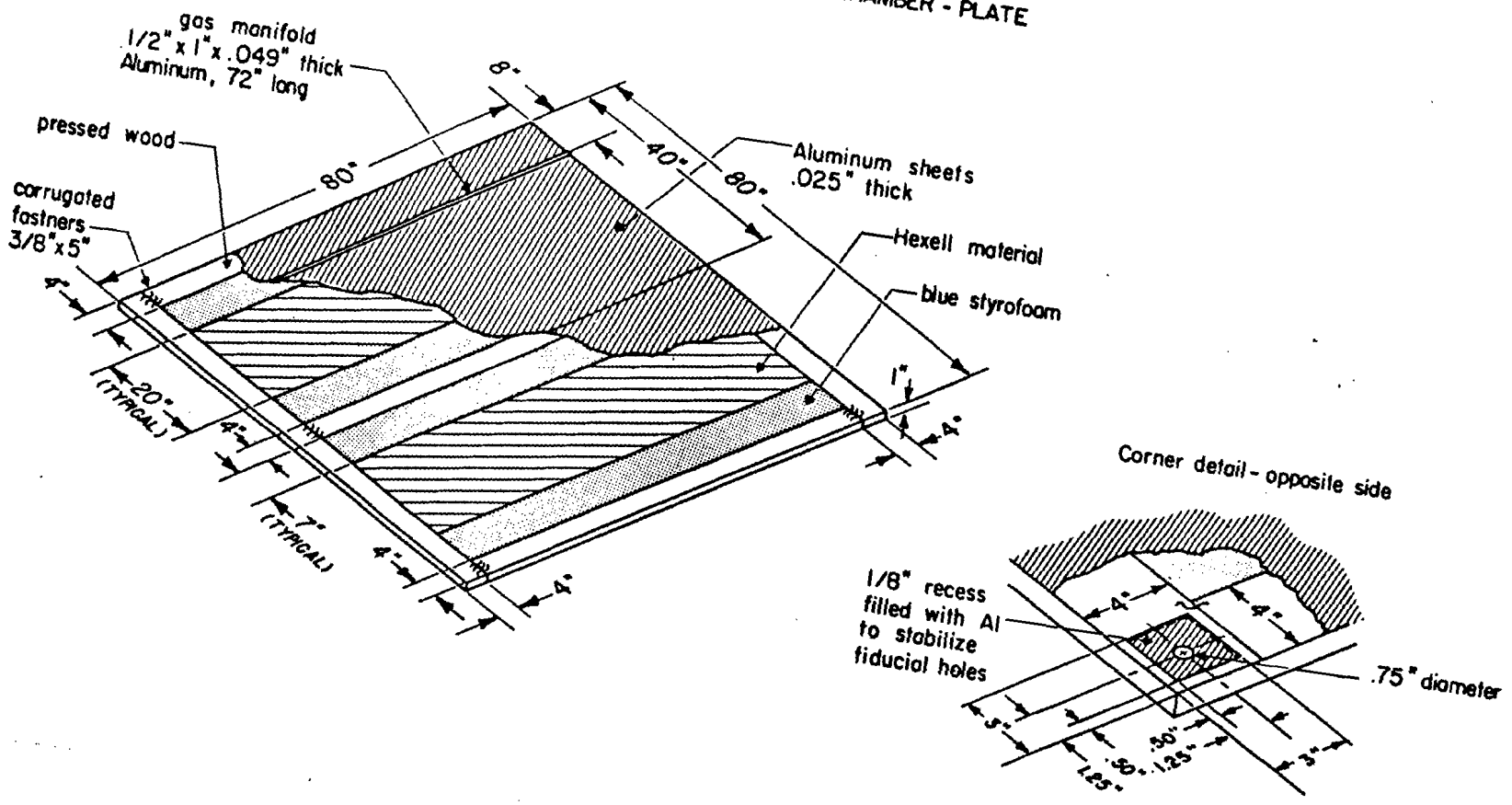

0810375

Figure A.6 1/2 Plane - a second is orthogonal to this

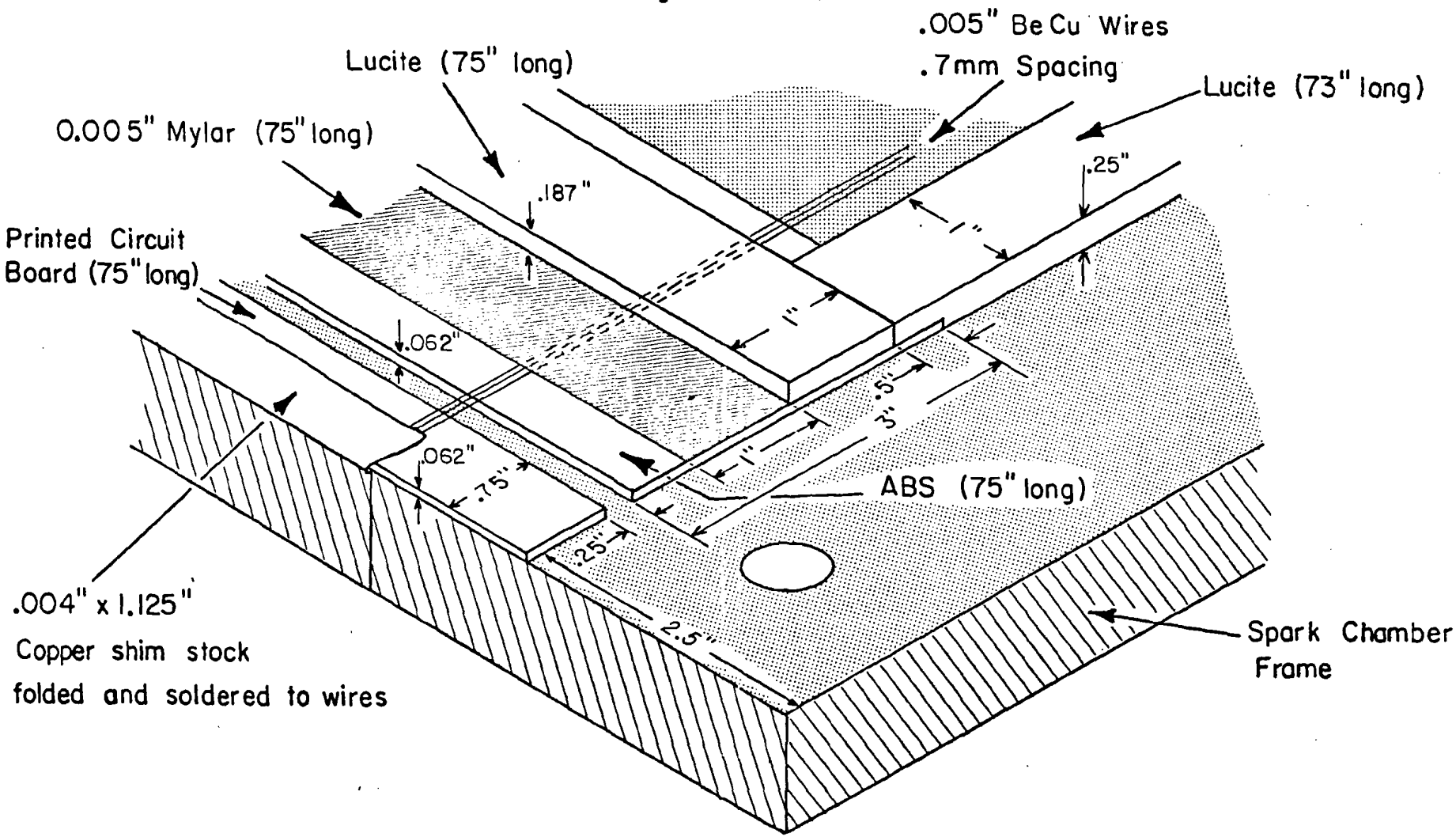

WINDOW AND WIRE PLANE

0810375

Two plates were glued together with the wire planes orthogonal to each other to make one chamber. Two chambers were assembled to make one module. One chamber was rotated by 45° to the other.

The combined chambers were suspended from the top of a frame made of aluminum angle. The height, the tilt, and the side motion could be adjusted by the top screws. The frame had a V block at one side of the bottom and a U block at the other to fit on the rails accurately.

Operation

Spark chambers were filled with 80% neon, 17% helium, and 3% argon, 3-5% of which flowed over 88°F isopropyl alcohol. The gas was purified and recirculated at the rate of about 2 cubic feet/hour/module, using an LBL recirculator. Argon improves spark formation time and helps suppress edge breakdown. The alcohol limits spark currents, improving multiple track efficiency and kills metastable states.

The operation of the spark chamber is illustrated in Figure A.7a, and the actual triggering logic is shown in Figure A.7b.

Sound waves caused by spark current flowing across a magnetostrictive wire travel along the wire at a speed of about $5.3*10^{5}$ cm/sec (or 1.7 μsec/cm) and are picked up by a coil wound around one end of the wire.

Figure A.7a SCHEMATIC OF SC OPERATION

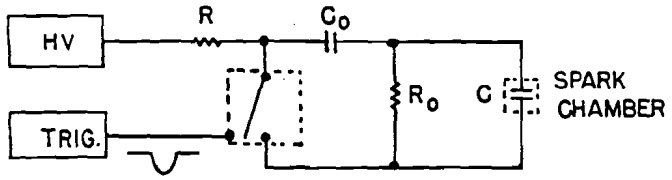

Figure A.7b SPARK GAP CIRCUIT

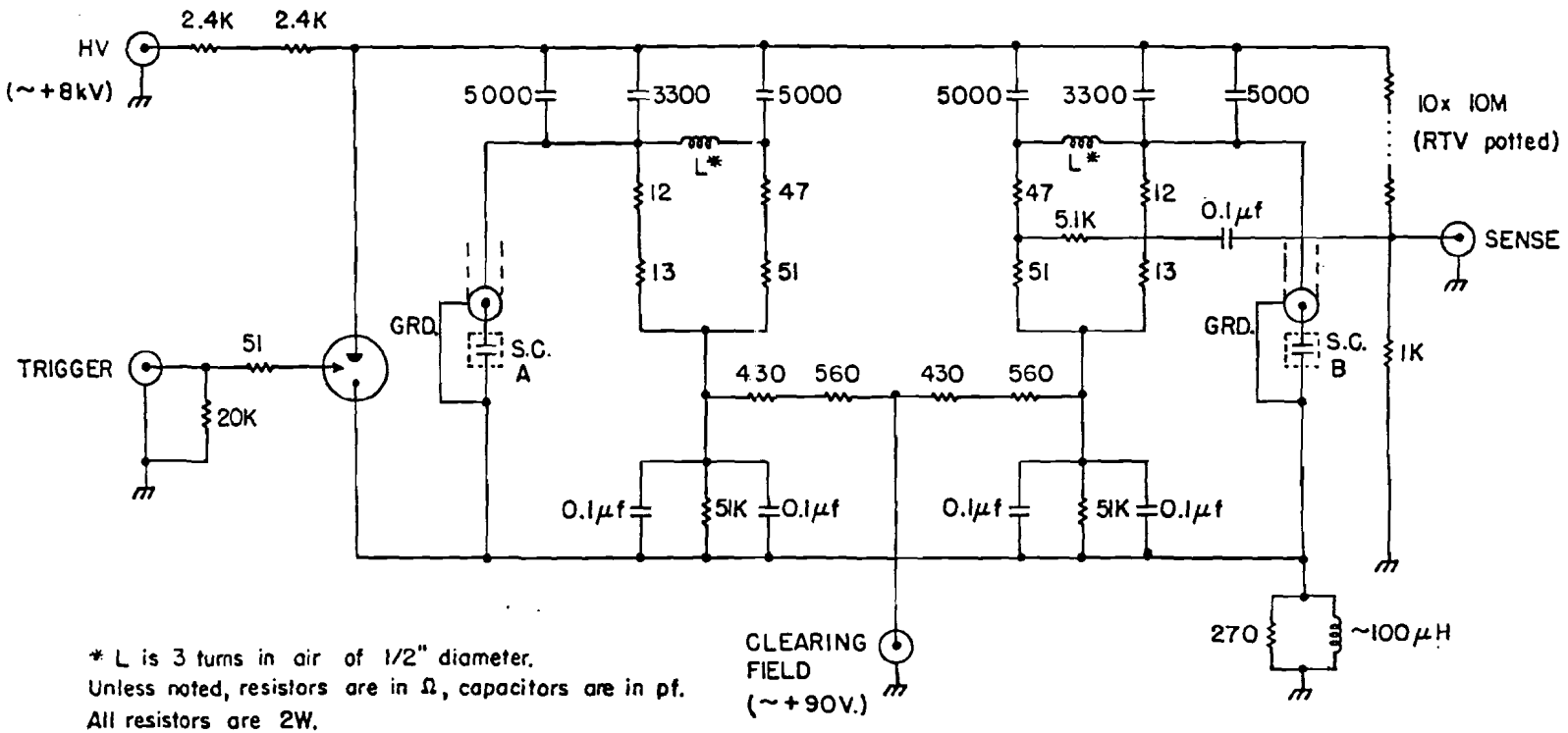

* L is 3 turns in air of 1/2" diameter.
Unless noted, resistors are in Ω, capacitors are in pf.
All resistors are 2W.
2 x 15Ω 2' long cables in parallel to each chamber.

Part of the spark current flow through wires at either end and formed fiducial signals to take out the temperature dependence and other effects. The time difference in the arrival time relative to the two fiducials represents the distance along the wand where the spark occurred.

The picked up signal was amplified by the circuit shown in Figure A.8.

The amplified signals were sent to the discriminator by a coaxial cable, which was also a power line. The signals were discriminated and the position of the peak was determined accurately by differentiating and zero-crossing the pulses by the circuit shown in Figure A.9. The standard pulses were then fed to the time digitizer.

Time digitizer converts the pulses to the 20 MHz scaler counts corresponding to the distance along the wand. The time digitizer system consists of a control module and 10 data modules, each of which fits into a normal CAMAC station. Each data module contained four independent input channels corresponding to four coordinates of a spark chamber module. Each channel was capable of digitizing up to eight sparks including the first and second fiducials. A simple schematic of the system and the timing is illustrated in Figure A.10. The control module has a 20 MHz clock and a 14 bit scaler. The scaler started counting the clock pulses when an event trigger opens the gate. Each bit of the scaler

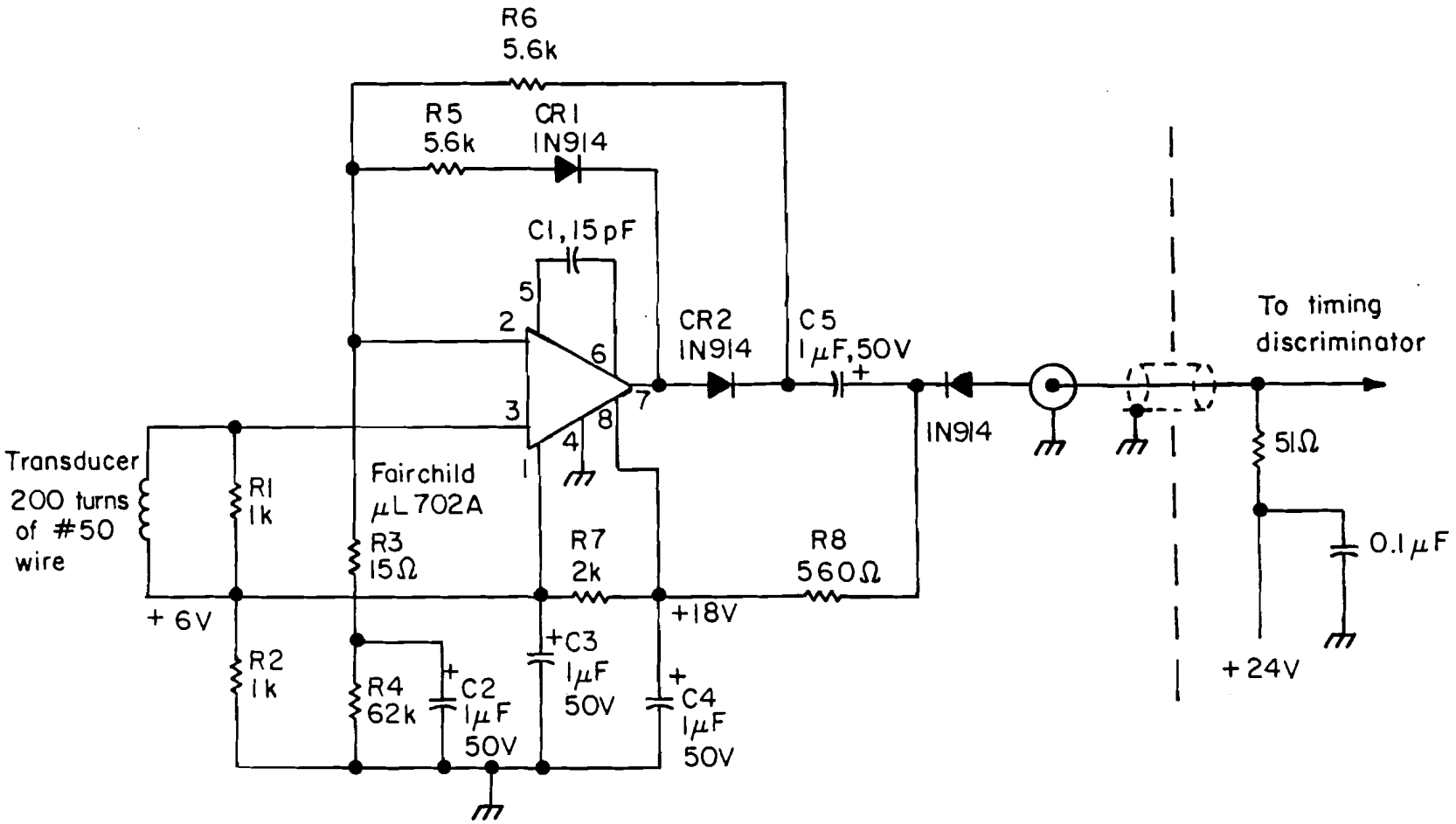

Wand Amp Circuit

Figure A.8

0810575

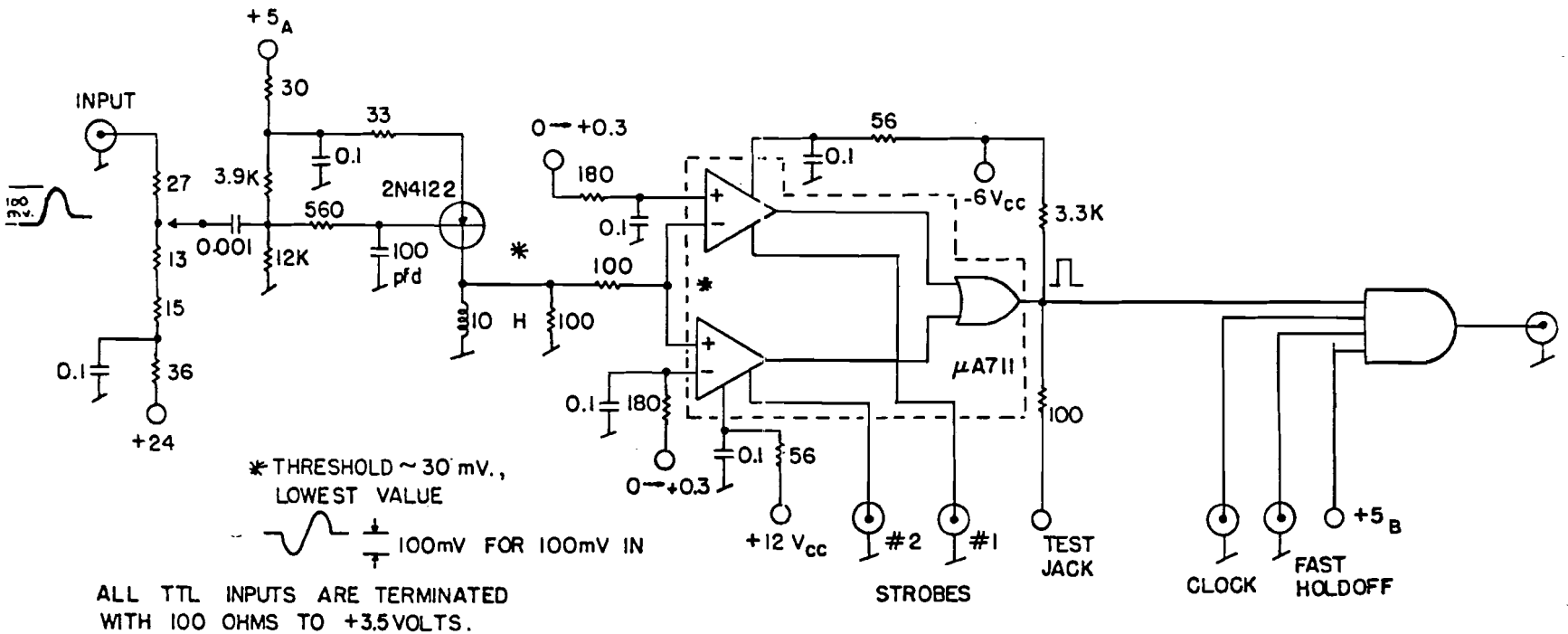

ZERO CROSSING PEAK DETECTOR

Figure A.9a

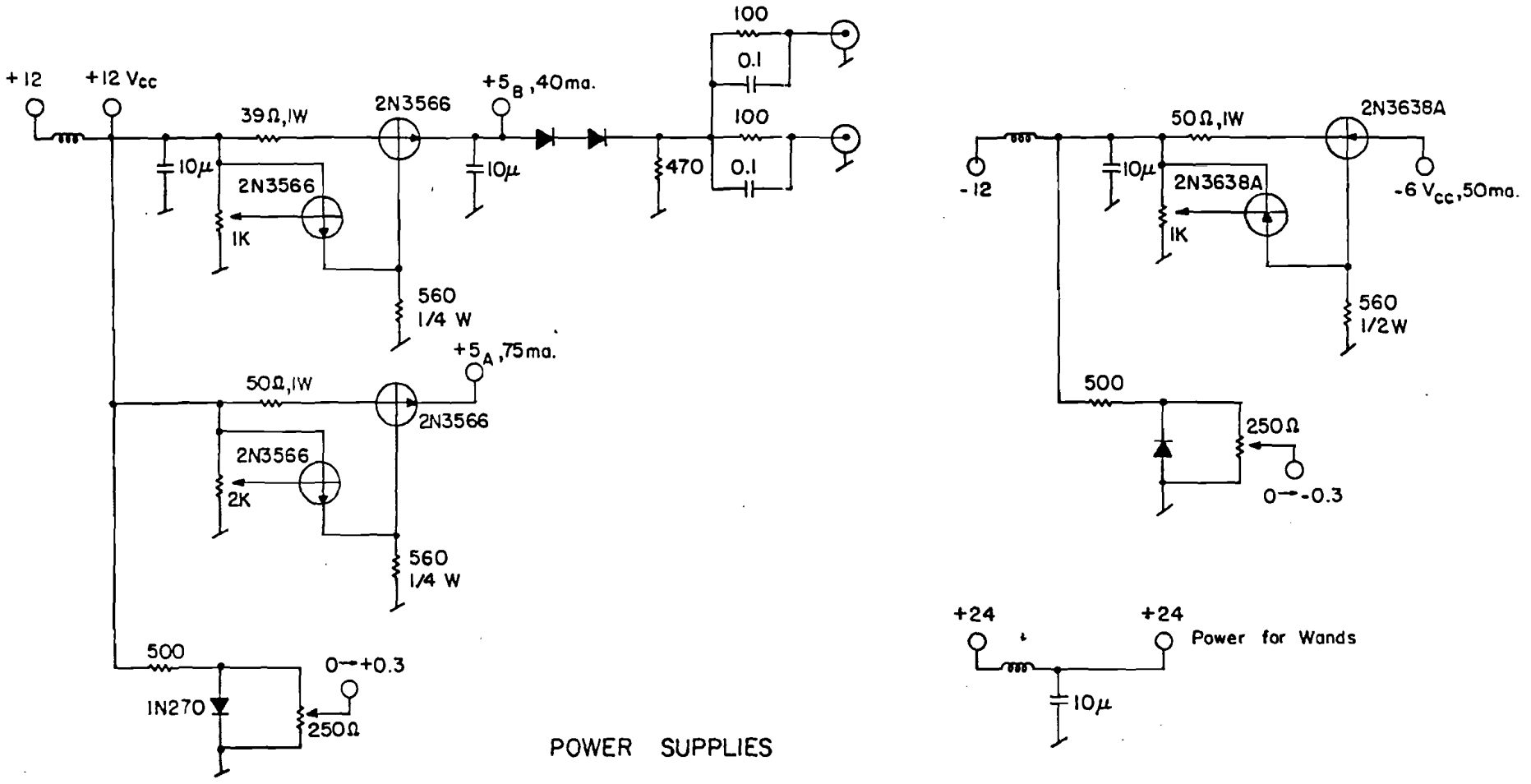

POWER SUPPLIES

Figure A.9b

0810375

was gated out to a CAMAC write line and was presented to shift registers of the data modules. A pulse from a wand "froze" the on-off pattern of the scaler storing the 14 bits into a shift register. Arrival times of up to eight sparks were thus stored into 14 shift registers. They were read out on a first in-first out basis. In each read cycle, the bits were shifted toward read lines by one bit by making use of a two-input-multiplexer at the data input of each register.

Table A.4 summarizes the parameters of construction and operation of the spark chambers.

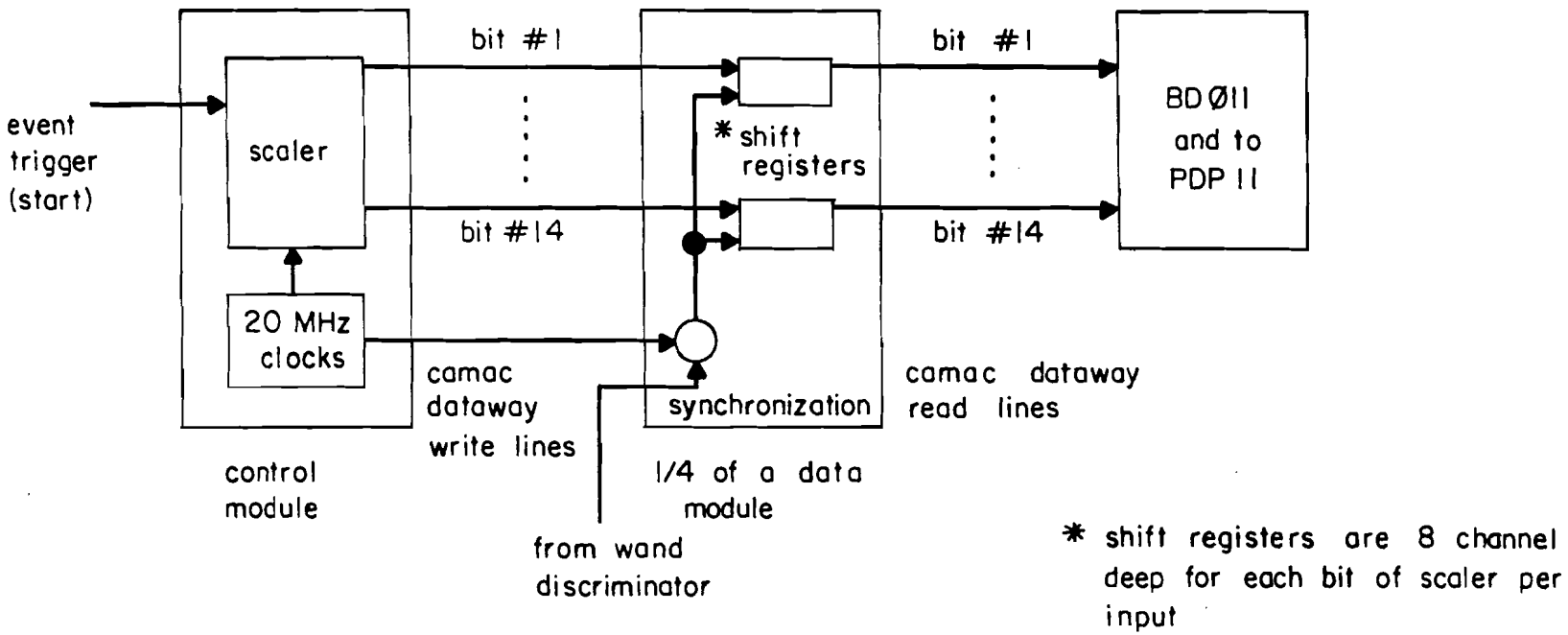

Simplified Schematic of Time Digitizer System

Figure A.10

Table A.4. Construction and Operation of Spark Chambers

1) Construction

Plate	4"x1" pressed wood, glued to make 80"x80" frame
High voltage and ground plane	0.025"x80"x40" aluminum sheets glued to each side of the plate. Stuffed with 1" thick foam inside
Wire	0.005" thick Be-Cu wire, tensioned 1 lb/wire to prevent sagging.
Wire spacing	0.027"
Gap spacing	0.5"

2) Operation

Read-out	Magnetostrictive wire. 5mm/μs
Amplifier	500 gain. LRL clipping amplifier
Pick-up coil	200 turns, #50 Cu wire
Time digitizer	20 MHz scaler (4 counts/mm), 8 sparks/wand
Gas filling	80% Ne + 17% He + 3% Argon + iso-propyl alcohol recirculated
High voltages	Typically 8 kV, 90 volts steps for the distribution
Cleaning field	+90 V
Trigger delay	About 300 ns after track went through
Spatial resolution	∿0.7 mm/plane
Memory time	∿1 μs
Recharging time	40 msec

Appendix B

DETAILS OF ANALYSIS PROGRAM

1. Track Reconstruction in the Spectrometer

The scattered muon tracks were reconstructed starting from the downstream end of the spectrometer.[29]

First, lines were established in the last three modules and then points were sought in the modules in the spectrometer by extrapolating these lines as a function of momentum.

The reason for reconstructing tracks from the back is that the front chambers were often flooded by showers originating from produced hadrons. These showers were mostly absorbed by the solid iron magnets and the concrete plugs in the hole of magnets, and the chambers behind the iron magnets were protected from them.

These chambers, however, occasionally contain extra sparks from electromagnetic showers associated with the muon track either due to knock-on or e^+e^- pair production in the iron. Most of the extra sparks could be avoided by making the windows of point finding and matching of XY-UV chambers small. Notice also that the losses due to this process are uncorrelated between the modules separated by magnets.

A rough sketch of each step in the analysis program is given below. The terms used are defined in Table B.1.

Table B.1. Terminology for Track Reconstruction

Modules	Proportional and spark chamber modules are numbered 1 through 15 from up- to down-stream. #1-#6 are proportional chambers. #7-#15 are spark chambers. #1-#4 were used to reconstruct beam track.
Spectrometer	Consists of modules #5-#15, iron magnets and trigger counters. #11-#15 are called the spectrometer chambers.
Front	Modules #5-#10 are after the target but before the iron magnets to detect the scattered muon angle.
Rear	Modules #13-#15 downstream of all the iron magnets.
X, Y, U and V views	Spark chamber modules #7-#15 consists of two gaps or four wire planes. XY chamber is vertical - horizontal, and UV chamber is rotated by 45° clockwise looking downstream. The separation of XY and UV is about 2 3/4".
Wires	Corresponds to the coordinates along the magnetostrictive wire converted from time digitizer counts.
Lines	Straight lines in the modules #13-15.
Matches (points)	Wires in each view in a module are combined to get the spatial coordinates of points. 4-way is the highest quality, 3-way follows, and 2-way is the lowest.
DCR confirmation	Spectrometer trigger banks, SA, SB and SC consisted of five vertical bins. Each bin was latched into DCR (Discriminator Coincidence Register). The DCR has a time resolution of 50 ns compared to 1 μs for the spark chambers. The reconstructed points were tested for consistency. The test was used to order the priority of tracks.

1) Line Finding in the Rear

The last three modules were downstream of all of the magnets and therefore the scattered muon tracks were straight lines. Lines were sought in each coordinate view, finding the set of wires satisfying the linearity equation,

$$\left|\frac{z_{15}-z_{14}}{z_{15}-z_{13}}\,x_{13} + \frac{z_{14}-z_{13}}{z_{15}-z_{13}}\,x_{15} - x_{14}\right| < w_\ell$$

(similar equations for y, u, and v view)

where subscripts are the module numbers and w_ℓ is the window. Figure B.1a shows the histogram of this quantity.

The lines in each view were combined and lines were confirmed if at least one wire in additional view is within the matching windows. The line finding efficiency was studied as a function of the window w_ℓ and set to 2 mm, where the plateau was stable.

Note that the minimum requirement to reconstruct a line is straight lines in at least two views plus one confirming spark in the other views.

2) Point Finding in the Spectrometer

The established lines in the rear were extrapolated into the spectrometer and points at a module in the spectrometer were predicted as a function of momentum of the track.

The prediciton of points was expressed as follows:

$$x_m^{pred} = x_m^{(0)} + x_m^{(1)}k + x_m^{(2)}k^2 \qquad (m = 11 \text{ or } 12) \qquad (B.2)$$

where m is the module m, k is the curvature ($\propto 1/P$) and $x_m^{(0)}$, $x_m^{(1)}$, and $x_m^{(2)}$ are coefficients calculable once a line is given.

The window to look for points about this prediction has the shape shown in Figure B.2 (and named "hourglass"), originating from two components, momentum dependent and independent. The former is due to the multiple scattering error and the latter is due to the extrapolation and measurement errors. This window was realized in analytic approximation and was found later to break down if a parameter of the window was made too large. But the efficiency was studied and found to be satisfactory at the chosen value.

At first, wires were selected in module #12 within the boundary of this hourglass window. As the observation of a wire corresponds to a measurement of momentum, or the angle, the effect of finite separation between XY and UV chambers could be corrected.

Selected wires in each view are matched to obtain the spatial coordinates. The histogram of matching is shown in Figure B.1b. These points were tested further if they were within the hourglass window as described below.

For each point in module #12, a window was opened in module #11 using the obtained momentum information to

Figure B.1 Line Finding in the Rear

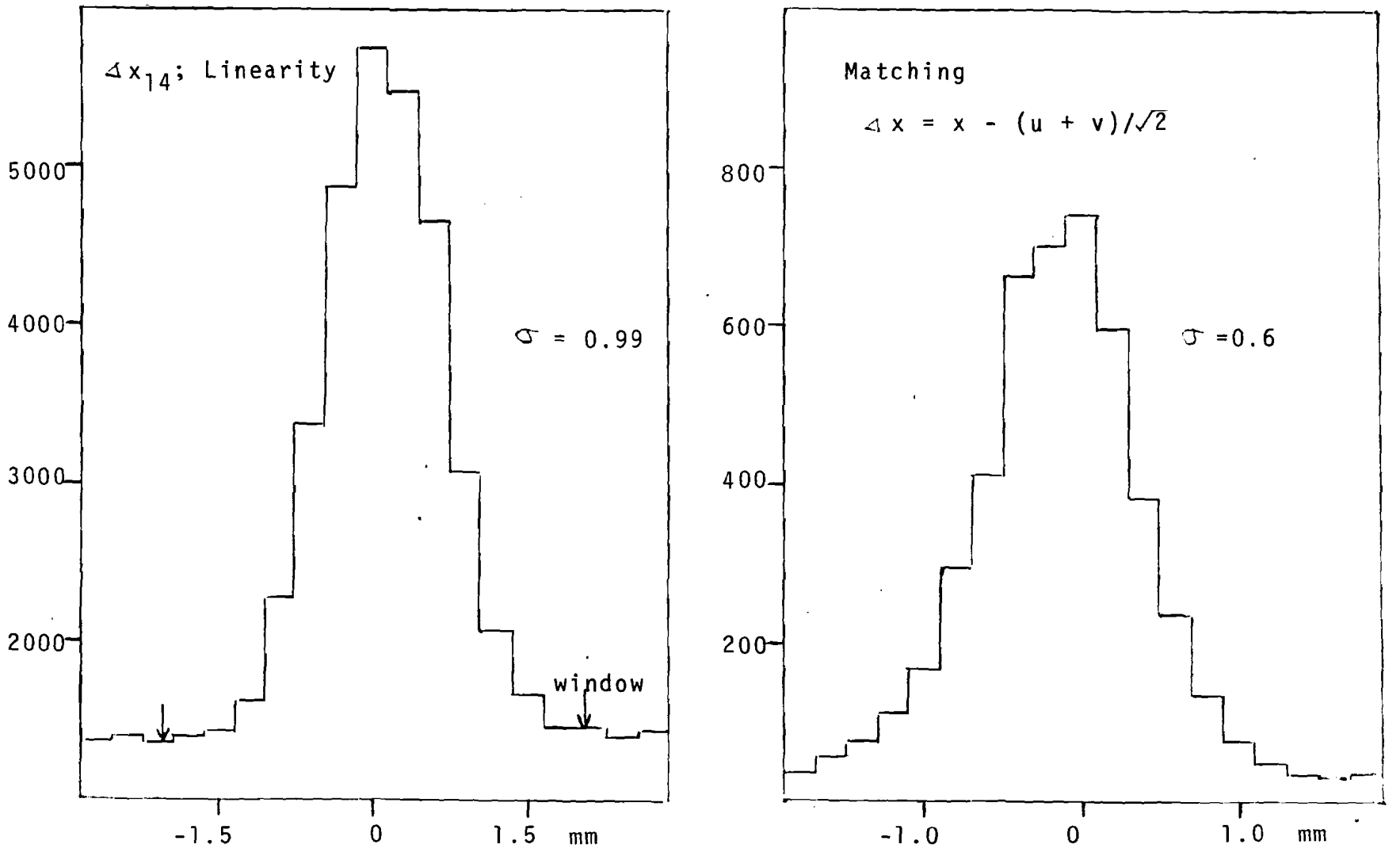

Figure B.2

WINDOW FOR POINT FINDING IN MIDDLE OF SPECTROMETER

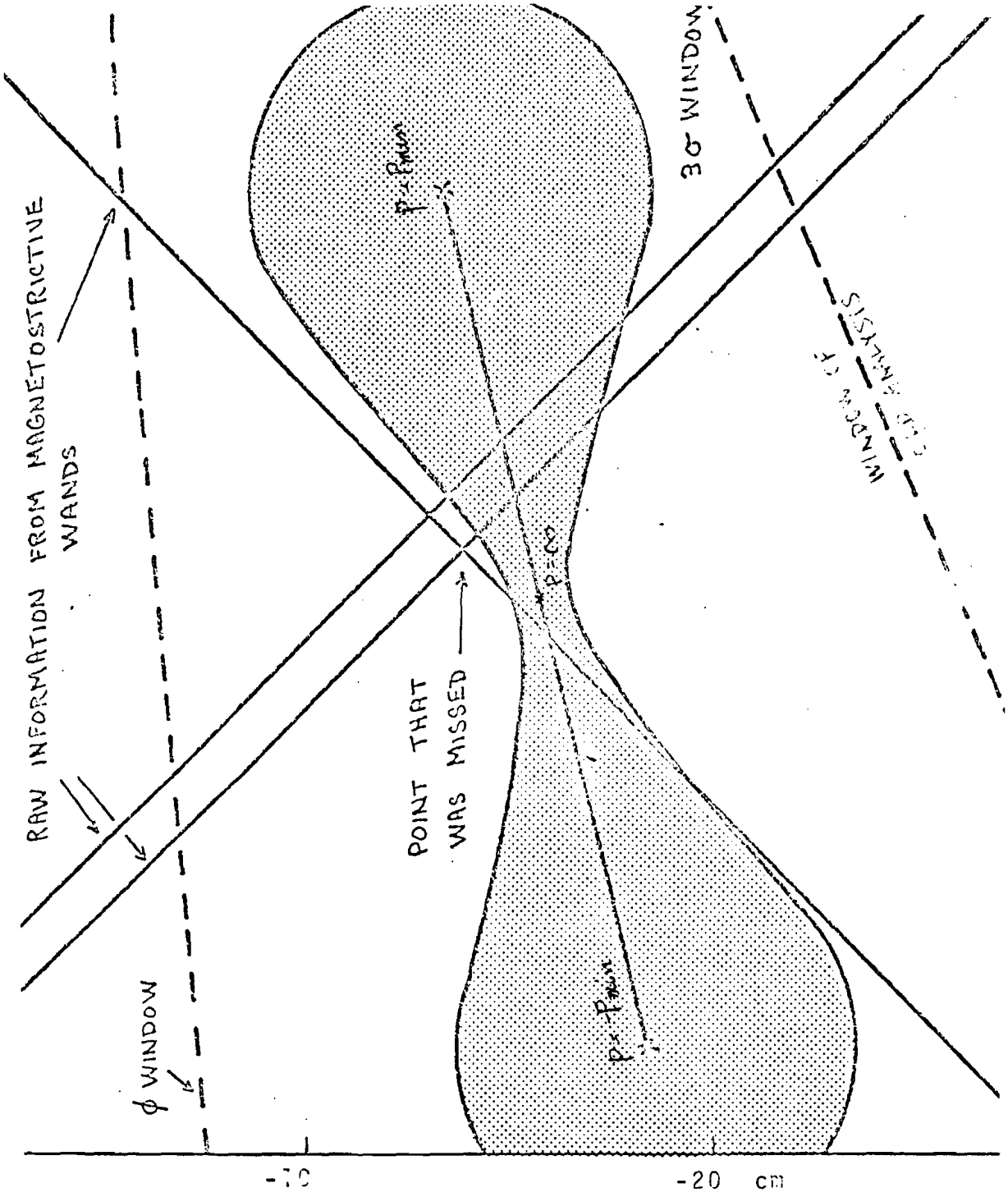

restrict the region. The best combination of points in 11 and 12 was chosen by minimizing the χ^2 defined below.

$$\chi^2 = \sum_{i=11,12} (d^{-1}(K))_{ij}(\delta x_i \delta x_j + \delta y_i \delta y_j)$$

where δx_i are residuals from the predicted as Eq. (B.2) and d(K) is the error matrix given by

$$d(K)_{ij} = \sum_{m=magnets} Z_{im} Z_{jm} \langle\theta^2\rangle + \delta_{ij}(\sigma_e^2 + \sigma_m^2)$$

$\langle\theta^2\rangle$ is the mean square multiple scattering angle from one iron magnet, σ_e^2 and σ_m^2 are the extrapolation and measurement errors, and Z_{im} is the distance between the ith module and the center of the mth magnet in the downstream.

Typical χ^2 as a function of K is shown in Figure B.3. The minimization of χ^2 is done by approximating the shape around the minimum by the second order polynomial.

3) Tracks

Lines that found one or both points in modules 11 and 12 are called tracks, although in the final analysis both points were required. The quality of tracks was ordered in terms of the number of contributing modules (4 or 5), the χ^2 obtained above, and the number of DCR confirming points (up to 3, see Table B.1).

Each track up to five was fitted by a momentum fitting program, and was written on to the secondary tape independent

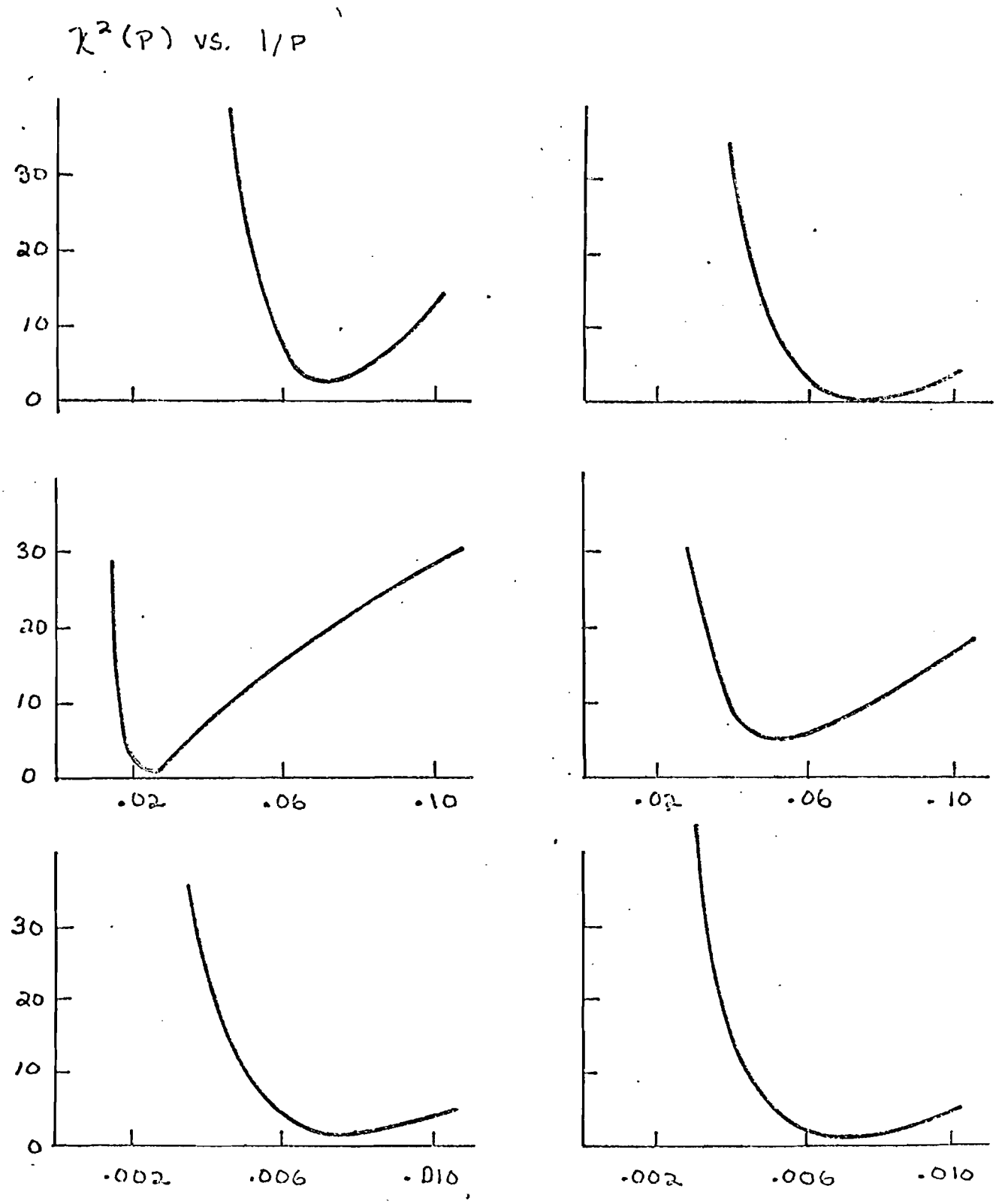

Figure B.3

SAMPLE MINIMIZATION OF ONE-DIMENSIONAL χ^2 VS. $1/P$

of linking to the target.

4) Hourglass Window

The analytic realization of the window used in the analysis is described below. The method is based on the following observations:

i) The trajectory produced at a module by changing the momentum is close to a straight line.

ii) The distance on the trajectory from $P = \infty$ point is almost proportional to $1/p$ (Figure B.4).

iii) The momentum independent part of the window size is the same for all the lines.

Choosing the coordinates such that $P = \infty$ point is the origin and $P = P_{min}$ is on the x axis, an observed point (x_o, y_o) is thought to be within the window if the solutions for x exist in the equation,

$$(x_o - x)^2 + y_o^{\ 2} = \sigma^2 \cdot (r_e^{\ 2} + r_m^{\ 2}(x/x_{max})^2)$$

where x is a point on the x axis, $\pm x_{max}$ are the endpoints corresponding to $P = \pm P_{min}$, r_m is the rms multiple scattering radius at $P = P_{min}$, r_e is the rms radius due to extrapolation error, and σ^2 is to control the window size.

Unfortunately, it was realized after some production analysis that the equation does not have solutions if σ^2 was made too large. The efficiency vs. σ^2 was studied in detail as discussed in Appendix C and, fortunately, the chosen value was found to be efficient.

Figure B.4

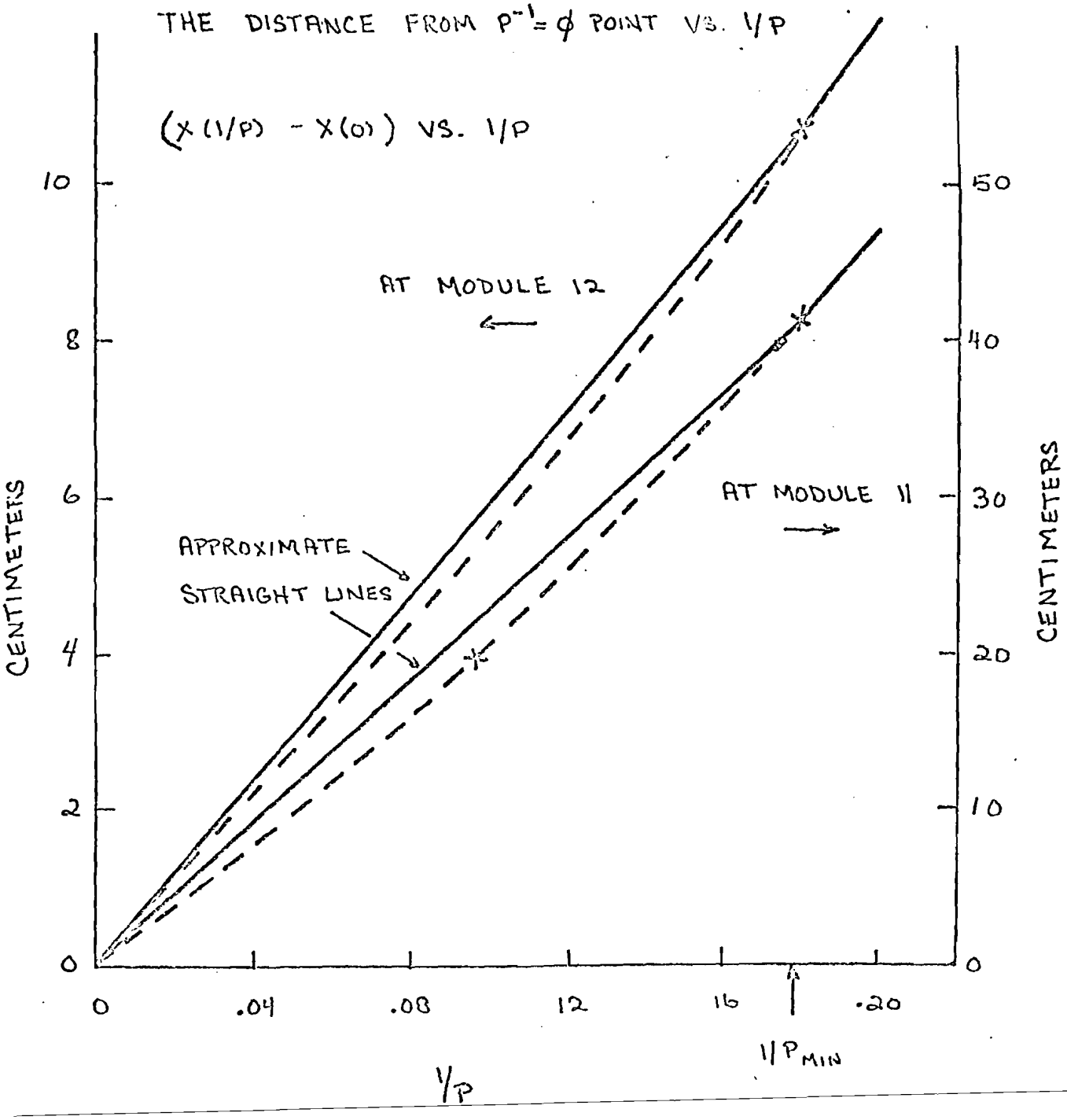
THE DISTANCE FROM $P^{-1} = \phi$ POINT VS. 1/P
(X(1/P) - X(0)) VS. 1/P
AT MODULE 12
AT MODULE 11
APPROXIMATE
STRAIGHT LINES
CENTIMETERS
CENTIMETERS
0
2
4
6
8
10
0
10
20
30
40
50
0
.04
.08
12
16
.20
1/P
1/P MIN

2. Beam Track Finding

The beam chamber consisted of three proportional chamber modules #2, 3 and 4. They were XY and two UVW chambers, respectively. Every wire of these chambers was latched in, and the first task was to decode the fired bits to give the wire coordinates. Then straight lines were sought in three modules.

The chamber operation was not always stable. During some runs the amplifiers were marginally efficient. Thus a slightly more elaborate scheme than the original was developed as described below.

1). Fired bits to wire coordinates

Fired bits were converted to the coordinates in the chamber. Special attention was given to multiple wires. Wires firing more than two adjacent were eliminated. Two wires adjacent were averaged.

2). Spatial coordinates

In each module xy coordinates were listed correlating the chambers of the module. In the UVW modules, signals satisfy the following equation,

$$|u + v + w| < W_M$$

where u, v and w are the wire coordinates in each chamber and W_M is the appropriate window.

Every fired wire in UVW chambers was tested against this. The histogram of this is shown in Figure B.5. The

ones that satisfy the equation were called match of 3. The wires contributed to match of 3 were erased to find match of 2, but they were restored in the end for the reasons described below. These matched wires were converted to the spatial coordinates. Up to 30 xy coordinates were listed at each module.

3). Beam tracks

The xy coordinates at the three modules were fitted to a straight line to reconstruct beam tracks.

The following criteria were adopted for beam tracks. They were to increase the reconstruction efficiency which was necessary for some of the runs but at the same time not to pick up noise.

1 At least one degree of freedom in the fit

2 χ^2/freedom < 10

3 The beam angle less than 2.5 milliradian

The types of the beam reconstructed were (2,2,2), (1,2,2), (2,1,2) and (2,2,1) where the numbers represent the number of coordinates at each module contributing to the fit. Although it was not totally desirable, the first two types were sought first and the rest were tried only when that failed to give a beam track.

Reconstruction of the last two types required a rotation of the coordinates to the plane of the constraint. To pick up these types of tracks, restoration of wires after match

of 3 was necessary. The coefficients were rotated back if the above criteria were satisfied.

The χ^2 distribution is shown in Figure B.5b. The cut seems to be adequate. Table B.2 summarizes the quality of beam tracks reconstructed comparing event and beam triggers which are in principle similar.

Figure B.5$_a$ Matching of UVW histogram of every (u+v+w)

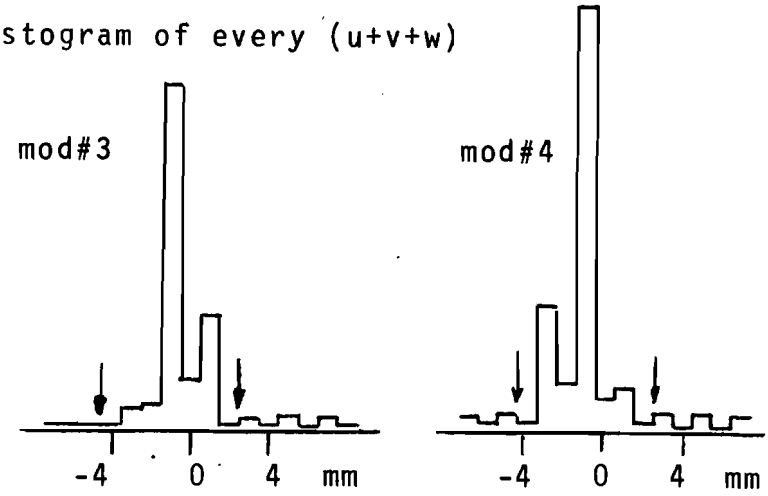

Figure B.5b χ^2_B distribution

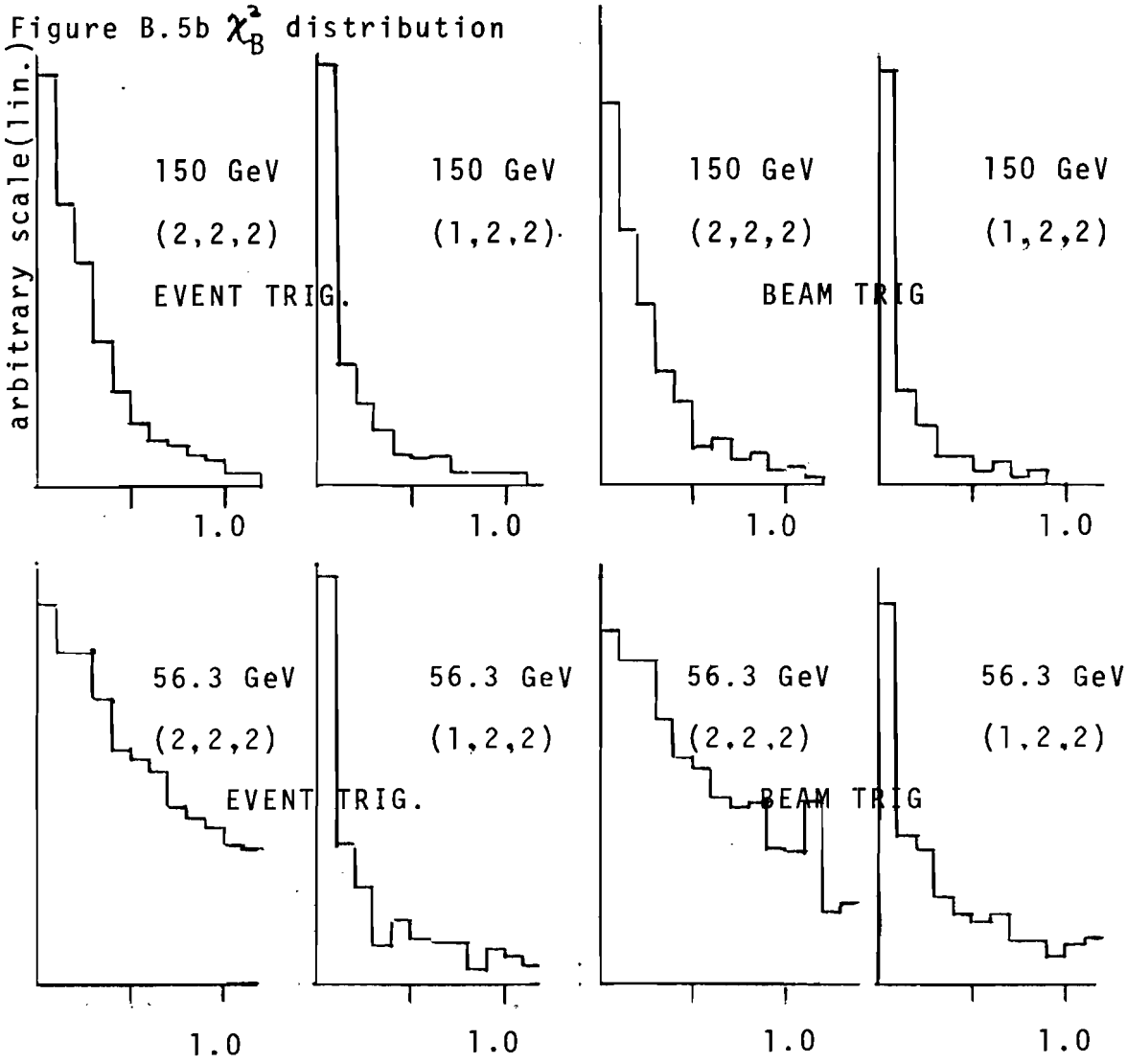

Table B.2. Beam Track Reconstruction

1. Number of beam tracks/trigger

	Number of beam tracks				
	0	1	2	3	>3
150 GeV LA					
Event trigger	4.3%	87.4	7.0	0.9	0.4
Beam trigger	0.7	89.5	8.6	0.8	0.3
56.3 GeV LA					
Event trigger	2.9%	92.9	3.7	0.3	0.2
Beam trigger	0.4	95.4	4.0	0.2	0

2. Type of the beam track

	No. of coordinates contributing at each module		
	222	122	212 or 221
150 GeV LA			
Event trigger	72.1%	21.6%	6.3%
Beam trigger	83.6%	13.5%	5.0%
56.3 GeV LA			
Event trigger	86.1%	10.8%	3.1%
Beam trigger	88.4%	9.2%	2.3%

3. Momentum Fit

1) χ^2 and its minimization

The resolution of the reconstructed momentum is dominated by the multiple scattering in the iron magnets, and the deviations at the spark chambers from an ideal track are correlated.

Thus, it is important to define a χ^2 taking the effect into account in order to obtain the optimum resolution.

The χ^2 was defined as follows:

$$\chi^2 = \sum_{ij} (Y^{-1})_{ij}(\delta x_i \delta x_j + \delta y_i \delta y_j)$$

where δx_i, δy_j are the residuals at the ith module and Y_{ij} is the expectation value of $\delta x_i \delta x_j$, and

$$Y_{ij} = \langle \delta x_i \delta x_j \rangle = \langle \theta^2 \rangle \sum_m \left(Z_{im} Z_{jm} + \sigma_m^2 \delta_{ij} \right)$$

$\langle \theta^2 \rangle$ is the mean square multiple scattering angle from one iron magnet, σ_m^2 is the mean square of measurement error, and Z_{im} is the distance between the module i and the center of mth magnet in the upstream.

With this definition, $\langle \chi^2 \rangle$, the expectation value of χ^2 should be the number of degrees of freedom.

The predicted points (and hence χ^2), are functions of the momentum, and the initial angle and the position. Strictly speaking, the minimization of the χ^2 by varying them can be complicated, but it was simplified by expanding the trajectory in powers of 1/p, retaining up to the second

order. This is discussed in the next section.

So the procedure for χ^2 minimization is to predict a trajectory from an initial guess, obtain Y_{ij} by inverting the matrix, minimize χ^2 and iterate this.

2) Tracing through the spectrometer

The ideal track can be predicted if the initial position and the slope are given, by successively calculating new positions and slopes as z, the distance along the beam direction, is stepped through the spectrometer.

At some fixed z, the position and the slope were expanded in terms of the curvature up to the second order.

$$x = \sum_{i=0}^{2} x^{(i)} K^i$$

$$x' = \sum_{i=0}^{2} x'^{(i)} K^i$$

(similar formula for y, y')

where x' is dx/dz, the tangent of the track in x-z plane, K is the curvature and related to the momentum p by

$$K = (q \cdot B_0/3327.4)/p$$

B_0 is the typical fixed field strength, q is the charge of the particle (μ^+ or μ^-) and the number is the conversion coefficient.

In free space where no force is present, the equations at some $Z = Z_2$ given the values at $Z = Z_1$ are expressed as

$$x(Z_2) = x(Z_1) + x'(Z_1)*(Z_2-Z_1)$$
$$y(Z_2) = y(Z_1) + x'(Z_1)*(Z_2-Z_1)$$

The bend in a magnet is simplified by an impulse approximation, in which the deflection occurs at the center of the magnet.

$$\Delta x'_{bend} = -f_y(r)*K*T = -f(r)\ \sin\phi*K*T$$
$$\Delta y'_{bend} = f_x(r)*K*T = f(r)\ \cos\phi*K*T$$

where $f_y(r)$ is the y component of the magnetic field at radius r, ϕ is the angle in xy plane, and T is the thickness of the magnet.

By expanding the equation in terms of K, the new coefficients are obtained.

$$x'^{(1)} = x'^{(1)} + T\cdot f(r_o)\sin\phi_o$$
$$x'^{(2)} = x'^{(2)} + q\ T(f'(r_o)\sin\phi_o\cdot r + f(r_o)\cdot(\sin\phi_1 + (n-\tfrac{1}{2})DE))$$

(for y replace sin → cos)

where r_o, r_1, $\sin\phi_o$, $\sin\phi_1$, etc., are given by

$$r_o = (x^{(0)2} + y^{(0)2})^{1/2}$$
$$r_1 = (x^{(0)}\cdot x^{(1)} + y^{(0)}\cdot y^{(1)})/r_o$$
$$\cos\phi_o = x^{(0)}/r_o$$
$$\sin\phi_o = y^{(0)}/r_o$$
$$\cos\phi_1 = y'^{(1)}/r_o - y'^{(0)}\cdot r_1/r_o^{\ 2}$$
$$\sin\phi_1 = x'^{(1)}/r_o - x'^{(0)}\cdot r_1/r_o^{\ 2}$$

DE is related to the energy loss ΔE, and n is the number of magnets passed so far.

$$DE = 3327.4 \cdot \Delta E / qB_0$$

ΔE has a small dependence on the momentum, which was fitted to the following form,

$$E = 0.01264/p^2 - 0.011406/p + 0.016 + 0.53589 \times 10^{-4}\ P + 0.29748 \times 10^{-8}\ P^2$$

Appendix C

STUDY OF TRACK RECONSTRUCTION EFFICIENCY AND THE BIAS

The efficiency and bias of track finding in the analysis program was studied in detail, reanalyzing the raw data to estimate the normalization and systematic biases.

This was done in two steps utilizing the structure of the analysis program which was described in Appendix B. The first step was to estimate the efficiency of line finding in the rear of the spectrometer, and the second step that for point finding given a line in the rear.

The uniformity of the efficiency over spark chamber planes was studied by dividing module #13 into sixteen regions as shown in Figure C.1.

The inefficiencies studied here are due to the following origins:

a. Inefficiency of individual spark chambers.

b. Too many sparks in some of the chambers due to local breakdown or electromagnetic showers associated with the muon track.

c. The scattering or energy loss too large in the iron magnets to be within the windows of the analysis program.

d. Breakdown of some approximations in the program or failure of fitting.

Figure G.1

Binning of the spark chamber plane #13

and the numbering

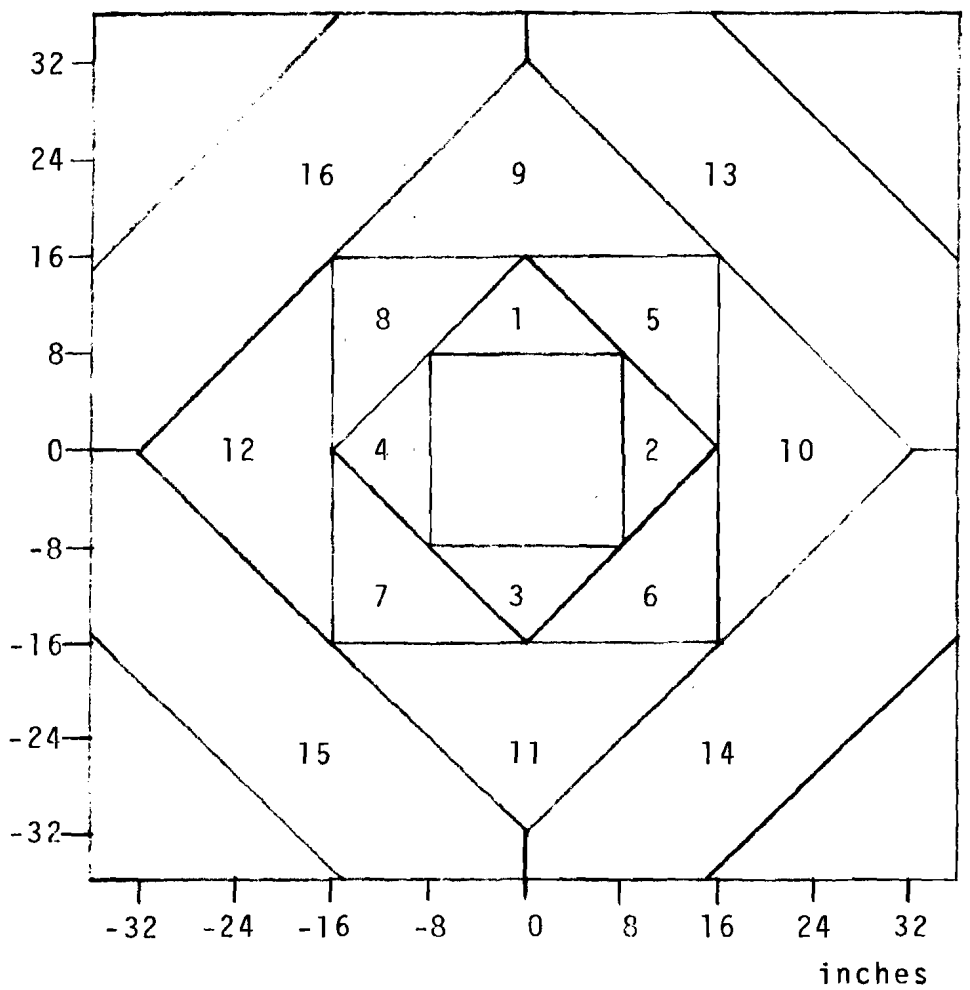

There are other effects related but that cannot be studied in this section:

a. Trigger bias: inefficiency of trigger counters or electronics, and accidental killing due to the veto counters especially due to beam veto counters.

b. Overall inefficiency of spark chambers, e.g. inefficiency of thyratron, bad spill, etc.

The two steps are described below.

1. Back line efficiency

Having a reasonable monitor is essential for efficiency study.

Usual analysis first found lines in the rear three modules, and then found points in the chambers upstream. If we go downstream instead and find tracks in front, we have a good monitor for the back line finding.

It was even possible to use existing software with minor modification by renaming the module numbers and negating the Z-coordinates.

Monitor tracks were reconstructed by finding lines in the modules #8, 9 and 10 then seeking points in #11 and 12 by extrapolating the lines.

The reconstructed tracks were fitted to get the momentum and the angle. We call this FRONT FIT. The information of the FRONT FIT was written on tape in the same format as the secondary tape, together with the raw coordinates of the last

three modules.

The tape created was read by a special program, which made appropriate cuts to the sample and called relevant line finding programs a number of times with different window sizes each time.

A line was considered to be reconstructed if it was within a 5σ cone around the predicted line from FRONT FIT. The size of the cone was mainly determined by the multiple scattering in the upstream magnets, and was empirically adjusted to have a proper momentum dependence by analyzing calibration data. The separation of the signal was very clean.

As mentioned in Appendix B, the front chambers were often flooded with many sparks. So the efficiency of reconstructing FRONT TRACKS was low (about 20% per trigger) and halo tracks were used to obtain sufficient statistics at large radius.

Event reconstruction efficiency was obtained by cutting on Z_{int} around the target. The cut on the distance at the closest approach was also important to eliminate accidental matching of event track in one view with halo track in the other.

2. Point finding efficiency

Given a back line, the efficiency of point finding in modules 11 and 12 was studied.

Back lines were selected assuming that they were from

the target, and the momentum and angle were determined. We call this LINE FIT.

Contamination from halo tracks and events from absorbers could be greatly reduced by applying cuts discussed below.

The momentum and the angle for a given back line were determined as follows. Using the back-tracing subroutine, a point was predicted as a function of momentum in the xy plane at the target position.

Given the point (x_B, y_B) at which the beam track went through the plane, a χ^2 was minimized to obtain the momentum.

$$\chi^2(K) = \{(x(K) - x_B)^2 + (y(K) - y_B)^2\}/(\chi^2_{mult} \cdot K^2)$$

where $K \propto 1/E'$, $(x(K), y(K))$ is the predicted point, and the denominator is the mean square radius of the multiple scattering in the spectrometer. Momentum independent terms from the measurement error and the extrapolation error were neglected. The reconstructed momentum compared to the BACKFIT made a gaussian of mean = 1.0 and sigma about 10%.

The following cuts were made to reduce contamination of lines that were not from the targets:

a) Event trigger

b) One and only one beam track

c) No unscattered muon downstream. This eliminated about 40% of the triggers, but events from downstream were greatly suppressed.

d) E' (LINE FIT) > $E_0/3$

e) χ^2 (LINE FIT) < 10

f) DCR confirmation. This eliminated events other than from the target in two reasons. Out of time nature of halo track, and the predicted trajectory is wrong for those events.

g) Geometry: standard cuts using the predicted coordinates.

For lines passing the cuts, the hourglass window σ was plateaued by feeding the same line to the relevant programs a number of times with different σ each time. All five points were required and usual momentum fit (BACKFIT) was done to require that χ^2 (BACKFIT)/dof < 10.

3) <u>The results</u>

The uniformity of efficiency over a spark chamber plane is shown in Figure C.2 for line finding and for point finding.

The efficiency of halo tracks only for line finding is shown to study the uniformity out to large radius in good statistics. The lower efficiency for them is because of out of time nature of halo tracks.

Figure C.3 shows the efficiencies vs. radius.

We conclude from these that the chambers were uniformly efficient.

Overall efficiency is given in Table C.1. The errors for line finding efficiency were estimated by displaying tracks and line finding on a scope.

Those errors for point finding were estimated from the dispersion around the mean.

These numbers were used to estimate the effective number of muons to each set of data.

Figure C.2 Uniformity of efficiency over a spark chamber plane

ε_L = line finding eff.

ε_p = point finding eff.

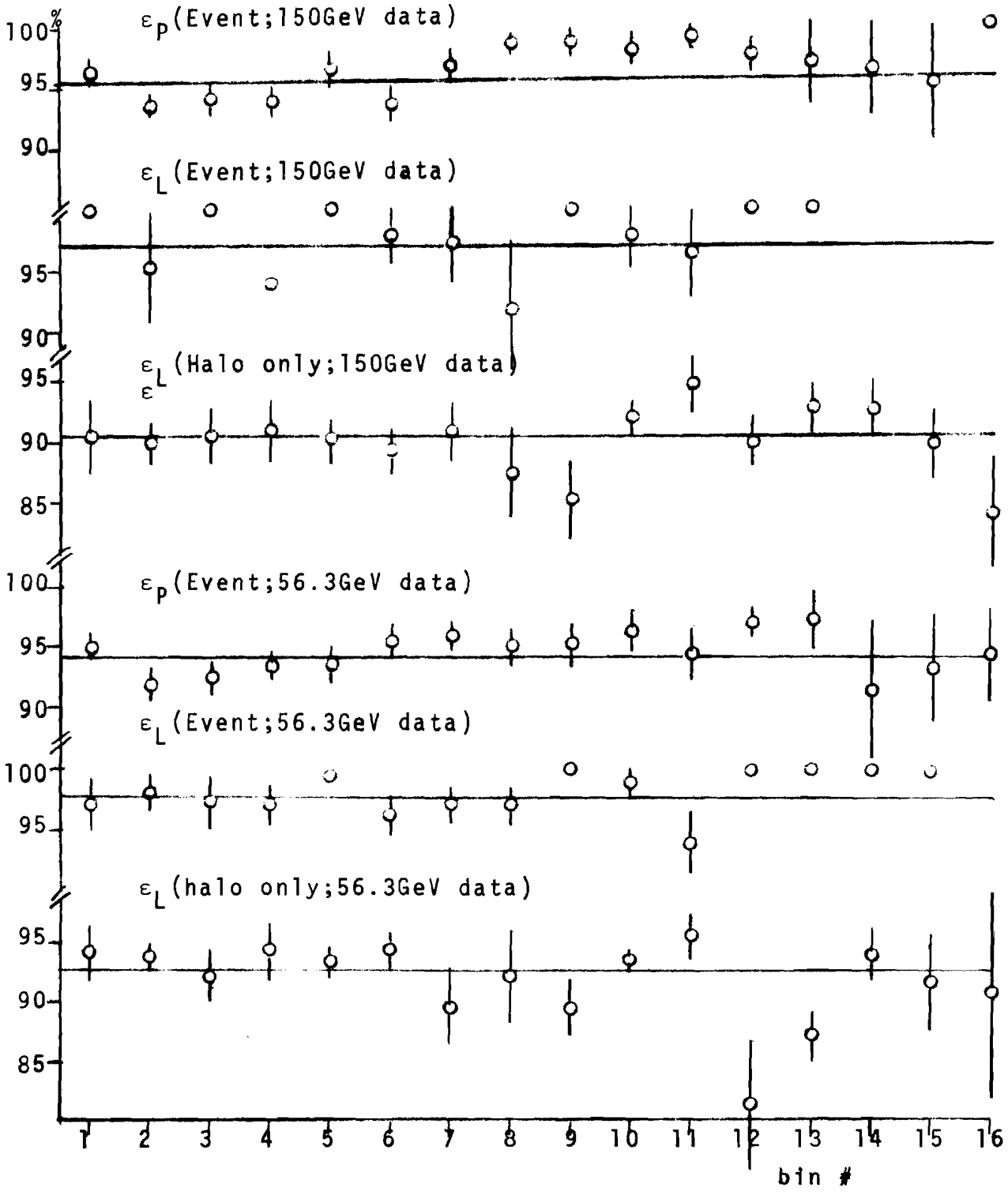

Figure C.3 Reconstruction efficiency vs. R_{13}

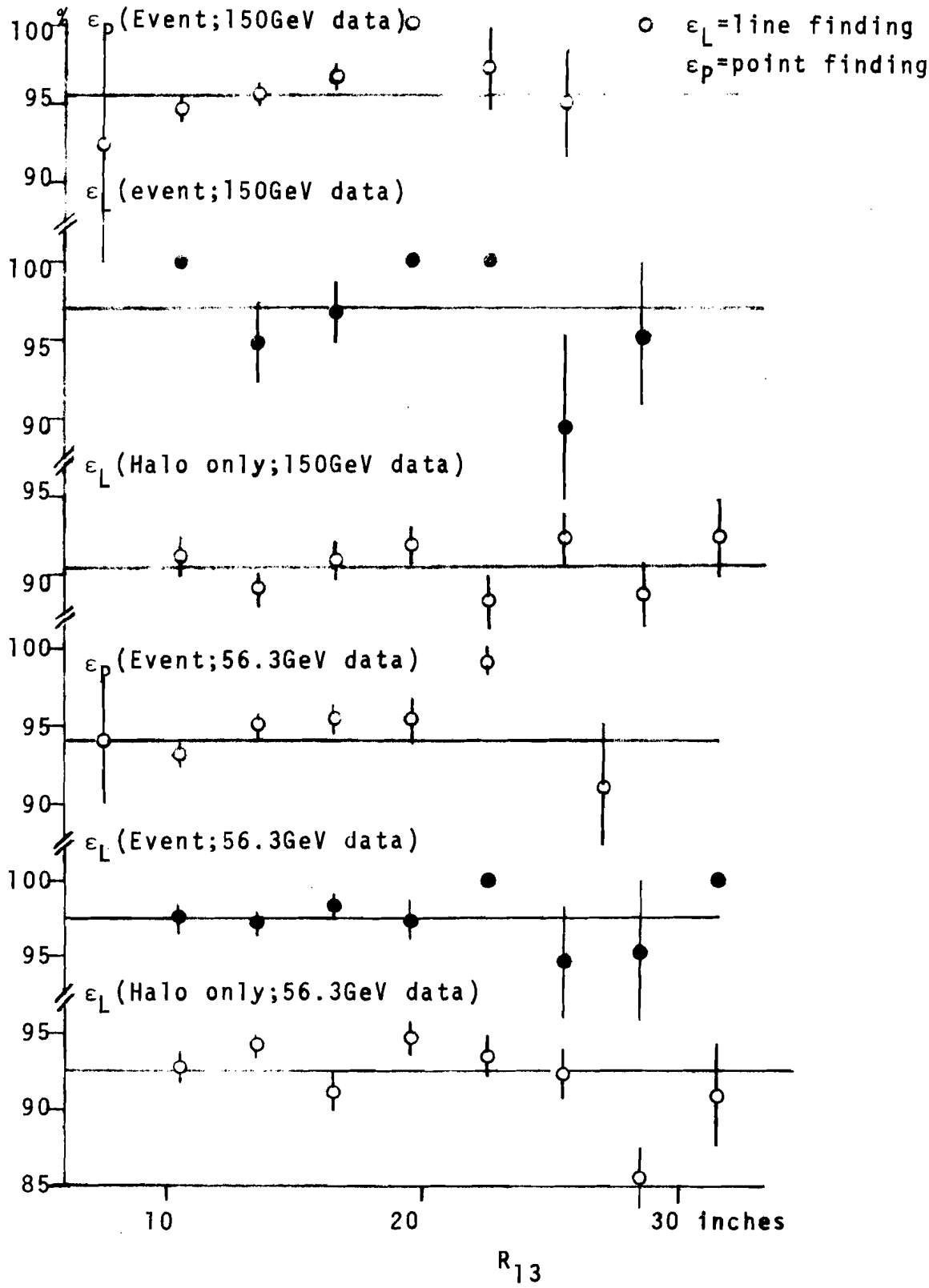

Table C.1. Track Finding Efficiency

Data set	Back line finding	Point finding	Overall
150 GeV LA	96.9 ± 2%	95.6 ± 2%	92.6 ± 3.0%
56.3 GeV LA	97.6 ± 2%	95.8 ± 2%	92.1 ± 3.0%
150 GeV SA	91.6 ± 2%	96.5 ± 2%	88.4 ± 3.0%
56.3 GeV SA	97.3 ± 2%	96.1 ± 2%	93.5 ± 3.0%

Appendix D

CALIBRATION OF THE SPECTROMETER

1. Method

In order to calibrate the spectrometer, the muon beam line was tuned to various momenta and muons of known energy were sent into the spectrometer with the help of specially constructed small toroidal magnet placed around the target position. The small magnet was 2" ID, 12" OD, and 73" long iron, excited applying 85 A to obtain the transverse momentum of about 1 GeV/c. It was placed at several positions along the beam line to illuminate different regions of the spectrometer at lower energies.

The conditions of these runs is summarized in Table D.1.

The data were analyzed by the analysis program as though they were real data, and the secondary tape was analyzed by a special program to cut and histogram events. Note that we are calibrating BACKFIT, which was used as the final analysis.

2. Beam energy into the spectrometer

The determination of beam energy into the spectrometer at 1% level needed a careful investigation. In principle the energy was determined by extrapolating the beam tracks through bending magnets in Enclosure 104 and then to the downstream of Enclosure 103 where a beam hodoscope HA was placed.

Table D.1. Conditions of Calibration Runs

150 GeV configuration

Run #	1E4 setting	E' into the spectrometer	No. of triggers	P_T of small magnet	Note
4467	148.3 GeV	144.3 GeV	1000	1.0 GeV/c	
4468	92.8	89.1	1220	1.0	no beam tracks available
4471	55.2	51.8	1600	1.0	
4472	34.6	31.4	2000	0.3	

56.3 GeV configuration

Run #	1E4 setting	E' into the spectrometer	No. of triggers	P_T of small magnet	Note
564	56.1 GeV	52.2 GeV	6000	1.0 GeV/c	
565	46.7	43.2	6000	1.0	
566	35.1	31.8	6000	1.0	CEA quads off.
567	35.1	31.8	6000	0.3	
568	31.8	31.8	6000	0.7	
569	21.5	18.5	6000	0.7	
575	99.6	97.0	13000	1.0	

The difference between the latched bit and the extrapolation is the momentum dispersion. This does not give the absolute energy if the position of HA and/or beam proportional chambers is not precisely known.

Uncertainty of 1 cm of HA or module #4 corresponds to 0.5% of energy uncertainty.

The beam energy into the spectrometer was also estimated from 1W2 magnet setting assuming that the beam was centered at the aperture of magnets upstream and using HA bits.

These results agree within 2%.

The values in Table D.1 are average of these two methods, subtracting the mean energy loss through the small magnet.

3. Results and discussion

As the resolution of momentum is dominated by the multiple scattering in the spectrometer, the inverse of momentum 1/E' is gaussian, which produces asymmetry toward higher energy if plotted in terms of the momentum. A typical distribution is shown in Figure D.1. The mean and the sigma of the gaussian in 1/E' obtained are summarized in Table D.2.

The difference in the resolution for two configurations is because BACKFIT did not really scale. In comparing two sets of data, a gaussian error of 8% was folded into 1/E' of 150 GeV data.

The calibration of higher energies for 150 GeV configuration was difficult because of limited bend angle

Figure D.1 E' Resolution

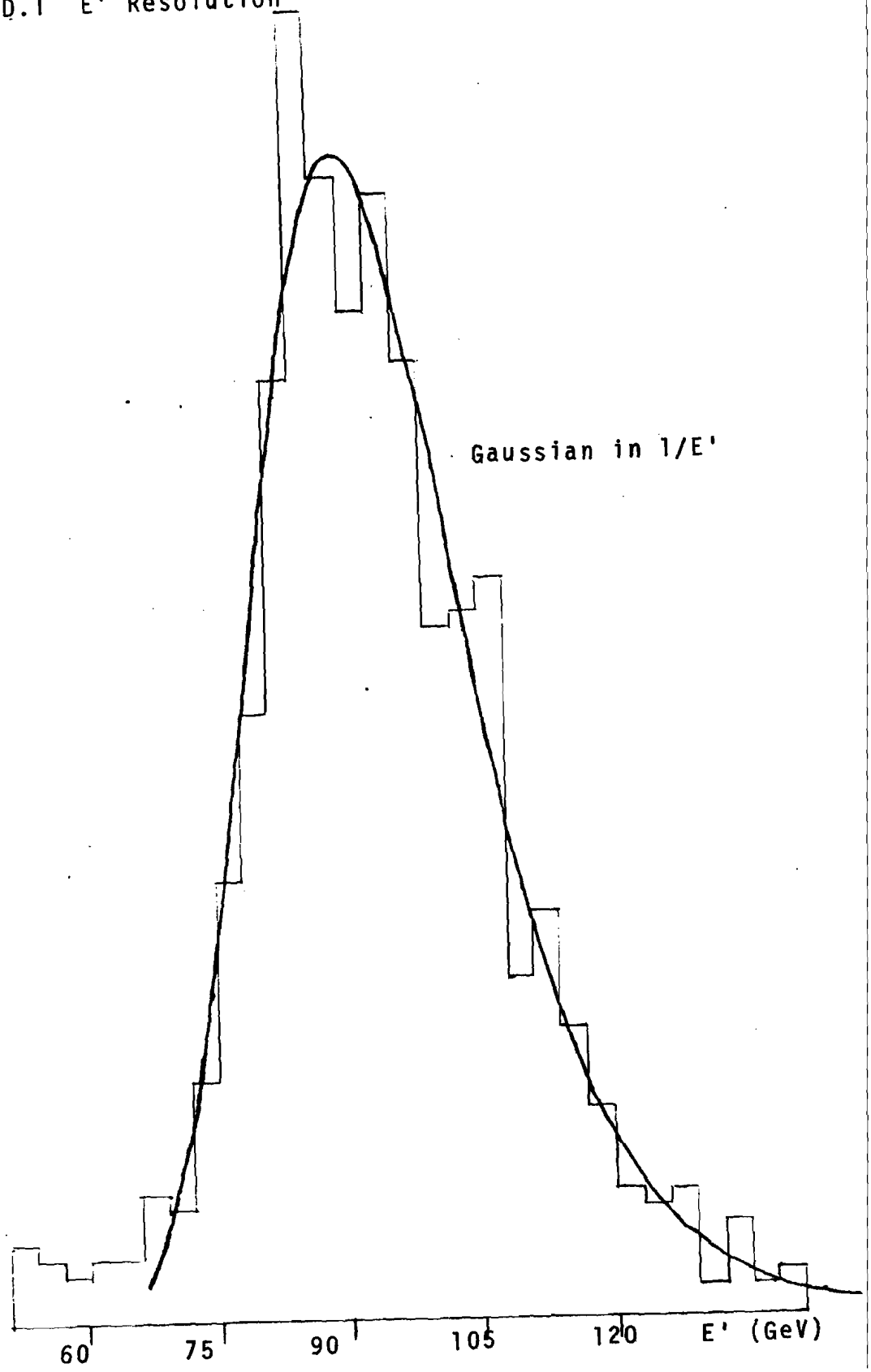

obtained by the small magnet. The deflected beam went very close to the inside edge of acceptance, and the energy might have been biased. We assume that the calibration there is similar to the one at lower energies, and assign ±1.0% error for 150 GeV configuration. The error for 56.3 GeV configuration is ±0.3%.

Table D.2. Result of Calibration (BACKFIT)

Run #	E' predicted (E'_p)	Reconstructed $\langle 1/E' \rangle^{-1}$	σ	$\langle 1/E' \rangle^{-1}/E'_p - 1$
150 GeV Configuration				
4467	144.3 GeV	146.6±1.9	14%	+1.2%
4468	89.1	89.8±0.5	14	+0.8
4471	51.8	51.8±0.2	14	-0.0
4472	31.4	30.2±0.2	14	-4.0
56 GeV Configuration				
564	52.2 GeV	51.9±0.15	17%	-0.60%
565	43.2	42.9±0.12	17	-0.67
566	31.8	31.8±0.10	17	-0.01
567	31.8	31.8±0.1	17	-0.00
568	31.8	31.6±0.1	16	-0.66
569	18.5	18.1±0.05	16	-0.19
575	97.0	97.0±0.4	18	+0.05

Appendix E

EVENT SIMULATION: MONTE CARLO PROGRAM

A Monte Carlo program was developed to simulate the data to study various systematic effects. The program developed at Cornell is described in detail, although two other independent programs existed.

It was found convenient to separate the program into two parts. The first part generated and wrote out events according to a cross section, taking the straggling and multiple scattering in the target into account. The second part read the generated events in, propagated through the spectrometer, made the fits as done in data analysis and wrote tape.

This separation had the following advantages:

1) It was easier to study various systematic effects, e.g. a question of how well apparatus scales for the two configurations, for the different beam sizes, etc.
2) It allowed increasing core size to speed up generation.
3) It gave a way of obtaining the acceptance.
4) Checks of the program were decoupled.

The brief description of the program is given below.

1. <u>The generation part</u>

Generation of events used a look-up table to increase speed.

Given a cross section $d^2\sigma/dudv$, where $u = \ln(E_0-E')$ and

$v = 1/\theta^2$, the following tables were prepared:

$$F(u_i) = \int_{u_{min}}^{u_i} du \int_{v_{min}}^{v_{max}} dv \; \frac{d^2\sigma}{dudv} \Big/ \int_{u_{min}}^{u_{max}} du \int_{v_{min}}^{v_{max}} dv \; \frac{d^2\sigma}{dudv}$$

and

$$G(u_i) = \text{maximum of } \frac{d^2\sigma}{dudv} \text{ for } v_{min} < v < v_{max} \text{ and}$$

$$u_i < u < u_i + \Delta u$$

(u_i: 512 steps for 5 different E_0)

Picking the vertex position randomly, the incident muon was made straggle to the vertex. At the closest E_0 for which the tables were prepared, u was generated according to F(u), then picked v if a random number is smaller than $(d^2\sigma/dudv)/G(u)$.

The resulting E',θ and the weight of the event were rescaled to the original E_0 at the vertex utilizing the approximate scaling nature of the cross section. The non-scaling of the cross section was corrected in the weight.

The scattered muon thus generated was straggled and multiple scattered in the rest of the target.

Fermi motion of the nucleon could be included by choosing the nucleon momentum, and by generating events in the nucleon rest system.

The weight was made unity by throwing a random number to drop or to repeat the event.

The information written on tape is given in Table E.1.

2. The spectrometer part

Reading in the tape of generated events, the muons were propagated through the spectrometer. The coordinates were fitted in the same way as the data analysis and the information was written on tape.

This part could also run in point mode where events with fixed E' and θ were sent to the spectrometer.

Actual beam tracks obtained from the beam triggers could also be read in.

Radiative corrections and background contributions were taken into account after events were accepted, because they did not change kinematical values except for the weight of the events.

Bending, straggling and multiple scattering in the spectrometer magnets were evaluated at every 1/3 of the magnet thickness. The bend was exerted using a simple impulse approximation. The step size was studied and found to be satisfactory. Coordinates were evaluated at spark chambers and trigger counters. Events were rejected if they were outside of active region of trigger counters.

3. Ingredients

Table E.2 summarizes various physics effects included in the program.

Table E.1. Format of Generated Events

10 words/event

90 events/block

Word #	Information	
1	RUN * 10 + EV	
2	E_0	Nuclear rest frame
3	E'	
4	θ	
5	E'	at the vertex in the lab frame
6	θ	
7	z at the vertex	
8	# muons in modulo 2^{24}	
9	E'	after the target
10	θ	

Units: MeV, 0.1 mrad and 0.1 mm

Table E.2. Effects Included in the Monte Carlo Program

$\nu W_2(x')$	Bodek's fit to deuteron and proton[31] $\nu W_2^{iron} = (N\nu W_2^{deuteron} - (N-Z)\nu W_2^{proton})/A$ $\nu W_2(x') = \sum_{i=3}^{7} a_i(1-x')^i$, $x' = Q^2/(2M\nu + M^2)$ For deuteron: $a_3 = 1.638$, $a_4 = -3.584$, $a_5 = 15.61$, $a_6 = -22.28$, $a_7 = 9.192$ For proton: $a_3 = 0.5435$, $a_4 = 1.714$, $a_5 = 0.6723$, $a_6 = -5.971$, $a_7 = 3.313$
$R = \sigma_L/\sigma_T$	Fixed at $R = 0.18$
Multiple scattering	Gaussian of mean square angle $\langle\theta^2\rangle_{proj} = (0.015/P)^2 \cdot$ rad. lengths
Energy loss	μe scattering, bremsstrahlung, pair creation and nuclear interaction. Made lookup table approximating the combined shape.
Fermi motion	Simple Fermi gas model with the maximum momentum of 260 MeV. Lorentz transform to the nucleon rest frame and transform back.
Radiative corrections	Equivalent radiator method. (Y. S. Tsai and also G. Grammer)[30]
Backgrounds	Wide angle bremsstrahlung

νW_2 for iron was obtained from Bodek's fit for deuterons and protons. Figure E.1 shows the resulting function plotted vs. ω. The x' instead of x as the scaling variable shows the apparent Q^2 dependence as shown.

$R = \sigma_L/\sigma_T$ was fixed at 0.18. The effect of a small change around this value is negligible.

Ignoring single scattering tail in multiple scattering is justified for thicknesses exceeding about 10 radiation lengths. The argument is that at the region where the single scattering becomes important, the momentum transfer is large enough to be dumped by the nuclear form factor.

The simple Fermi gas model could be too naive, but the effect is itself unimportant according to the study in Appendix F.

Radiative corrections used a simple equivalent radiator method, where the internal bremsstrahlung was approximated by a real bremsstrahlung placing a radiator of thickness $t = \frac{4\alpha}{3\pi}(\ln(Q^2/m_\mu^2) - 1)$ in radiation length before and after the scattering. This procedure was checked to agree within 2% with the exact integration given in Mo and Tsai.

Importance of background due to wide angle bremsstrahlung (WAB) was pointed out by D. Yennie, who derived a simple form for the contribution as the ratio to the deep inelastic cross section (DI).

Figure E.1 νW_2^{IRON} vs. ω

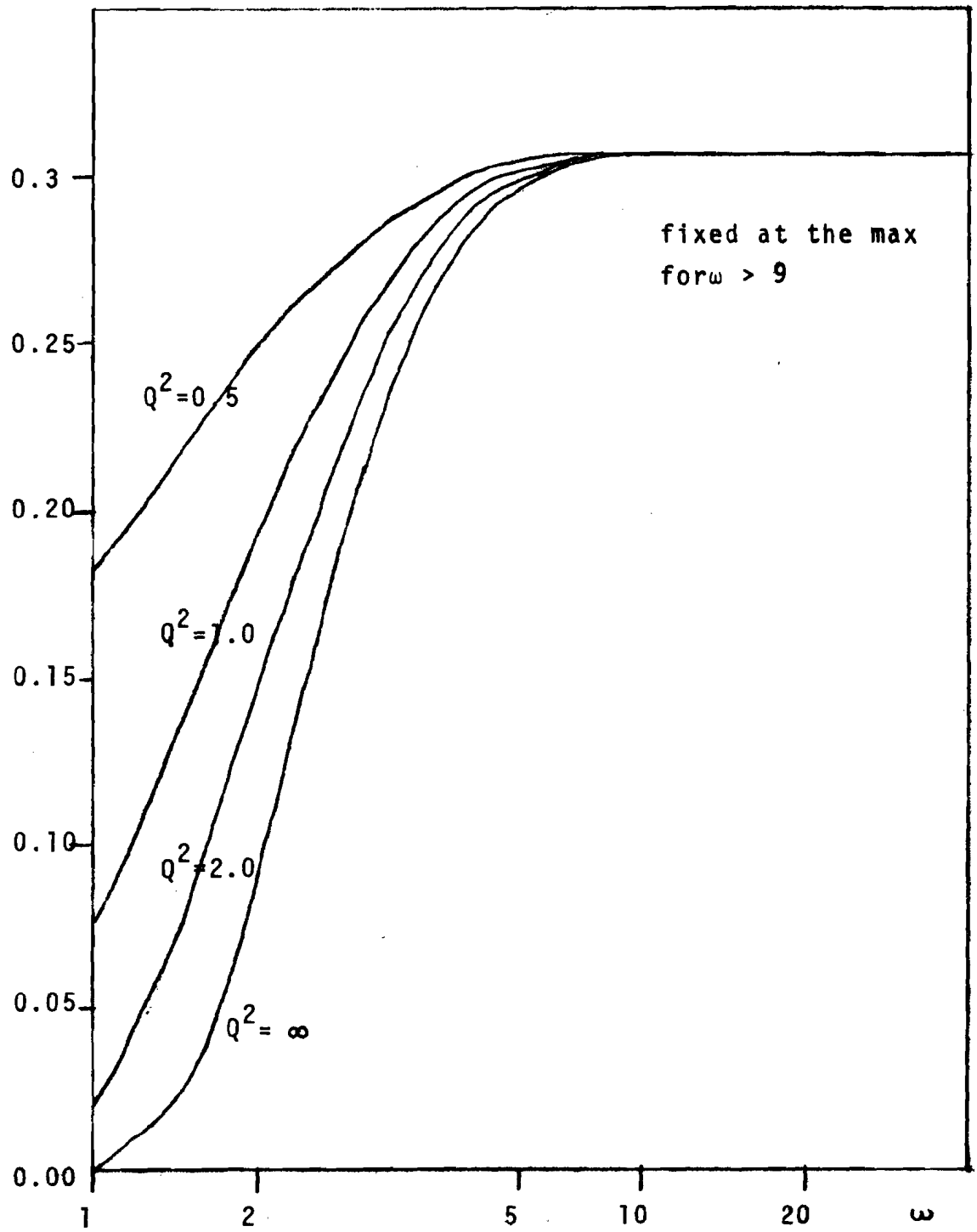

$$\frac{d\sigma(WAB)}{d\sigma(DI)} = \frac{Z^2\alpha}{\pi A} \quad \frac{y^2}{1-y} \quad \frac{G(Q^2)}{\nu W_2(\omega')}$$

where $y = \nu/E_0$, $Q^2 = M/\omega$ and

$$G(Q^2) = \int_0^\infty dQ_T^2 Q_T^2 \; F^2(Q^2+Q_T^2)/(Q_T^2 + Q^2)^2$$

$F(Q^2)$ is the nuclear form factor.

The effect is only important at low E' and also the contribution scales at two incident energies.

Figure E.2 shows a typical cross section, effect of radiative corrections and WAB.

Figure E.3 gives the amount of radiative corrections as a function of E' at different ω.

Figure E.4 shows integrand of exact formula for radiative corrections at several kinematical values.

Figure E.2 A typical cross section

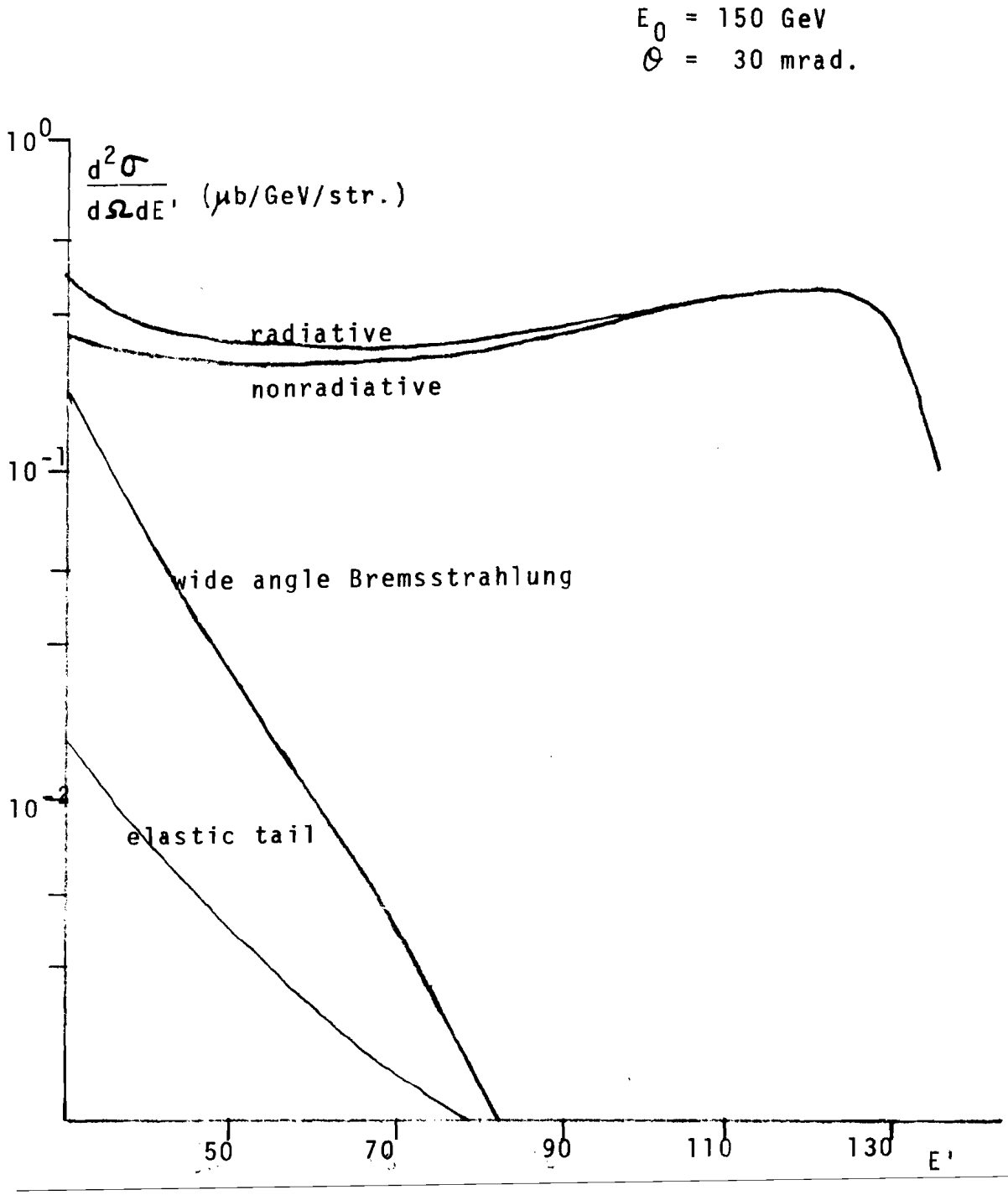

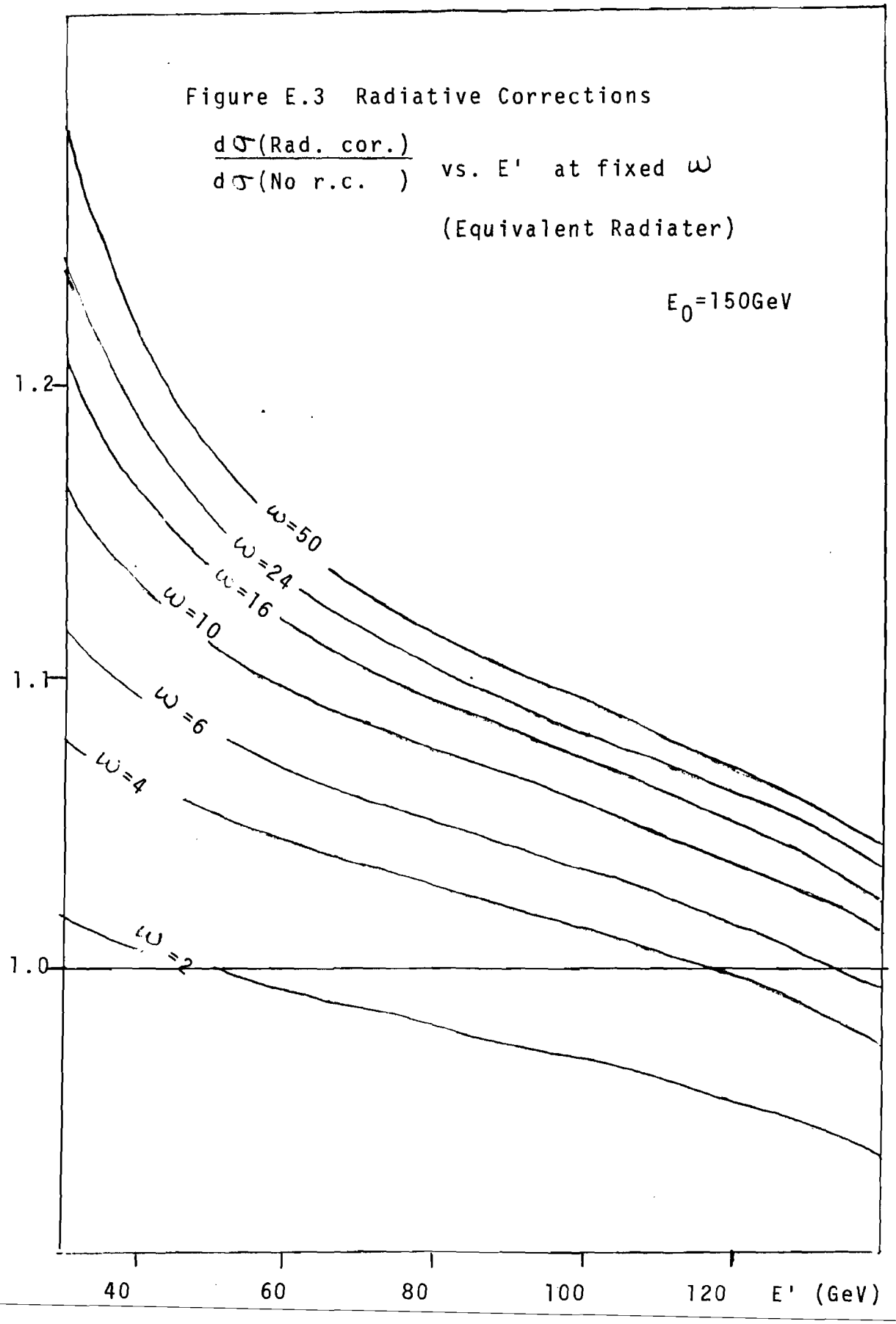
Figure E.3 Radiative Corrections
dσ(Rad. cor.) / dσ(No r.c.) vs. E' at fixed ω
(Equivalent Radiater)
E0=150GeV
1.2
1.1
1.0
ω=50
ω=24
ω=16
ω=10
ω=6
ω=4
ω=2
40
60
80
100
120
E' (GeV)

Figure E.4 Integrand of $\cos\theta_k$
(in the exact formula of radiative corrections)

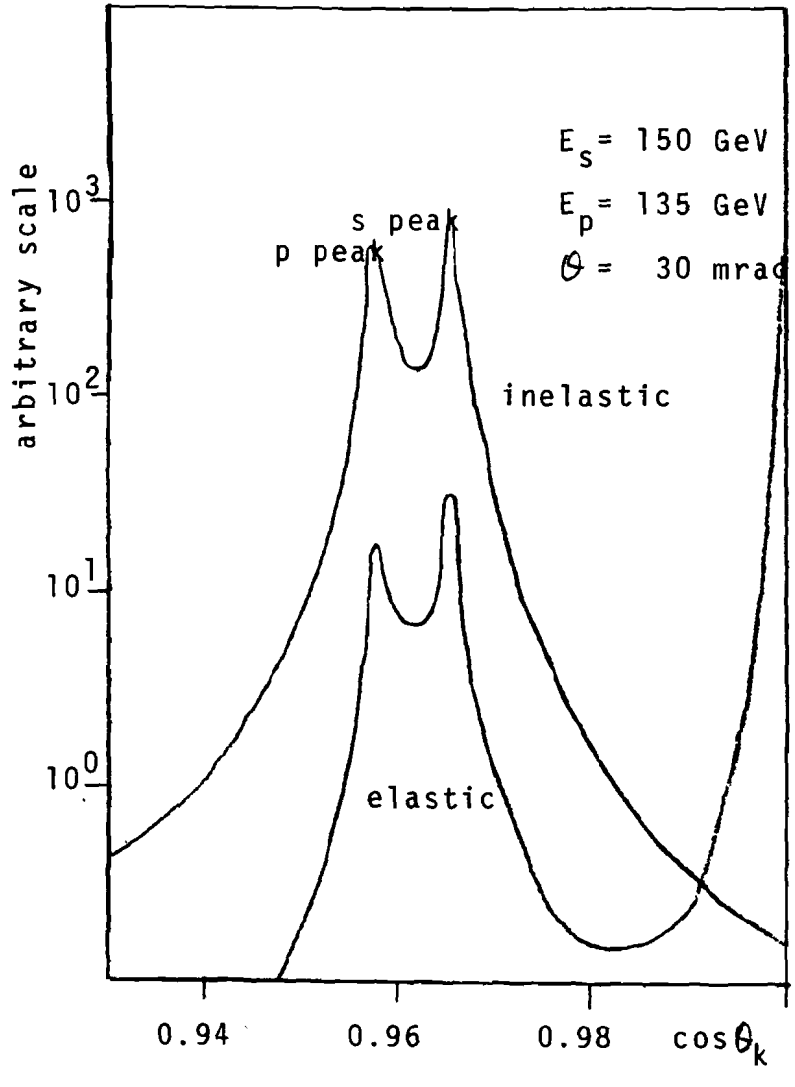

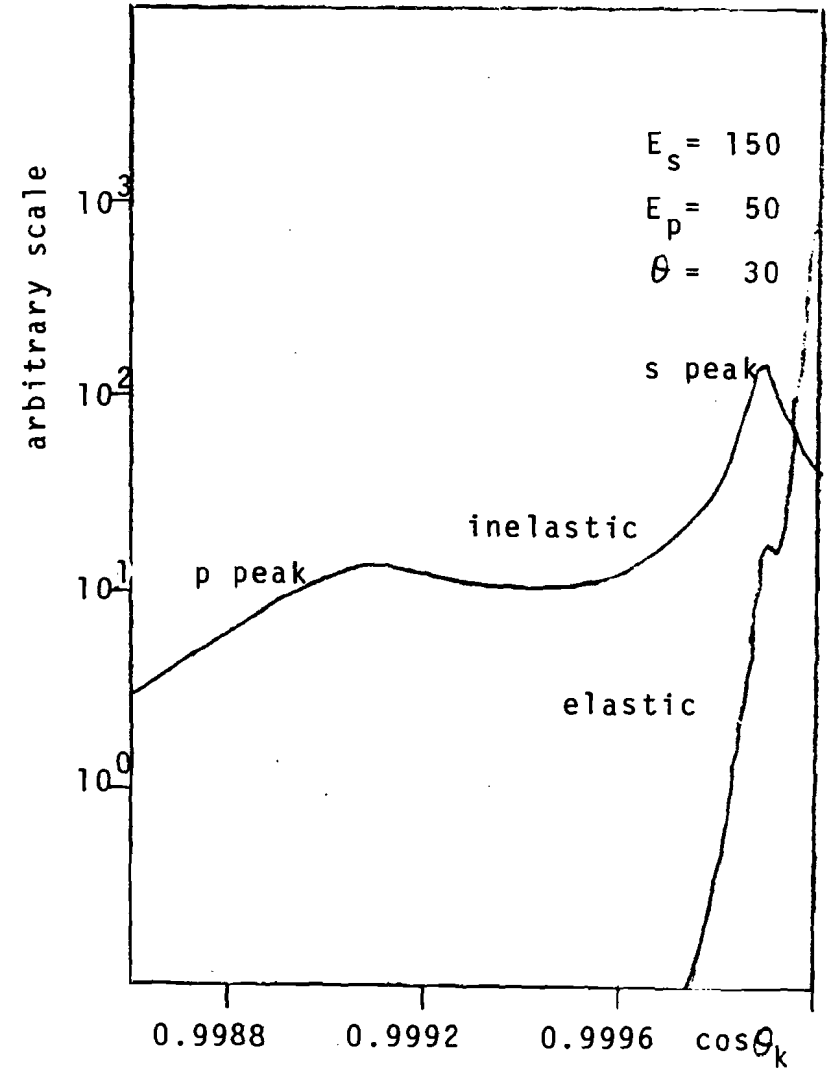

Appendix F

SYSTEMATIC UNCERTAINTIES

In this section, we list possible systematic uncertainties and estimate the magntitudes.

1) Normalization

The following factors come in, in obtaining the normalization for the data.

i) Number of effective muons

The scaler $(B \cdot \overline{BV}_{delayed})_{EVG}$ automatically corrected the effects due to the spark chamber dead time, accidental losses due to veto counters, and inefficiencies of beam counters and associated electronics.

The correction due to the beam size cut was obtained from the unbiased sample accumulated by the beam trigger.

The correction due to one and only one beam track was obtained after all the cuts, treating all the beam tracks the same, setting the position and the slopes zero. This number includes the inefficiency of beam chambers and that of beam reconstruction.

ii) Thickness of the target material

The thickness of carbon and iron target were scaled to the ratio of the energies. The error due to the ratio of energy being not exactly 0.375 as planned is 0.3%.

iii) Reconstruction efficiency

This is studied in Appendix C, and the relative efficiency between the two sets of data is estimated to be good to ±3%.

iv) Other efficiencies

Efficiencies of trigger counters in the spectrometer and the electronics were monitored during the data taking and checked to be better than 99%.

These numbers are summarized in Table F.1.

The uncertainties of the normalization was estimated by the fluctuation of event rate shown in Figure 4.3.

2) Incident energies

Incident enrgies were calculated from the bend angle through the bending magnets in the beam line. The bend angle is obtained by extrapolating beam tracks through the magnets to the beam hodoscope counter HA. Absolute values were obtained from the calibration constant of the magnets, the magnet current setting and the alignment constants of beam chamber and hodoscope system. The mean energies for the two sets of the data were estimated to be 148.3 and 55.89 GeV with the accuracy of ±1% each. We still refer the two sets of data as 150 and 56.3 GeV data.

The relative energy is known to better accuracy because the largest uncertainty of alignment constants cancel. The error was estimate to be ±0.5%.

Table F.1. The Number of Effective Muons

	150 GeV	56.3 GeV
Runs	457-465	535-563
$(B \cdot \overline{BV}_d)_{EVG}$	$0.966 \cdot 10^9$	$3.66 \cdot 10^9$
one and only one beam / trigger	0.899	0.959
$r_B < 9$ cm, $r_B' < 2$ mrad.	0.974	0.917
line finding efficiency	0.969	0.976
point finding efficiency	0.956	0.958
trigger loss	0.01	0.01
losses due to bad spills etc.	-	-
the number of effective muons	$0.780 \cdot 10^9$	$2.99 \cdot 10^9$
the number for Monte Carlo	$2.96 \cdot 10^9$	$5.00 \cdot 10^9$

Target Material

	150 GeV	56.3 GeV
Iron target	619.7 g/cm^2	229.9 g/cm^2
carbon target	63.1	22.5
target counters	6.7	6.7
total	689.5	259.1
relative	1.000	0.997

E_0 shift in the scaling ratio is to change $\lambda = 55.89/148.3$, so the effect is to shift Q^2 and ν by $Q^2 \cdot \Delta\lambda$ and $\nu \cdot \Delta\lambda$.

3) Shift of E'

The following effects are responsible for the possible shift of E'. The shift in reconstructing the momentum, calibration error in magnetic field measurement and some uncertainty in energy loss through iron. The calibration of the spectrometer discussed in Appendix D includes all these effects, and the relative uncertainty for E' shift for the two sets of data is estimated to be ±1%.

Figure F.1 shows the motion of events due to E' shift in Q^2-ν plane. When ω cut is made, the main effect is to change the number of events at low Q^2, affecting the normalization.

4) The resolution

Two methods were tried in correcting the different E' resolution between 150 and 56.3 GeV data. One method was to fold in an 8% gaussian error into 1/E' of 150 GeV data and Monte Carlo. The other was to rely on Monte Carlo correction, eliminating the sensitive region by recomputing E' to the value of $\omega = 1$ if $\omega < 1$.

Smearing due to 15% E' resolution in Q^2-ν plane is shown in Figure F.2.

Figure F.1

The Movement of Events

by E'⟶E'*1.01

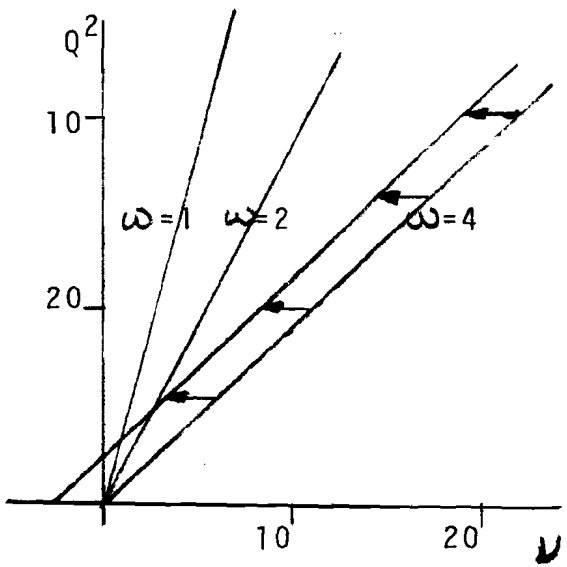

Figure F.2

The effect of 15% E' resolution

in Q^2 - ν plane

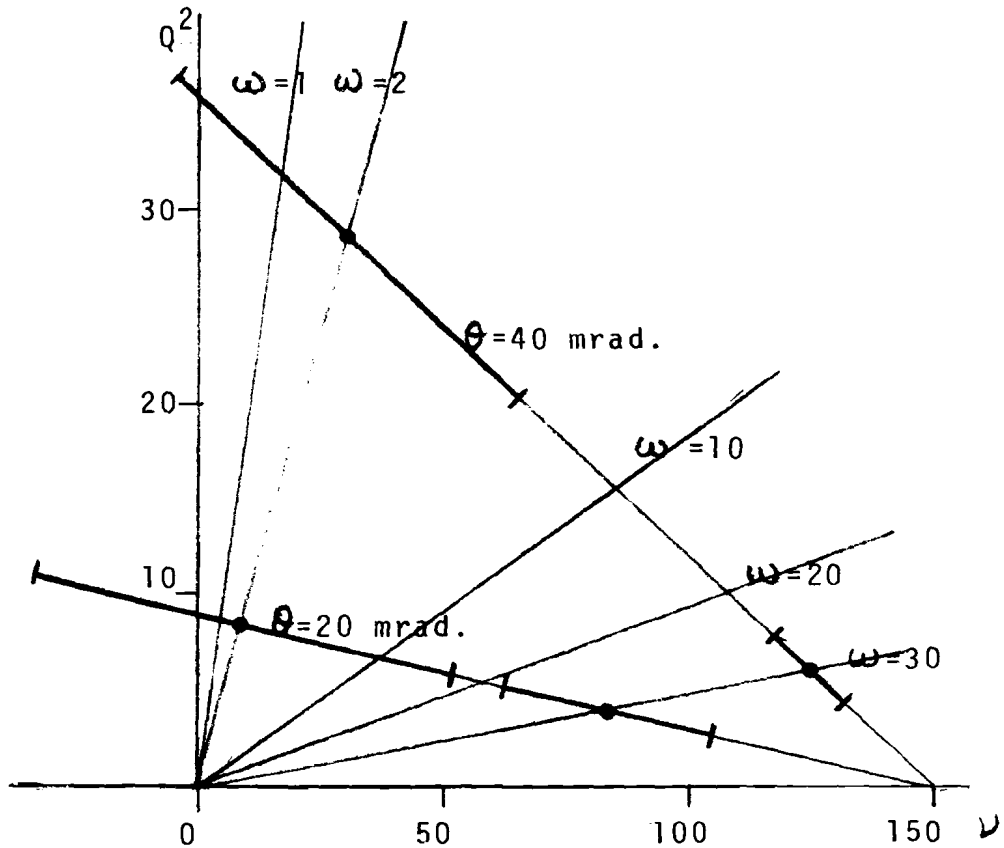

5) Radial dependence of magnetic field

Radial dependence of magnetic field of the spectrometer magnets were obtained in two independent ways. One was to obtain B-H curve from a small toroid made from the same iron. B-H curve was converted to radius dependence of the field for the spectrometer magnets.

In the other method, a direct measurement was made by drilling holes through some of $7\frac{3}{4}''$ thick plates of the magnets.

These measurements agree quite well and more than 0.5% difference between the inner and outer edge of magnets is very unlikely.

This uncertainty become negligible when taking the ratio of the two sets of data. Other possible contribution to the uncertainty is the off magnets used as an extra material for the scaling purpose in 150 GeV configuration. As the remnant field of the magnets is about 6 K gauss, these magnets must be degaussed. Differenr part of magnet experiences different degaussing cycle, as the H field changes inversely proportional to the radius and therefore varies by a factor of six from the inside to the outside radius of the magnets. Three out of eight magnets were degaussed for the 150 GeV configuration, monitoring the field at various radii carefully throughout the degaussing cycle.

One of the three was connected oppositely in this cycle to reduce the remaining effect. The maximum field undetectable is about $\sim$300 gauss, so the effect is less than $\pm$0.3% of the total field.

6) Biased inefficiencies

Loss of events due to the trigger requirement was monitored during the data taking. Efficiency of the spectrometer trigger banks at various radii was checked by a counter telescope. The efficiency was better than 99%.

Losses due to inefficiencies of spark chambers and the analysis program are studied in Appendix C.

The uniformity of the chambers over the plane was better than 95%.

Dependence on χ^2 is not a problem in the present analysis where no χ^2 tail was visible.

Beam veto signal was the coincidence of two counters placed after different amount of hadron absorber. The signal of each counter was latched in to monitor the effect of being killed by surviving hadrons.

Latching efficiency was checked to be better than 99% from the beam trigger. Table F.2 shows the amount of absorbers upstream of each counter and the frequency of latching at these counters.[32] Most of the counts were accidental, and partly due to the Cherenkov light from the light pipe.

But if all the counts at BV_{II} were due to surviving hadrons, the hadrons giving a coincidence of BV_{II} is about 1% for 56 GeV data and negligible for 150 GeV data. Firing both counters was consistent with the number expected from the real muon in the next RF bucket.

7) Misalignment effect

The spark chamber coordinates when converted from the time digitizer counts were corrected for the small displacement from the axis. The constants were determined in several steps. The beam tracks were used to align the chambers up to the module #2 and #3 in space. The two modules were not moved for the change of the configuration.

To align the chambers in the spectrometer, where this method fails because of multiple scattering in the concrete absorber, special data were taken triggering on small counters placed outside of magnet region. The data were good to several millimeters in aligning them. The limitatin was because the region illuminated by the triggers was close to the edge of the active region. Overall alignment was done analyzing mostly the calibration data. The tracks found in the chambers upstream of magnets were propagated through the spectrometer with the known momentum, and the displacement in the transverse direction to the bend plane was minimized.

BACKFIT is sensitive to certain misalignment effects.

Table F.2. Beam Veto Operations

1) Amount of absorber upstream of beam veto

150 GeV data

material	thickness	g/cm^2	attenuation lengths ($185\ g/cm^2$)
iron	32"	640	
concrete	160"	1463	
Up to BV_{II}		2003	10.8
concrete	96"	878	
Up to BV_I		2881	15.6

56.3 GeV data

iron	12"	240	
concrete	64"	585	
Up to BV_{II}		825	4.5
concrete	32"	293	
Up to BV_I		1118	6.0

2) Latching of BV / trigger

	BV_{II} only	BV_I only	both
150 GeV data	6.5 %	2.2 %	0.5 %
56.3GeV data	5.9 %	2.1 %	0.3 %

Possible effects are an intrinsic curvature in the spectrometer and the angle between the beam axis and the spectrometer axis.

The effect of an intrinsic curvature can be written as

$$\frac{1}{E'_m} = \frac{1}{E'_t} + \frac{\alpha_x}{E_0}\cos\phi + \frac{\alpha_y}{E_0}\sin\phi$$

where ϕ is the azimuthal angle of the muon track, E'_m and E'_t are the reconstructed momentum with and without misalignment.

α_x and α_y are the amount of misalignment in x and y direction relative to E_0.

α_x and α_y were obtained by calculating average values of $1/E_m$, $1/E_m\cos\phi$, etc. and found to be less than 3%. The effect of shifting ±3% was large, but the averaging due to azimuthal symmetry of the apparatus made it negligible except for the high E' edge, where proper averaging is not done.

8) <u>Effect of underlying physics</u>

Effects were studied on a simulated data by Monte Carlo program, which kept true values besides measured ones. To study, for example the effect of nonscaling of radiative corrections at two energies, the ratio of corrections were calculated for each accepted events, and the mean was obtained in each bin.

Nonscaling of radiative corrections due to internal bremsstrahlung is negligible and so is the x' effect.

Actual effects of corrections are shown in Figure F.3.

The effect of uncertainty of $R=\sigma_L/\sigma_L$ is only important if it is nonscaling and much larger than the assumed value of R=0.18.

The effect of Fermi motion was studied by comparing the Monte Carlo data with and without. Main difference observed is an E' shift of ~1%. Since the effect scales at the two energies, more sophisticated modeling of nucleon momentum distribution in the nucleus is not nesscery.

Effect on the propagator fit from imperfect modeling of Monte Carlo was estimated by weighting the Monte Carlo data to simulate different structure functions.

Figure F.3 Effects of underlying physics

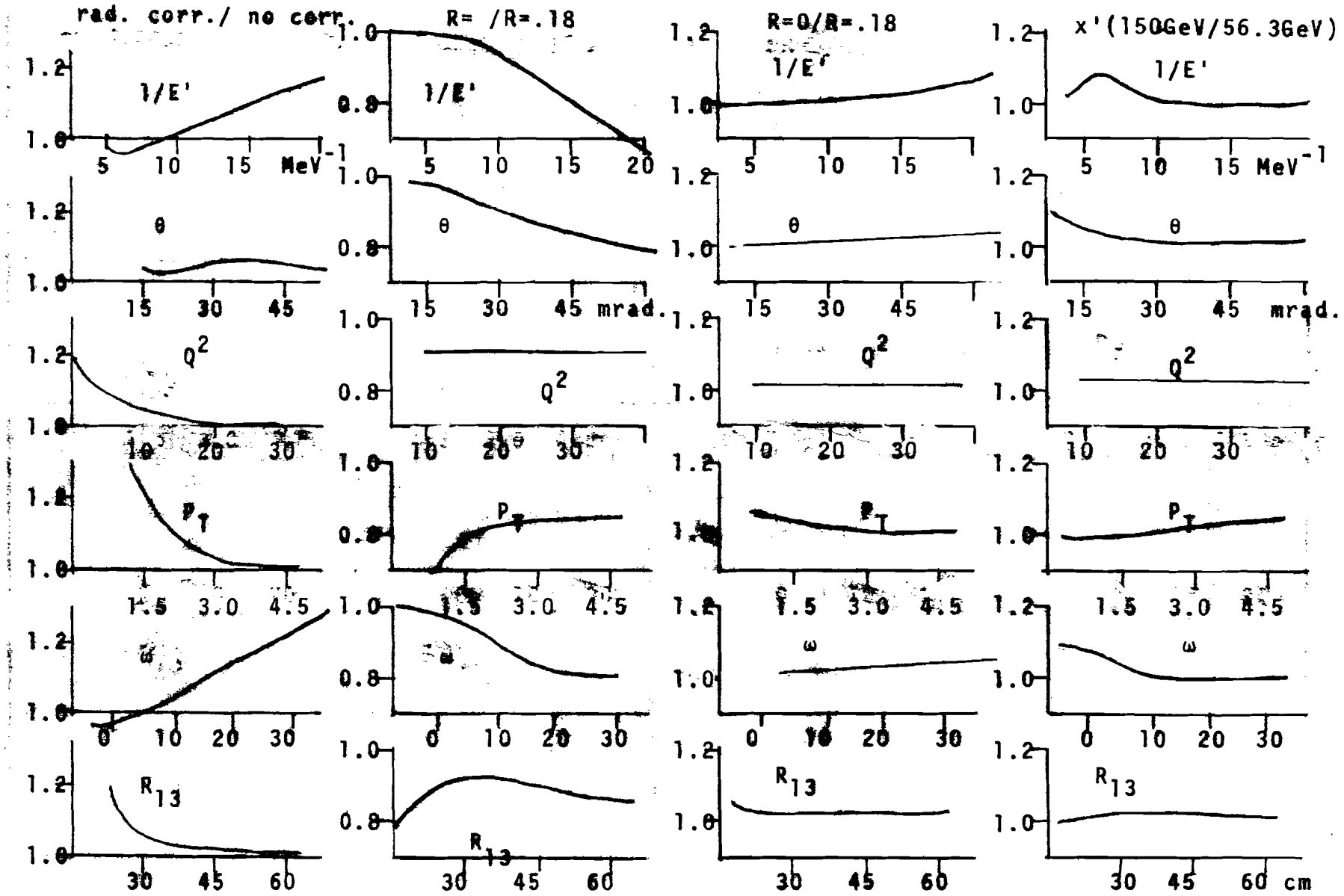

References

1. A good review of experimental finding in J.I Freedman and H.W. Kendal Annual Rev. of Nuc. Science 22 203 (1972).

2. J.D.Bjorken Phys. Rev. 179 1547 (1969).

3. R.D.Feynman Phys. Rev. Letters 23 1415 (1969). and in High Energy Collisions (Gordon and Breach 1969). J.D.Bjorken and E.A.Paschos,Phys.Rev 185 1975 (1969).

4. See a review by Llewellyn-Smith Phys.Reports 3C No.5 (1972).

5. S.D. Drell and T.M.Yan, Annals of Physics 66 555 (1971). Earlier works are referenced there in. Y.Frishman in Proceedings of the XVI International Confrence on High Energy Physics, J.D.Jackson and A.Roberts editor (National Accelerator Laboratory Batavia, Illinois, 1972) p.119.

6. D.J.Gross and F.Wilczek Phys.Rev.Letters 30 1343 (1973); G.'t Hooft (unpublished); H.D.Politzer, Phys.Rev. Letters 30 1346 (1973).

7. J.E.Augustin et al., Phys.Rev.Letters 34 764 (1975).

8. J.E.Augustin et al., Phys. Rev. Letters 33 1406 (1974). J.J.Aubert et al., Phys.Rev.Letters 33 1404 (1974). G.S. Abrams et al., Phys.Rev.Letters 33 1453 (1974).

9. A.M.Boyarski et al., Phys.Rev.Letters, to be published.

10. L.N.Hand, Phys.Rev. 129 1834 (1963).

11. C.G.Callan and D.G.Gross, Phys.Rev.Letters 22 156 (1969).

12. See Frederic J.Gilman Rapporteur's Talk XVII International Conference on High Energy Physics London, England July1-10, 1974

13. J.H.Christensen et al., Phys. Rev. D8 2016 (1974).

14. Measurement of pion contamination in the μ beam by Exp #98 at the Fermilab, private communication

15. Geoffery B.West, Annals of physics 74 464 (1972).

16. D.Yennie private communication. We thank him for teaching us the simple formula.

17. S.W.Herb,thesis,Cornell Univ.,being prepared.

18. J.-E.Augustin et al., Phys. Rev. Letters 34 233 (1974)
B.L.Beron et al., Phys. Rev. Letters 33 663 (1974)

19. E.M.Riordan et al., Phys. Letters 52B 249 (1974)

20. Michael S.Chanowitz and Sidney D.Drell Phys. Rev. D9 2078 (1974); K.Matumoto, Prog. Theor. Phys. 47 1795 (1972)

21. Geoffrey B.West and Peter Zerwas, Phys. Rev. D10 2130 (1974)

22. H.David Politzer, Phys. Rev. D9 2174 (1974)
D.J.Gross, Phys. Rev. Letters 32 1071 (1974)

23. J.Kogut and Leonard Susskind, Phys. Rev. D9 3391 (1974)

24. Ikaros Y.Bigi and James D. Bjorken, Phys. Rev. D10 (1974)

25. Jogesh C.Pati and Abdus Salam, Phys. Rev. D11 1137 (1975)

26. H.T.Nieh, Phys. Letters B53 344 (1974)

27. Y.Watanabe et al., Phys. Rev. Letters, to be published.

28. C.Chang et al., Phys. Rev. Letters, to be published.

29. C Chang, thesis, Michigan State Univ., being prepared.

30. P.Limon et al., Nuc.Instr. and Methods 116 317 (1974)
P.Limon et al., ibid., to be published.

31. A.Bodek, thesis, MIT (1973)

32. J.Geibel et al., Nuc. Instr. and Methods 32 45 (1965)

33. L.W.Mo and Y.S.Tsai, Rev. Mod. Phys. 41 205 (1969)
G.Grammer Jr., thesis, Cornell Univ. (1973)
Yung-Su Tsai "Radiative Corrections to Electron Scattering" SLAC-PUB-848 1971, unpublished.